Parametric Amplification and Squeezing with a Superconducting Resonator

Author:
Parker, Daniel

Publication Date:
2021

DOI:
https://doi.org/10.26190/unsworks/1980

License:
https://creativecommons.org/licenses/by/4.0/
Link to license to see what you are allowed to do with this resource.

UNSW

AUSTRALIA

SCHOOL OF ELECTRICAL ENGINEERING
AND TELECOMMUNICATIONS

Parametric Amplification and Squeezing with a Superconducting Resonator

by

Daniel Parker

Student ID: 3466223

Thesis submitted as a requirement for the degree

Masters of Engineering (Electrical Engineering)

Submitted: June 24, 2021
Supervisor: Dr Jarryd Pla

Thesis/Dissertation Sheet

Surname/Family Name	:
Given Name/s	:
Abbreviation for degree as give in the University calendar	:
Faculty	:
School	:
Thesis Title	:

Abstract 350 words maximum: (PLEASE TYPE)

ORIGINALITY STATEMENT

'I hereby declare that this submission is my own work and to the best of my knowledge it contains no materials previously published or written by another person, or substantial proportions of material which have been accepted for the award of any other degree or diploma at UNSW or any other educational institution, except where due acknowledgement is made in the thesis. Any contribution made to the research by others, with whom I have worked at UNSW or elsewhere, is explicitly acknowledged in the thesis. I also declare that the intellectual content of this thesis is the product of my own work, except to the extent that assistance from others in the project's design and conception or in style, presentation and linguistic expression is acknowledged.'

Signed   …………………………………………...............

Date   …………………………………………...............

INCLUSION OF PUBLICATIONS STATEMENT

UNSW is supportive of candidates publishing their research results during their candidature as detailed in the UNSW Thesis Examination Procedure.

Publications can be used in their thesis in lieu of a Chapter if:
- The candidate contributed greater than 50% of the content in the publication and is the "primary author", ie. the candidate was responsible primarily for the planning, execution and preparation of the work for publication
- The candidate has approval to include the publication in their thesis in lieu of a Chapter from their supervisor and Postgraduate Coordinator.
- The publication is not subject to any obligations or contractual agreements with a third party that would constrain its inclusion in the thesis

Please indicate whether this thesis contains published material or not:

☐ This thesis contains no publications, either published or submitted for publication
(if this box is checked, you may delete all the material on page 2)

☐ Some of the work described in this thesis has been published and it has been documented in the relevant Chapters with acknowledgement
(if this box is checked, you may delete all the material on page 2)

☐ This thesis has publications (either published or submitted for publication) incorporated into it in lieu of a chapter and the details are presented below

CANDIDATE'S DECLARATION

I declare that:

- I have complied with the UNSW Thesis Examination Procedure

- where I have used a publication in lieu of a Chapter, the listed publication(s) below meet(s) the requirements to be included in the thesis.

Candidate's Name	Signature	Date (dd/mm/yy)

Abstract

Degenerate microwave amplifiers offer the potential to perform a measurement of weak microwave signals free from any degradation to their signal-to-noise ratio, a benefit afforded by the quantum mechanics of their phase sensitive gain [1]. The degenerate parametric amplifier may even be used to enhance the signal-to-noise ratio of a weak measurement by squeezing the vacuum fluctuations below the standard quantum limit. Consequently, parametric amplifiers have featured in a number of recent sensitivity breakthroughs across multiple fields. These include the detection of gravitational waves [2], the search for dark matter [3], and high sensitivity electron spin resonance spectroscopy [4]. In this thesis, we present a novel microwave degenerate parametric amplifier based on the non-linear superconducting phenomenon of kinetic inductance. The device is a simple and robust quantum limited phase sensitive amplifier, which is well described by theory and shows potential as a highly-effective tool for the production of squeezed microwave light.

Contents

Acknowledgements

Like most projects, this thesis is not the result of my efforts alone. Jarryd, you have been guiding this research every step of the way. Without your hard work and dedication to this project, it would not have turned out the same. You've taught me so much these last two years, for which I thank you.

Mykhailo, the experiments detailed in this thesis would not have been possible without the brilliant device that you designed and manufactured. Thank you for this opportunity and for being a great travel companion. Wyatt, thank you for taking on the remaining few hurdles this project has to offer, and I wish the best of luck in what lies ahead. I'd like to also acknowledge Tim Duty, Andrea Morello, Arne Laucht and the staff at ANFF from UNSW for the expertise and resources they each contributed to this project, and Arne Grimsmo from the University of Sydney for his contributions to the theory presented in this thesis.

To my friends, you have provided much needed support and distraction over what's been a crazy year. I just hope you learn to trust me when I next call an emergency meeting. Hannes, thanks for the countless coffees, conversations and board games. Sam, thank you for giving me 725 reasons to take a break from my work. Finally, I wish to thank my family: my beautiful wife Caro, young Wallace the stinky, my parents Kathryn and John, and my sisters Lucy and Sarah. You've been my rock throughout this process and I couldn't have finished this without you.

Abbreviations

KIPA Kinetic Inductance Parametric Amplifier

cQED Circuit Quantum Electro-Dynamics

SNR Signal to Noise Ratio

SQL Standard Quantum Limit

DPA Degenerate Parametric Amplifier

3WM Three Wave Mixing

4WM Four Wave Mixing

TLS Two Level Systems

CPW Coplanar Waveguide

TEM Transverse Electomagnetic

VNA Vector Network Analyser

SQUID Superconducting Quantum Interference Device

TWPA Travelling Wave Parametric Amplifier

PBG Photonic Band-Gap

IDC Inter-Digitated Capacitor

EBL Electron Beam Lithography

RIE Reactive Ion Etch

List of Figures

List of Tables

Chapter 1

Introduction

Low noise and high gain microwave amplifiers have become a staple in contemporary experiments in the fields of condensed matter physics and quantum engineering. In order to sensitively measure weak microwave signals emitted by quantum systems, experimentalists require an amplifier that boosts the strength of the signal without excessively degrading the Signal to Noise Ratio (SNR). Microwave amplifiers based on parametric photon conversion are becoming an increasingly popular choice as they can operate very close to the quantum noise limit (also known as the Standard Quantum Limit), where only the minimal amount of noise required by quantum mechanics is added to the amplified signal. Parametric microwave amplifiers have enabled the high-fidelity readout of quantum bits in elementary quantum processors [8], and pushed the sensitivity of electron spin resonance to new limits [4, 9, 10, 11].

Parametric amplifiers largely fall into one of two classes: phase insensitive or phase sensitive. In quantum mechanics, a classical electromagnetic field $a(t) = I\cos(\omega t) + Q\sin(\omega t)$ (with angular frequency ω) can be described by dimensionless quadrature field operators $\hat{I}$ and $\hat{Q}$. A phase insensitive amplifier applies gain G equally to both quadratures $\langle \hat{I}_{\text{out}} \rangle = G\langle \hat{I} \rangle$ and $\langle \hat{Q}_{\text{out}} \rangle = G\langle \hat{Q} \rangle$ (where $\hat{I}_{\text{out}}$ and $\hat{Q}_{\text{out}}$ represent the field at the output of the amplifier), unavoidably adding at least $1/4$ photon of noise to each quadrature in the process [1]. Conversely, for a phase-sensitive amplifier, one field quadrature is amplified $\langle \hat{I}_{\text{out}} \rangle = G\langle \hat{I} \rangle$, whilst the other is deamplified $\langle \hat{Q}_{\text{out}} \rangle = \langle \hat{Q} \rangle/G$. This definition of quadrature gain allows for amplification without any added noise [1]. The noiseless nature of a phase-sensitive amplifier makes it distinctly useful for detecting small microwave signals containing only a handful of photons [12].

Phase sensitive parametric amplifiers not only de-amplify wave-packets of photons along a single quadrature, but have been shown to suppress the fluctuations of the electromagnetic field in a phenomenon known as squeezing. Electromagnetic radiation cooled to its ground state will produce noise (known as the vacuum fluctuations) such that the uncertainty relation holds: $\langle \Delta \hat{Q}^2 \rangle \langle \Delta \hat{I}^2 \rangle \geq 1/16$, where $\langle \Delta \hat{I}^2 \rangle$ and $\langle \Delta \hat{Q}^2 \rangle$ represent the variances of the field quadratures (in photon units). Simply cooling the microwave radiation in a given system will produce vacuum fluctuations that are equal on each quadrature: $\langle \Delta \hat{Q}^2 \rangle = \langle \Delta \hat{I}^2 \rangle = 1/4$, commonly referred to as the Standard Quantum Limit (SQL). Historically, the SQL has been considered a fundamental limit on photon detection sensitivity until the advent of squeezing technology. A phase sensitive amplifier may reduce (or squeeze) the vacuum fluctuations along one quadrature, while amplifying the vacuum fluctuations along another such that the uncertainty relation still holds. In applications where the measurement may be projected onto a single quadrature, squeezed noise can be used to enhance SNR in experiments requiring high sensitivity. So far, squeezing technology has been successfully deployed in the search for dark matter axions [13, 3], the manipulation of the coherence properties of a superconducting qubit [14], the detection of gravitational waves [2], and high sensitivity electron spin resonance (ESR) spectroscopy [7].

Squeezed vacuum states may also prove to be a valuable resource in quantum computing [15]. Measurement-based computation using highly-entangled cluster states encoded in the modes of an electromagnetic field is one credible pathway to achieving large-scale quantum computation [15]. Critically, it has been shown that fault-tolerance in this scheme can be attained using vacuum states squeezed by at least $15-17\,\mathrm{dB}$ [16]. Circuit-based microwave squeezers are a particularly attractive platform in this context, as they combine manufacturability with another key requirement in cluster-state computing, the ability to engineer non-Gaussian states of light [15].

The simplest parameteric microwave amplifier is the Degenerate Parametric Amplifier (DPA), characterised by a pumped non-linear cavity that facilitates the conversion of pump photons to signal photons via multi-wave mixing. In this thesis, I present a new type of phase-sensitive microwave parametric amplifier that behaves as a near-ideal DPA. Our device is fabricated using a single-step lithography process on a thin film on NbTiN, which provides the non-linearity responsible for multi-wave mixing. This non-linearity

originates from a kinetic inductance intrinsic to the NbTiN film [17, 18, 19, 20]. As such, we have decided to call our device a Kinetic Inductance Parametric Amplifier, or KIPA for short.

We observe in excess of 40 dB gain for phase insensitive operation and up to 50 dB of gain in phase sensitive mode, with a gain-bandwidth product of approximately 100 MHz. A 1 dB-compression power of -43 dBm enables high gain amplification of small microwave signals without device saturation and is nearly five orders of magnitude improvement on other microwave parametric amplifiers [21, 22]. Phase sensitive amplification of a coherent tone is used to observe deamplification of up to 26 dB without the distortions, known to limit the achievable squeezing, commonly observed in other devices [7, 5, 20]. We successfully predict the behaviour of the KIPA using a theoretical framework based on the ideal DPA and present early measurements on its noise squeezing properties. Combined with a statistical analysis of the output noise fields for a vacuum state input, we produce a body of evidence to suggest that our device well approximates the ideal DPA, even for phase sensitive gains as high as 30 dB. Finally, we find a phase sensitive noise temperature of 0.07 photons, demonstrating that the KIPA is quantum limited.

This thesis is organised into four chapters:

- **Background**: We begin the thesis with a review of the literature on microwave parametric amplifiers and present the mathematical background required to develop the theory of the KIPA in later chapters.

- **The Kinetic Inductance Parametric Amplifier**: In this chapter we describe how the KIPA was designed and manufactured, and present the derivation of the KIPA Hamiltonian.

- **Amplifier Performance**: This chapter presents a series of experiments that we use to quantify the KIPA's utility as a microwave amplifier. We measure the phase insensitive and phase sensitive gains of the KIPA as well as its 1 dB-compression power.

- **Quantum Characteristics**: We conclude the thesis with a series of experiments used to understand the KIPA's noise properties and potential as a squeezer.

Chapter 2

Background

This chapter begins with a review of the quantum limits on amplifiers first introduced by Caves and the phenomenon of squeezing. The Degenerate Parametric Amplifier (DPA) is a technology that has been demonstrated to operate close to these limits, which we review and explore its ability to squeeze the vacuum. The requisite background theory to understand how a DPA operates is then presented, starting with the quantum mechanical microwave resonator and the theory of coupling to a microwave cavity, followed by a description of two different types of non-linear microwave media that can be used to construct a DPA – the Josephson junction and kinetic inductance. The Josephson Parametric Amplifier (JPA) currently represents the state-of-the-art in microwave squeezing technology. We review a selection of these amplifiers to provide a comparison to the new kind of microwave squeezer described in this thesis, the Kinetic Inductance Parametric Amplifier (KIPA). To finish we briefly introduce the kinetic inductance Travelling Wave Parametric Amplifier (TWPA) to motivate the potential use of kinetic inductance in a DPA, as is achieved by this work.

2.1   Linear Amplifiers: Quantum Limits & Squeezing

The formalism of squeezing was first introduced by Carlton Caves in his seminal paper: *Quantum limits on noise in linear amplifiers* [1]. Shortly after its publication, squeezing was first demonstrated by Slusher *et al.* in the optical domain [23] and then by Movshovich *et al.* at microwave frequencies [24]. Since then, quantum limited amplifiers that produce squeezing have become a powerful tool in modern experimental quantum

physics [14, 7, 13, 2, 25], all strictly adhering to the theory first introduced by Caves in 1982 [1]. We begin our review of the literature with the quantum mechanical noise limits of linear amplifiers, first discovered by Caves. Following this, we define the phenomenon of squeezing, a consequence of Caves' fundamental limits. Caves' theory extends to multi-mode (wideband) linear amplifiers and generalises to the situation where there is a frequency difference between input and output modes. These generalisations are beyond the scope of this thesis, therefore, we confine the discussion to the amplification of narrow-band signals where input and output mode frequencies coincide.

Consider a narrow-band input signal $y(t) = A\cos(\omega t + \varphi)$ with amplitude A, frequency ω, and phase φ. The input $y(t)$ may be equivalently represented by its quadratures I and Q ($I, Q \in \mathbb{R}$) such that $y(t) = I\cos(\omega t) + Q\sin(\omega t)$, where $A = \sqrt{I^2 + Q^2}$ and $\varphi = \arctan(-I/Q)$. Another way to represent y is as a complex phasor rotating at frequency ω, where $y = I + jQ$. In the classical picture, a linear amplifier is a device that linearly increases the quadratures of our input phasor to $\sqrt{G_I}I + j\sqrt{G_Q}Q$ where $G_I, G_Q \in \mathbb{C}$. Note that the power gains G_I and G_Q are not required to be equal.

In the quantum picture, the input quadratures I and Q are promoted to the operators $\hat{I}$ and $\hat{Q}$ such that the canonical commutation relation $[\hat{I}, \hat{Q}] = i/2$ is satisfied. Consequently, the variances of the quadrature operators must obey the Heisenberg uncertainty principal [26]:

$$\langle \Delta \hat{I}^2 \rangle \langle \Delta \hat{Q}^2 \rangle \geq \frac{|\langle [\hat{I}, \hat{Q}] \rangle|^2}{4} = \frac{1}{16} \tag{2.1}$$

In this picture, the phasor and its conjugate relate to the creation and annihilation operators as:

$$\hat{a}^\dagger = \hat{I} + j\hat{Q} \tag{2.2}$$

$$\hat{a} = \hat{I} - j\hat{Q} \tag{2.3}$$

obeying the commutation relation $[\hat{a}, \hat{a}^\dagger] = 1$. In the Fock basis, the states $|0\rangle, |1\rangle, \cdots |n\rangle$ represent the photon population of the electromagnetic mode. Acting on the state $|n\rangle$, the creation operator populates the mode with an extra photon: $\hat{a}^\dagger |n\rangle = \sqrt{n+1}|n+1\rangle$, while the annihilation operator depopulates the mode by one photon: $\hat{a}|n\rangle = \sqrt{n}|n-1\rangle$ for $n \geq 1$ [27]. If the mode is in the ground (or vacuum) state $|0\rangle$ then the eigenvalue is zero and we have $\hat{a}|0\rangle = 0$. It is useful to also define the number operator $\hat{a}^\dagger \hat{a}$, whose

expectation provides the number of photons n in the mode:

$$\langle \hat{a}^\dagger \hat{a} \rangle = \langle n | \hat{a}^\dagger \hat{a} | n \rangle = n \tag{2.4}$$

We proceed with a simplified proof of Caves' fundamental noise limits for linear amplifiers by making two assumptions: that the phase of the input and the output are the same, and that no mixing of quadratures occurs. The former is equivalent to applying a suitable rotation of basis to the output vector space, however, the latter is not guaranteed to be true in practice as has been observed in our device. For the complete proof see Caves [1]. Under these assumptions, a linear amplifier produces the output operators $\hat{I}_{\text{out}}$ and $\hat{Q}_{\text{out}}$ related to the input field $(\hat{I}, \hat{Q})$ by:

$$\hat{I}_{\text{out}} = \sqrt{G_I}\hat{I} + \mathcal{F}_I \tag{2.5}$$

$$\hat{Q}_{\text{out}} = \sqrt{G_Q}\hat{Q} + \mathcal{F}_Q \tag{2.6}$$

With quadrature power gains G_I and G_Q. When $G_I = G_Q$ the amplifier is said to be phase insensitive, and when $G_I \neq G_Q$ the gain in phase sensitive. Caves introduces the additional 'noise' operators $\mathcal{F}_I$ and $\mathcal{F}_Q$ to ensure that the output fields satisfy the canonical commutation relation $[\hat{I}_{\text{out}}, \hat{Q}_{\text{out}}] = i/2$ [1]. Without loss of generality, it is assumed that $\langle \mathcal{F}_I \rangle = \langle \mathcal{F}_Q \rangle = 0$ [1]. In order to satisfy the canonical commutation relation, the commutator of the noise fields must equal:

$$\left[\mathcal{F}_I, \mathcal{F}_Q\right] = \frac{i}{2}(1 - \sqrt{G_I G_Q}) \tag{2.7}$$

giving the uncertainty relation:

$$\langle \Delta \mathcal{F}_I^2 \rangle \langle \Delta \mathcal{F}_Q^2 \rangle \geq \frac{|\langle \left[\mathcal{F}_I, \mathcal{F}_Q\right] \rangle|^2}{4} = \frac{|G_I G_Q|}{16}\left|1 - \frac{1}{\sqrt{G_I G_Q}}\right|^2 \tag{2.8}$$

Assuming that the noise operators and input field quadratures are uncorrelated, the fluctuations of the output quadrature operators are given by:

$$\langle \Delta \hat{I}_{\text{out}}^2 \rangle = |G_I|\langle \Delta \hat{I}^2 \rangle + \langle \Delta \mathcal{F}_I^2 \rangle \tag{2.9}$$

$$\langle \Delta \hat{Q}_{\text{out}}^2 \rangle = |G_Q|\langle \Delta \hat{Q}^2 \rangle + \langle \Delta \mathcal{F}_Q^2 \rangle \tag{2.10}$$

We may now write down an uncertainty relation for the output field quadratures using Equations 2.1 and 2.8:

$$\langle \Delta \hat{I}_{\text{out}}^2 \rangle \langle \Delta \hat{Q}_{\text{out}}^2 \rangle \geq |G_I G_Q|\langle \Delta \hat{I}^2 \rangle \langle \Delta \hat{Q}^2 \rangle + \langle \Delta \mathcal{F}_I^2 \rangle \langle \Delta \mathcal{F}_Q^2 \rangle \tag{2.11}$$

$$\geq \frac{|G_I G_Q|}{16} + \frac{|G_I G_Q|}{16}\left|1 - \frac{1}{\sqrt{G_I G_Q}}\right|^2 \tag{2.12}$$

Referring the output quadrature fluctuations to the input of the device using $\hat{I}_e = \hat{I}_{\text{out}}/\sqrt{G_I}$ and $\hat{Q}_e = \hat{Q}_{\text{out}}/\sqrt{G_Q}$, and subtracting the quadrature fluctuations of the input, we arrive at an expression for the minimum input referred noise a linear amplifier must add to the signal, defined by Caves as the *Amplifier Uncertainty Principal* or the *Fundamental Theorem for Phase Sensitive Linear Amplifiers* [1]:

$$\langle \Delta \hat{I}_e^2 \rangle \langle \Delta \hat{Q}_e^2 \rangle - \langle \Delta \hat{I}^2 \rangle \langle \Delta \hat{Q}^2 \rangle \geq \frac{1}{16} \left| 1 - \frac{1}{\sqrt{G_I G_Q}} \right|^2 \qquad (2.13)$$

Note that in the special case where the product $\sqrt{G_I G_Q} = 1$ (i.e. no amplification takes place), a linear amplifier may contribute no noise whatsoever yet the input and output fluctuations still obey the Heisenberg uncertainty principal. Further, in the case where $G_I = G_Q = G$, the amplifier is said to be phase insensitive as the amplitude of the signal increases by $\sqrt{G}$ irrespective of the phase of the input. The uncertainty relation reduces to the *Fundamental Theorem for Phase Insensitive Linear Amplifiers* [1]:

$$\langle \Delta \hat{I}_e^2 \rangle \langle \Delta \hat{Q}_e^2 \rangle - \langle \Delta \hat{I}^2 \rangle \langle \Delta \hat{Q}^2 \rangle \geq \frac{1}{16} \left| 1 - \frac{1}{G} \right|^2 \qquad (2.14)$$

If the power gain G is large, then the phase insensitive amplifier contributes at minimum an additional 1/4 photons to the input referred fluctuations.

Caves' fundamental theorems for linear amplifiers are illustrated in Figure 2.1 assuming the optimal phase insensitive amplifier and the optimal phase insensitive amplifier.

For the phase insensitive amplifier, setting $G_I = G_Q = G$ implies that inputs of constant magnitude map to outputs of constant magnitude, hence the gain is insensitive to phase. The phase insensitive amplifier not only amplifies the input fluctuations $\langle \Delta \hat{I}^2 \rangle$ and $\langle \Delta \hat{Q}^2 \rangle$ by the gain G, but also contributes $G/4$ photons of noise to each quadrature (or 1/4 photons referred to the amplifier input).

For the phase sensitive amplifier, the picture is more interesting. One quadrature $\hat{I}$ is amplified by $\sqrt{G}$ while the other is deamplified by $\sqrt{G}$. Upon inspection of the noise along the amplified quadrature, the input fluctuations increase by G and the amplifier adds no additional noise. If we can project our measurement onto the amplified quadrature then optimal phase sensitive amplification offers a better Signal to Noise Ratio (SNR) than is permitted by the quantum mechanics of the optimal phase insensitive amplifier. If the signal of interest is only on the order of a few photons, this enhancement in SNR
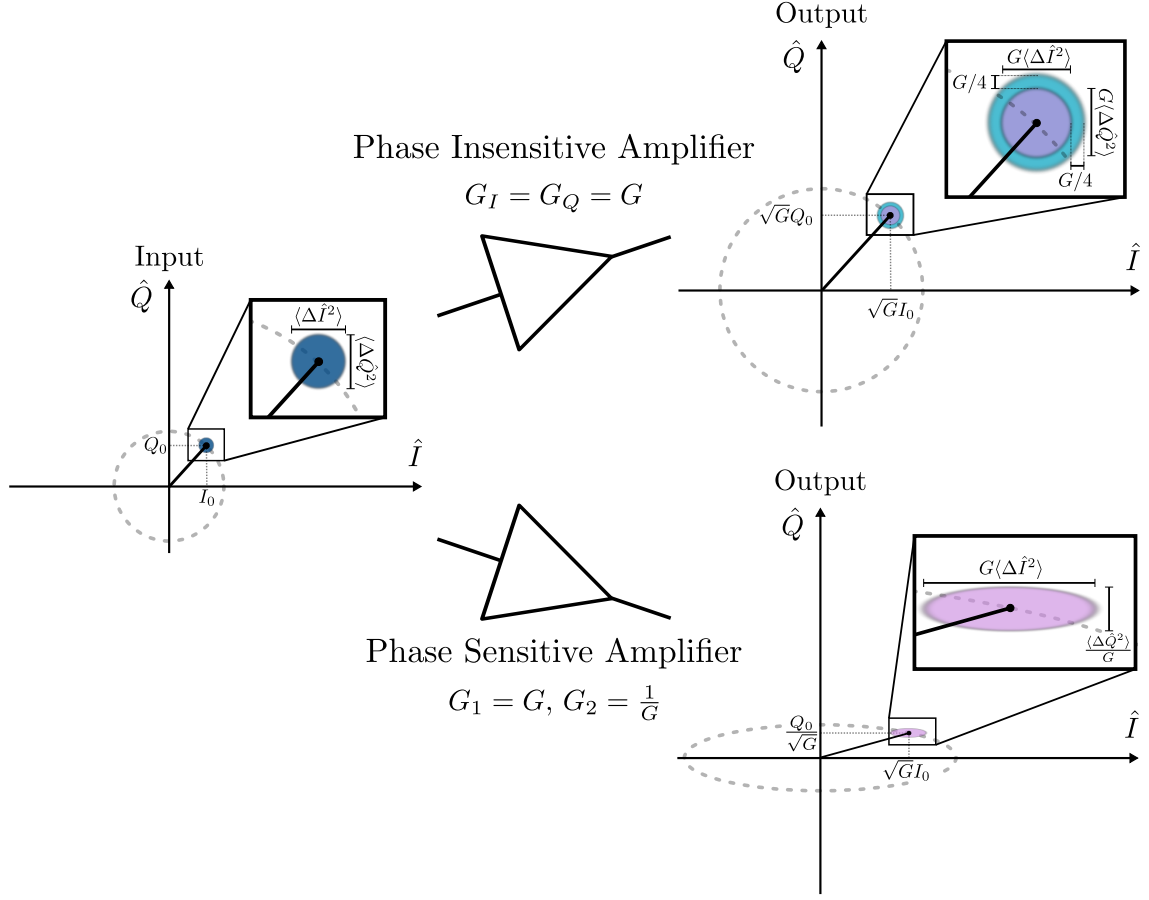
Figure 2.1: A depiction of the optimal phase insensitive amplifier and optimal phase sensitive amplifier acting on an input with expectations $\langle \hat{I} \rangle = I_0$ and $\langle \hat{Q} \rangle = Q_0$ with quadrature variances $\langle \Delta \hat{I}^2 \rangle$ and $\langle \Delta \hat{Q}^2 \rangle$ (dark blue circle). The phase insensitive amplifier increases both quadratures by the amplitude gain $\sqrt{G}$ and the noise on both input quadratures by G (purple circle). Further, the optimal amplifier adds an additional $G/4$ photons to the output variance (blue annulus). The phase sensitive amplifier increases the amplitude on $\hat{I}$ by $\sqrt{G}$ while decreasing the amplitude on $\hat{Q}$ by $\sqrt{G}$. The amplifier contributes no additional noise, and instead amplifies the input noise along $\hat{I}$ by gain G and deamplifies the noise by G along $\hat{Q}$ (pink ellipse). The dashed lines are used to indicate the mapping of inputs of constant magnitude to the output planes of the phase sensitive and phase insensitive amplifier.

is significant. An example use is the inductive detection of spins in quantum-limited Electron Spin Resonance (ESR) experiments, where a small ensemble of spins produces a fluctuation of signal amplitude at the resonance frequency (also known as a spin echo) that may be projected onto a single quadrature without loss of information.

Turning now to the deamplified quadrature, we find that in order for equality to hold in Equation 2.12, the fluctuations along $\hat{Q}$ must be decreased by G such that:

$$\langle \Delta \hat{I}_{\text{out}}^2 \rangle \langle \Delta \hat{Q}_{\text{out}}^2 \rangle = \langle \Delta \hat{I}^2 \rangle \langle \Delta \hat{Q}^2 \rangle \tag{2.15}$$

Along one quadrature, the noise is reduced below the intrinsic noise of the input. Consider the vacuum state $|0\rangle$ as an input to this amplifier. The fluctuations of the vacuum state along $\hat{Q}$ are $\langle \Delta \hat{Q}^2 \rangle = 1/4$, and are commonly referred to in the literature as the Standard Quantum Limit (SQL) [27]. The optimal phase sensitive amplifier is able to reduce the noise below the SQL, and permits the measurement of signals weaker than the vacuum noise along a single quadrature. The is precisely the definition of *Squeezing*: a reduction of noise below the SQL. The *Squeezing Level* $\mathcal{S}$ quantifies the reduction in vacuum fluctuations by the amplifier, and is typically expressed in dB. For squeezing along $\hat{Q}$:

$$\mathcal{S} = 10 \log_{10} \frac{\langle \Delta \hat{Q}^2 \rangle}{\langle \Delta \hat{Q}_{\text{out}}^2 \rangle} \tag{2.16}$$

For the optimal phase sensitive amplifier $\mathcal{S} = 10 \log_{10} G$.

2.2 The Degenerate Parametric Amplifier

The simplest and most common device used to realise squeezing is the Degenerate Parametric Amplifier (DPA), which uses multi-wave mixing arising from some non-linear medium to produce phase sensitive amplification approaching the quantum limits introduced by Caves [5, 12, 22, 28]. The degenerate parametric amplifier is constructed from a cavity containing a non-linear medium (see Figure 2.2). For example in the optical domain, the DPA may be realised using a pair of mirrors that sandwich a crystal that displays a power-dependent refractive index [27]. An external stimulus, called the pump, is applied to the non-linear medium causing a modulation of the cavity resonant frequency (ω_0). If this modulation occurs at the correct frequency, energy may be converted from the pump tone down to the cavity frequency. In the quantum optics example, the
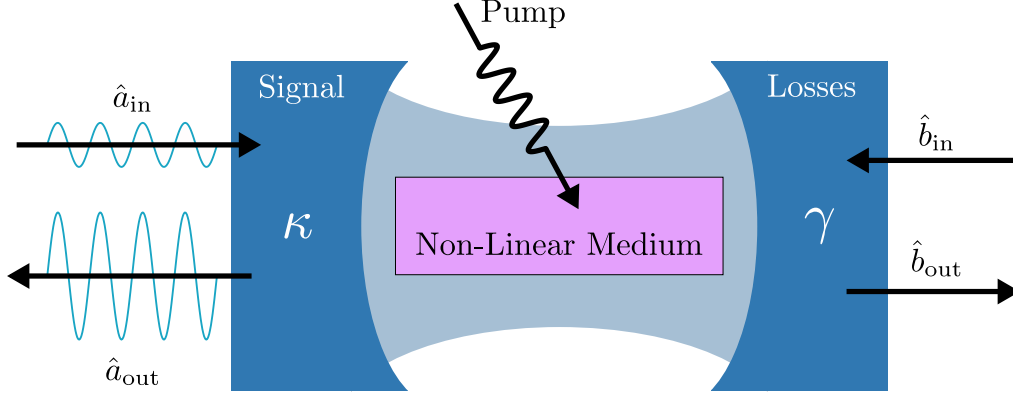
Figure 2.2: The quantum optics model for an ideal degenerate parametric amplifier, adapted from [5] Figure 1(a). A non-linear medium in between two mirrors is driven by an external stimulus called the pump. Photons enter and leave the cavity at the rate κ through one of mirrors, defined as the signal port. The other mirror, called the losses port, removes photons from the cavity and contributes thermal noise at a rate γ.

oscillating refractive index due to the pump modulates the optical path length between the mirrors and consequently the resonant frequency of the cavity.

In this section we present the Hamiltonian for a DPA that operates using a Three Wave Mixing (3WM) process. Although parametric amplification may be realised by a number of mixing processes, 3WM is the simplest and is the mixing process we use in the KIPA developed in this thesis. In quantum optics, 3WM arises in non-linear materials with a second order susceptibility $\chi^{(2)}$. If a pump tone is applied with frequency $\omega_p \sim 2\omega_0$, the second order susceptibility splits the pump photons into two, referred to as the *signal* and the *idler*, such that two conditions are satisfied [29]:

1) *The frequency matching condition*: $\omega_p = \omega_s + \omega_i$, where ω_s and ω_i are the frequencies of the signal and idler photons, respectively.

2) *The phase matching condition*: $\mathbf{k}_p = \mathbf{k}_s + \mathbf{k}_i$, where $\mathbf{k}_p$, $\mathbf{k}_s$ and $\mathbf{k}_i$ are the pump, signal and idler wave-vectors, respectively.

Similar frequency matching and phase matching conditions exist for higher order mixing processes.

The Hamiltonian for the 3WM DPA is given by Milburn and Walls [29]:

$$H = \underbrace{\hbar\omega\hat{a}^\dagger\hat{a}}_{H_0} + \underbrace{i\hbar\chi^{(2)}(\hat{a}^{\dagger 2}\hat{a}_p - \hat{a}^2\hat{a}_p^\dagger)}_{H_1} \tag{2.17}$$

where $\hat{a}_p^\dagger$ and $\hat{a}_p$ are the creation and annihilation operators for the pump field. Here, H_0 is the Hamiltonian for the quantum harmonic oscillator and H_1 captures the pump-cavity interaction, where a pump photon may be exchanged for two cavity photons and vice versa. In practice, the pump contains many more photons than are present in the signal and idler modes allowing us to make the strong pump approximation [27, 5]. In this approximation we replace the pump annihilation operator $\hat{a}_p$ with the coherent tone $\hat{a}_p \rightarrow \alpha e^{-i\omega_p t - i\varphi_p}$, giving the interaction Hamiltonian [27, 5]:

$$H_1 = i\hbar\alpha\chi^{(2)}(\hat{a}^{\dagger 2}e^{-i\omega_p t - i\varphi_p} - \hat{a}^2 e^{i\omega_p t + i\varphi_p}) \tag{2.18}$$

In a frame rotating at close to half the pump frequency $\omega \sim \omega_p/2$, the Hamiltonian becomes time independent [5]:

$$H_{\text{DPA}} = \hbar\left[\Delta\hat{a}^\dagger\hat{a} + i\frac{\xi}{2}\hat{a}^{\dagger 2} - i\frac{\xi^*}{2}\hat{a}^2\right] \tag{2.19}$$

where $\Delta = \omega_0 - \omega_p/2$ is the detuning between the resonance frequency and half the pump, and $\xi = 2\alpha\chi^{(2)}e^{-j\varphi_p}$ is the amplitude of the parametric pump.

To simplify the remainder of this discussion we assume $\varphi_p = 0$ and $\xi \in \mathcal{R}$. For the cavity creation and annihilation operators, we may write down the equations of motion in the Heisenberg picture [27]:

$$\frac{\partial\hat{a}}{\partial t} = \frac{1}{i\hbar}[\hat{a}, H_{1,\text{DPA}}] = \xi\hat{a}^\dagger \tag{2.20}$$

$$\frac{\partial\hat{a}^\dagger}{\partial t} = \frac{1}{i\hbar}[\hat{a}^\dagger, H_{1,\text{DPA}}] = \xi\hat{a} \tag{2.21}$$

Inverting Equations 2.2 and 2.3 we obtain the quadrature operators $\hat{I}$ and $\hat{Q}$ in terms of the creation and annihilation operators:

$$\hat{I} = \frac{1}{2}(\hat{a}^\dagger + \hat{a}) \tag{2.22}$$

$$\hat{Q} = \frac{i}{2}(\hat{a}^\dagger - \hat{a}) \tag{2.23}$$

Combining this with the equations of motion above provides the Heisenberg picture dynamics for the quadrature operators [27]:

$$\frac{\partial\hat{I}}{\partial t} = \xi\hat{I}, \qquad \frac{\partial\hat{Q}}{\partial t} = -\xi\hat{Q} \tag{2.24}$$

Solving these equations, we immediately obtain phase sensitive amplification, where the $\hat{I}$ quadrature is amplified while the $\hat{Q}$ quadrature is deamplified [27]:

$$\langle \hat{I}(t) \rangle = e^{\xi t} \langle \hat{I}(0) \rangle, \qquad \langle \hat{Q}(t) \rangle = e^{-\xi t} \langle \hat{Q}(0) \rangle \qquad (2.25)$$

Similarly, the quadrature variances demonstrate squeezing and are given by [27]:

$$\langle \Delta \hat{I}(t)^2 \rangle = e^{2\xi t} \langle \Delta \hat{I}(0)^2 \rangle, \qquad \langle \Delta \hat{Q}(t)^2 \rangle = e^{-2\xi t} \langle \Delta \hat{Q}(0)^2 \rangle \qquad (2.26)$$

The frequency matching and phase matching conditions provide us with a more intuitive explanation for the phase sensitive amplification produced by an ideal DPA. In the frame rotating at $\omega_p/2$, the signal and idler map onto the same frequency, due to the frequency matching condition. In telecommunications terms, the signal and idler form two side-bands about $\omega_p/2$ which are mapped to the same frequency when we demodulate at $\omega_p/2$, equivalent to moving to the rotating frame. Now, the phase matching condition restricts the signal and idler phases to be locked with the pump phase. Therefore, depending on the phase of the input the signal and idler tones will constructively or destructively interfere, giving rise to phase sensitive gain.

We have shown that the degenerate parametric amplifier may be realised with a cavity and suitable non-linear medium. In the following sections we present the theory of microwave cavities using the framework of Circuit Quantum Electrodynamics (cQED), and the phenomenon of kinetic inductance, the non-linear medium employed by the KIPA.

2.3   The Quantum LC Resonator

The cavity in our device may be modelled by a microwave frequency LC resonator, with a non-linear inductance. To begin, we formulate the physics of the linear LC circuit for quantised microwave fields, which we later build on to describe the distributed linear LC resonator, and ultimately the Hamiltonian for the non-linear cavity of the KIPA.

In terms of the current (I) and voltage (V), the current flowing through a parallel LC resonator (as depicted in Figure 2.3a) is given by [30]:

$$I = C\dot{V} \qquad (2.27)$$

Re-written in terms of the magnetic flux in the loop $\Phi = LI$ and the charge on the capacitor $Q = CV$, we obtain

$$\Phi = L\dot{Q} \qquad (2.28)$$
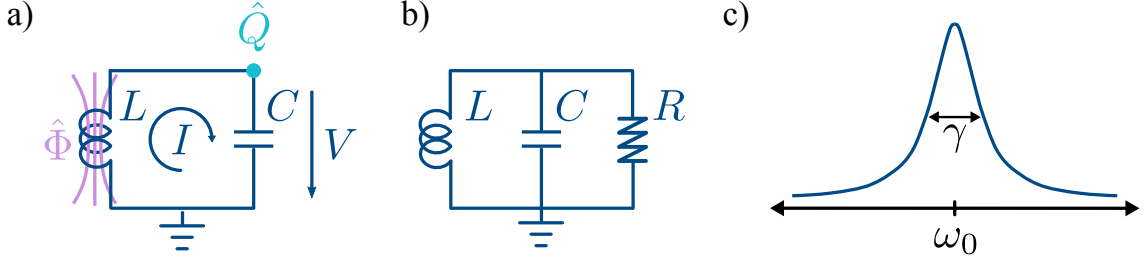
Figure 2.3: (a) The ideal LC resonator, labelled with the quantised flux and charge variables. (b) The parallel RLC circuit, where R is included to model internal cavity losses. (c) The frequency response of the RLC resonator, characterised by a line-width γ that corresponds to the loss rate of the system.

Here, Q and Φ are canonically conjugate variables, analogous to position and momentum in a mechanical system. Using the expressions for energy stored in an inductor and capacitor, the Lagrangian for this system is as follows [31]:

$$\mathcal{L}(\Phi, Q) = \frac{1}{2L}\Phi^2 - \frac{1}{2C}Q^2 \tag{2.29}$$

capturing the dynamics of the transfer of energy between the inductor and capacitor. In this definition of the Lagrangian, the charge Q is taken as the coordinate. The conjugate momentum can found from the Lagrangian:

$$p = \frac{\partial \mathcal{L}}{\partial \dot{Q}} \tag{2.30}$$

Substituting Equation 2.28 into the Lagrangian (2.29) and evaluating the conjugate momentum above (2.30) yields the flux $p = \Phi$, as expected. Although trivial to write down, we derive the classical Hamiltonian using the Legendre transformation, a step that will appear throughout this thesis:

$$\mathcal{H}(\Phi, Q) = \dot{Q}\frac{\partial \mathcal{L}}{\partial \dot{Q}} - \mathcal{L} \tag{2.31}$$

$$= \dot{Q}L\dot{Q} + \frac{1}{2C}Q^2 - \frac{1}{2L}\Phi^2 \tag{2.32}$$

$$= \frac{1}{2L}\Phi^2 + \frac{1}{2C}Q^2 \tag{2.33}$$

To obtain the quantum description for the LC resonator, we replace the classical

27

variables (Φ, Q) and the Hamiltonian function with operators [31]:

$$\Phi \rightarrow \hat{\Phi} \tag{2.34}$$

$$Q \rightarrow \hat{Q} \tag{2.35}$$

$$\mathcal{H} \rightarrow \hat{\mathcal{H}} \tag{2.36}$$

such that the commutator of the conjugate quantised flux ($\hat{\Phi}$) and quantised charge ($\hat{Q}$) operators satisfy the relation:

$$[\hat{Q}, \hat{\Phi}] = i\hbar \tag{2.37}$$

as is required in the equivalent quantum mechanical description for position and momentum operators. To simplify notation, we denote the quantum Hamiltonian operator using $H = \hat{\mathcal{H}}$ for the remainder of this thesis.

The quantum LC resonator behaves as a cavity, which may be populated by electromagnetic energy at the fundamental resonance frequency of the circuit: $\omega_0 = 1/\sqrt{LC}$. We can equate the LC circuit Hamiltonian with the Hamiltonian for the quantum harmonic oscillator in terms of the photon creation and annihilation operators $\hat{a}^\dagger$ and $\hat{a}$ [31]:

$$H = \frac{1}{2L}\hat{\Phi}^2 + \frac{1}{2C}\hat{Q}^2 \tag{2.38}$$

$$= \hbar\omega_0(\hat{a}^\dagger\hat{a} + {}^1\!/_2) \tag{2.39}$$

Where we have used the following expansion of the ladder operators $\hat{a}$ and $\hat{a}^\dagger$ on the flux and charge operators:

$$\hat{a} = \frac{1}{\sqrt{2\hbar Z_0}}(\hat{\Phi} + iZ_0\hat{Q}) \tag{2.40}$$

$$\hat{a}^\dagger = \frac{1}{\sqrt{2\hbar Z_0}}(\hat{\Phi} - iZ_0\hat{Q}) \tag{2.41}$$

Here, $Z_0 = \sqrt{L/C}$ is the characteristic impedance of the circuit. It is straightforward to verify that the operators $\hat{a}$ and $\hat{a}^\dagger$ satisfy the bosonic commutation relation:

$$[\hat{a}, \hat{a}^\dagger] = 1 \tag{2.42}$$

So far we have assumed an ideal system without loss, free from any undesirable coupling to the environment (also referred to as the bath). In practice, photon losses occur and may be modelled by an equivalent parallel resistance (Figure 2.3b), giving the resonance an "internal quality factor" $Q_i = \omega_0 RC$ with associated loss rate

$\gamma = \omega_0/Q_i = 1/RC$ [30]. The equivalent resistance loss model captures first-order/linear photon losses. While higher order loss mechanisms exist (e.g. two photon loss [32]), the first order loss model works well in practice for small signal powers [5], and losses are approximated to the first order for the remainder of this thesis. As such, we imply a small parallel resistance for the remaining circuit models presented henceforth.

In order for quantum effects to become significant in an LC resonator, two conditions must be satisfied: the resonator must be well isolated from its environment such that its energy level broadenings are narrower than their separation, and, the energy separation between the eigenstates of H must be larger than the thermal energy of the system [33].

The former condition is equivalent to requiring a high internal quality factor, where the loss rate γ is considerably slower than the system dynamics. The KIPA operates in the microwave domain with a resonant frequency $\omega_0 \sim 2\pi \cdot 7\,\text{GHz}$ and is fabricated from the superconductor NbTiN. High internal quality factors in superconducting microwave resonators are frequently observed in the laboratory, ranging from $Q_i \sim 10^3$ to 10^8 [34, 33], and are sufficiently large to not prohibit the experimental observation of quantum phenomena.

To satisfy the second condition, we require $\hbar\omega_0 \gg k_B T$. For $\omega_0 \sim 2\pi \cdot 7\,\text{GHz}$, this limit corresponds to a system temperature below $T = 336\,\text{mK}$. Given that the experiments presented in this thesis are performed at $T = 20\,\text{mK}$, the cavity of the KIPA is in the ground state $|0\rangle$ when the system is at thermal equilibrium. After the cavity has been populated with photons due to some past experimental stimulus, the resonator will relax back to the ground state on a timescale of order $T_\gamma = 1/\gamma$.

2.4 The Quantum $\lambda/4$ Resonator

In the microwave frequency range, coplanar waveguide (CPW) resonators are popular structures used in circuit cQED experiments due to their manufacturability and simple electromagnetic mode distributions. Further, if realised using superconductors, extremely low losses are achievable. The dominant loss mechanism in superconducting CPW resonators is due to the absorption of microwave photons by Two Level Systems (TLS), typically concentrated on the surface of the substrate [35]. Engineering considerations to minimise coupling to TLSs, such as overetching the substrate, have yielded internal
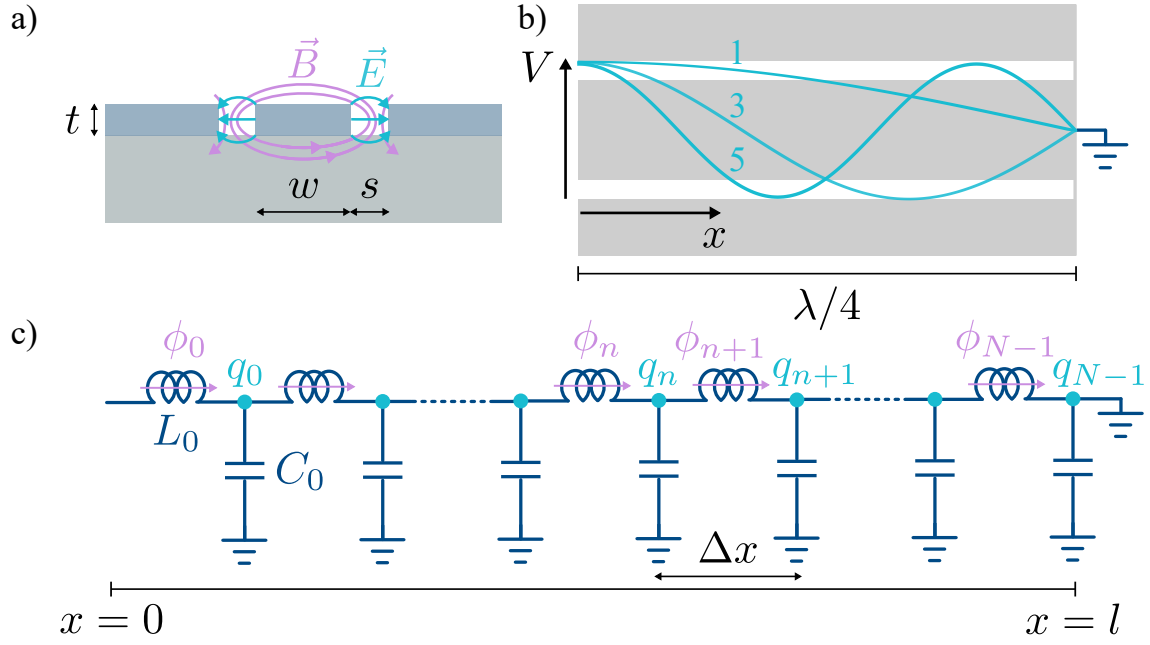
Figure 2.4: (a) A cross-section of coplanar waveguide with center line width w, gap width s and thickness t. Electric ($\vec{E}$) and magnetic ($\vec{B}$) field distributions are illustrated. (b) The geometry of a $\lambda/4$ resonator with centre line grounded at one end. The voltage V as a function of position x is overlaid for the 1st, 3rd and 5th harmonics. (c) The telegrapher circuit model for the $\lambda/4$ resonator, where each inductor-capacitor pair approximates the response of a small length Δx of the distributed resonator.

quality factors as high as $Q_i = 10^6$ at X-band frequencies [36].

The coplanar waveguide is a type of transmission line created from a strip of metal of width w sandwiched between two 'large' grounded conductive planes a distance s away, as illustrated in Figure 2.4a. The conductor rests on a dielectric substrate with relative permittivity ϵ_r, while the surface of the conductor is exposed to air or in our case vacuum. Typically, the thickness of the conductor t is much smaller than the size of the gap or the width of the central conductor $t \ll w, s$, giving the circuit an equivalent permittivity of $\epsilon' = \epsilon_0(1 + \epsilon_r)/2$, where ϵ_0 is the permittivity of free space [30]. The coplanar waveguide supports a quasi transverse electromagnetic (TEM) mode where the electric field concentrates between the central conductor and the ground planes, and the magnetic field circulates around the central conductor, as shown in Figure 2.4a [30]. When fabricated with a superconducting film and low loss dielectric substrate such as Sapphire or Silicon, the voltage and current distributions along the centre line are 90° out of phase, and are related by the characteristic impedance of the CPW $Z_{cpw} = \sqrt{L'/C'}$, where L' and C' are the inductance and capacitance per unit length, respectively. Electromagnetic radiation propagates along the CPW at a velocity $v = c\sqrt{\epsilon'/\epsilon_0}$, where c is the speed of light. For a Silicon substrate at low temperatures $\epsilon' = \epsilon_0(1 + 11.45)/2$, corresponding to a phase velocity of $v = 1.2 \times 10^8$ m/s.

Microwave resonators are realised by imposing boundary conditions on a fixed length l of coplanar waveguide [30]. To illustrate, we present the $\lambda/4$ resonator (Figure 2.4b), the same style of resonator that features in the KIPA. The quarter wavelength resonator is a formed by a length of CPW $l = \lambda/4$ with one end shorted to ground. The resonator supports standing waves of odd multiples of the fundamental frequency $f_0 = v/\lambda = v/4l$ where the boundary condition requires the electric field and voltage to be zero at the shorted end of the resonator as shown in Figure 2.4. For a 4 mm long strip on a Silicon substrate, the CPW will resonate at 7.5 GHz, 15 GHz, 22.5 GHz, etc. In this work, we are only concerned with the fundamental resonance f_0. To obtain the quantum mechanical description of the $\lambda/4$ resonator we adapt the Hamiltonian derivation for a $\lambda/2$ resonator presented by Blais *et al.* [33].

Using the telegrapher model, we may represent the distributed resonator as a string of small inductances L_0 in series interleaved with a parallel array of capacitances C_0, as illustrated in Figure 2.4c [30]. Let q_n be the charge on the n-th circuit node, and ϕ_n be

the total quantised flux entering the n-th circuit node, as illustrated for the flux in Figure 2.4c. Applying Kirchhoff's laws in terms of the magnetic flux and charge, we have:

$$\frac{1}{L_0}(\phi_{n+1} - \phi_n) = \dot{q}_n \quad \Rightarrow \quad \Delta\phi_n = L_0 \dot{q}_n \tag{2.43}$$

and,

$$\frac{1}{C_0}(q_{n+1} - q_n) = \dot{\phi}_n \quad \Rightarrow \quad \Delta q_n = C_0 \dot{\phi}_n \tag{2.44}$$

where, $\Delta\phi_n = \phi_{n+1} - \phi_n$ and $\Delta q_n = q_{n+1} - q_n$. The Lagrangian associated with this circuit model is:

$$\mathcal{L}_{\lambda/4} = \sum_{n=0}^{N-1} \left[\frac{1}{2L_0}\phi_n^2 - \frac{1}{2C_0}q_n^2 \right] \tag{2.45}$$

To obtain the telegrapher equations, we set $L_0 = L'\Delta x$ and $C_0 = C'\Delta x$, where L' and C' are the inductance and capacitance per unit length, respectively, and $\Delta x = l/N$. Further, we define Q_n to be the cumulative charge on the n-th circuit node:

$$Q_n = \sum_{i=0}^{n} q_i \tag{2.46}$$

and Φ_n to be the cumulative flux on the n-th circuit node:

$$\Phi_n = \sum_{i=0}^{n} \phi_i \tag{2.47}$$

Taking the limit of $\Delta x \to 0$ and $N \to \infty$ such that $N\Delta x = l$, and substituting the cumulative charge and flux variables from Equations 2.46 and 2.47, the Kirchhoff Equations 2.43 and 2.44 become the telegrapher equations:

$$\frac{\Delta\Phi_n}{\Delta x} = L'\dot{Q}_n \quad \to \quad \frac{\partial\Phi}{\partial x} = L'\frac{\partial Q}{\partial t} \tag{2.48}$$

$$\frac{\Delta Q_n}{\Delta x} = C'\dot{\Phi}_n \quad \to \quad \frac{\partial Q}{\partial x} = C'\frac{\partial\Phi}{\partial t} \tag{2.49}$$

where $\Delta\Phi_n = \Phi_{n+1} - \Phi_n$ and $\Delta Q_n = Q_{n+1} - Q_n$.

Differentiating Equation 2.49 with respect to x and substituting Equation 2.48, we arrive at the wave equation for the cumulative charge:

$$v_0^2 \frac{\partial^2 Q(x,t)}{\partial x^2} - \frac{\partial^2 Q(x,t)}{\partial t^2} = 0 \tag{2.50}$$

where $v_0 = 1/\sqrt{L'C'}$ is the microwave phase velocity, or equivalently, the speed of light in the CPW. Applying the usual separation of variables, we write the solutions to Equation 2.50 as the Fourier expansion of the resonant modes of the circuit:

$$Q(x,t) = \sum_{m=0}^{\infty} A_m u_m(x) \mathcal{Q}_m(t) \tag{2.51}$$

If we let ω_m be the frequency of the m-th mode then a classical solution for the temporal component is $\mathcal{Q}_m(t) = \cos(\omega_m t + \theta_m)$ and the spatial component is $u_m(x) = \cos(k_m x + \varphi_m)$, with $k_m = \omega_m/v_0$. Going forward, we will assume no particular form of the solution for $\mathcal{Q}_m(t)$. For the $\lambda/4$ resonator the boundary conditions require:

$$\Phi(0,t) = 0 \Rightarrow \dot{Q}(0,t) = 0 \qquad \text{(open circuit)} \tag{2.52}$$

$$q(l,t) = 0 \Rightarrow \left.\frac{\partial Q}{\partial x}\right|_{x=l} = 0 \qquad \text{(short circuit end)} \tag{2.53}$$

giving $\varphi_m = k_m l$ and $\omega_m = 2\pi \cdot (2m+1)v_0/4l = 2\pi \cdot (2m+1)f_0$. In other words, the resonant frequencies are odd multiples of $f_0 = v/4l$, as predicted. The spatial component becomes:

$$u_m(x) = \cos\left(2\pi \frac{2m+1}{4l}(x-l)\right) \tag{2.54}$$

To simplify the derivation of the Hamiltonian, we normalise the mode functions by choosing the coefficients A_m such that [33]:

$$\frac{1}{l}\int_0^l A_m u_m(x) A_{m'} u_{m'}(x)\,dx = \delta_{mm'} \tag{2.55}$$

giving $A_m = \sqrt{2}$.

Returning now to the Lagrangian, we re-write the charge and flux variables in terms of the new cumulative charge/flux coordinates and apply the substitution from the first telegrapher Equation 2.48:

$$\mathcal{L}_{\lambda/4} = \frac{\Delta x}{2}\sum_{n=0}^{N-1} \frac{1}{L'}\left(\frac{\Delta\Phi_n}{\Delta x}\right)^2 - \frac{1}{C'}\left(\frac{\Delta Q_n}{\Delta x}\right)^2 \tag{2.56}$$

$$= \frac{\Delta x}{2}\sum_{n=0}^{N-1} L'\dot{Q}_n^2 - \frac{1}{C'}\left(\frac{\Delta Q_n}{\Delta x}\right)^2 \tag{2.57}$$

The equation is now a function of the cumulative charges Q_n and their derivatives. In the limit of $\Delta x \to 0$ and $N \to \infty$, as was taken to derive the telegrapher equations, we arrive at the form:

$$\mathcal{L}_{\lambda/4} = \frac{1}{2}\int_0^l L'\left(\frac{\partial Q}{\partial t}\right)^2 - \frac{1}{C'}\left(\frac{\partial Q}{\partial x}\right)^2 dx \tag{2.58}$$

Substituting the Fourier series solution for $Q(x,t)$ (Equation 2.51), the Lagrangian simplifies to:

$$\mathcal{L}_{\lambda/4} = \frac{1}{2} \sum_m L' \dot{\mathcal{Q}}_m^2 \int_0^l A_m^2 \cos^2(k_m x + \varphi_m) dx$$
$$- \frac{1}{C'} \left(\frac{\omega_m}{v_0} \right)^2 \mathcal{Q}_m^2 \int_0^l A_m^2 \sin^2(k_m x + \varphi_m) dx \tag{2.59}$$

$$= \frac{1}{2} \sum_m L_T \dot{\mathcal{Q}}_m^2 - L_T \omega_m^2 \mathcal{Q}_m^2 \tag{2.60}$$

where $L_T = lL'$ is the total inductance of the resonator. The time-dependent mode amplitude $\mathcal{Q}_m$ (which has units of a charge) plays the role of a position, with the conjugate momentum then given as (see Equation 2.30):

$$\mathcal{P}_m = \frac{\partial \mathcal{L}_{\lambda/4}}{\partial \dot{\mathcal{Q}}_m} = L_T \dot{\mathcal{Q}}_m \tag{2.61}$$

with units of a magnetic flux.

Applying the Legendre transformation to Equation 2.58, we obtain the Hamiltonian:

$$\mathcal{H} = \int_0^l \dot{Q} \frac{\partial \mathcal{L}_{\lambda/4}}{\partial \dot{Q}} dx - \mathcal{L}_{\lambda/4} \tag{2.62}$$

$$= \int_0^l L' \frac{\partial Q}{\partial t}^2 dx - \left(\frac{1}{2} \int_0^l L' \left(\frac{\partial Q}{\partial t} \right)^2 - \frac{1}{C'} \left(\frac{\partial Q}{\partial x} \right)^2 dx \right) \tag{2.63}$$

$$= \frac{1}{2} \int_0^l \frac{1}{C'} \left(\frac{\partial Q}{\partial x} \right)^2 + L' \left(\frac{\partial Q}{\partial t} \right)^2 dx \tag{2.64}$$

Inserting once again the mode expansion for $Q(x,t)$, we find:

$$\mathcal{H} = \frac{1}{2} \sum_m L_T \omega_m^2 \mathcal{Q}_m^2 + L_T \dot{\mathcal{Q}}_m^2 \tag{2.65}$$

$$= \frac{1}{2} \sum_m L_T \omega_m^2 \mathcal{Q}_m^2 + \frac{1}{L_T} \mathcal{P}_m^2 \tag{2.66}$$

The Hamiltonian reduces to a sum of LC oscillator Hamiltonians that oscillate at the harmonics ω_m and each have a fictitious mass of L_T. The Hamiltonian for the quantum $\lambda/4$ resonator is obtained in the usual way, by promoting the conjugate variables $\mathcal{Q}_m$ and $\mathcal{P}_m$ to the operators:

$$\mathcal{Q}_m \rightarrow \hat{Q} = i\sqrt{\frac{\hbar}{2Z_m}} (\hat{a}_m^\dagger - \hat{a}_m) \tag{2.67}$$

$$\mathcal{P}_m \rightarrow \hat{\Phi} = \sqrt{\frac{\hbar Z_m}{2}} (\hat{a}_m^\dagger + \hat{a}_m) \tag{2.68}$$
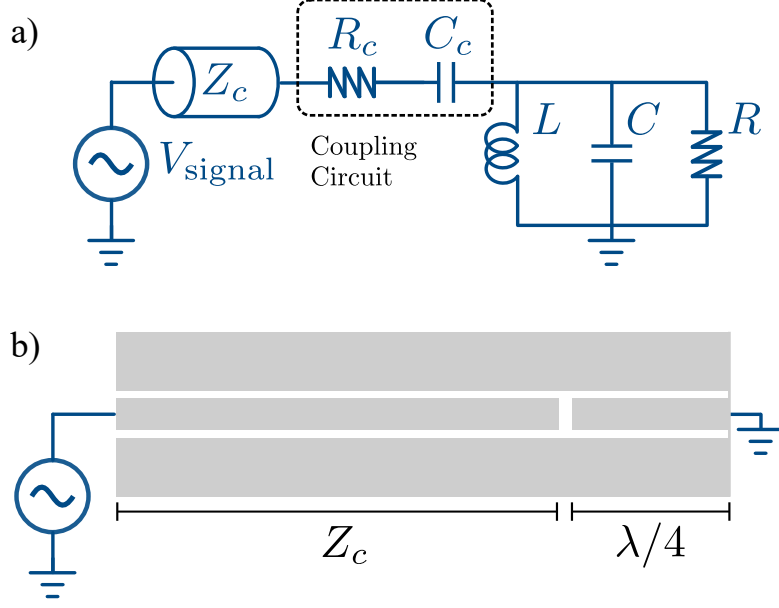
Figure 2.5: (a) The LCR resonator, capacitvely coupled to the input source via a transmission line with characteristic impedance Z_c. The coupling circuit is emphasised, but may be substituted by an arbitrary circuit with transfer function $T(z)$. (b) A distributed $\lambda/4$ resonator capacitvely coupled to a CPW transmission line with characteristic impedance Z_c.

where we have defined the mode impedance $Z_m = L_T \omega_m$. This provides the familiar Fock basis Hamiltonian:

$$H = \sum_{m=0}^{\infty} \hbar\omega_m (\hat{a}_m^\dagger \hat{a}_m + {}^1\!/_2) \tag{2.69}$$

2.5 Coupling to the Resonator

The resonators we have presented so far are totally isolated from their environment. To build a useful amplifier, we need to get photons (signal) into the cavity and back out of it again. Typically, this is achieved using a capacitive coupler, as presented in the circuit model shown in Figure 2.5a. In the case of CPW resonators, a transmission line transports the signal to the resonator, where typically a small gap defines a capacitance between the transmission line and the resonator [30], as illustrated in Figure 2.5b. When observed through the transmission line, the additional capacitance (C_c), any loss (R_c), and the characteristic impedance (Z_c) of the transmission line will load the circuit and

increase the observed line-width relative to γ, the line-width of the isolated resonance. The observed total quality factor Q_t may be decomposed into the internal quality factor $Q_i = \omega_0/\gamma$ introduced earlier and a so-called coupling quality factor $Q_c = \omega_0/\kappa$, where ω_0 is the resonance frequency (e.g. the fundamental frequency of a $\lambda/4$ resonator) and κ is defined as the rate at which photons enter and leave the cavity, known as the coupling rate [30]. The total quality factor is given by:

$$\frac{1}{Q_t} = \frac{1}{Q_c} + \frac{1}{Q_i} \tag{2.70}$$

A resonator is said to be: *over-coupled* if $Q_i \gg Q_c$, *under-coupled* if $Q_i \ll Q_c$, and *critically-coupled* if $Q_i \approx Q_c$ [30]. A more detailed circuital analysis of the capacitvely coupled LC resonator may be found in [37].

Although the capacitive coupler is the simplest coupling mechanism, coupling to a resonator may be achieved with any coupling circuit that influences the rate that photons enter and leave the cavity. However, in order to measure quantum effects in practice we require the coupling rate κ to not be excessively faster than the dynamics of the system under observation, as was required for the loss rate γ. Conversely, designing κ to be small will limit the response time of the resonator and exacerbate cavity ring-down. In the case of the KIPA, we define the coupling quality factor Q_c using a band-stop filter, centred about the resonance frequency. The depth of the band-stop region may be used to design the coupling rate κ, as will be discussed in greater detail in Section 3.1.2.

In the presence of a coupling circuit, the boundary conditions (e.g. Equations 2.52, 2.53) of the $\lambda/4$ resonator wave equation (Equation 2.50) change, shifting the resonance frequency and modifying the amplitudes and phases of the mode functions [33]. A complete quantum mechanical treatment of the loaded circuit is beyond the scope of this thesis. Instead, we adopt the boundary conditions of the isolated resonator as an approximation, and turn to input-output theory for a quantum mechanical description of a resonator with an input port and loss channel.

2.6   Input Output Theory

The field operators $\hat{a}$, $\hat{\Phi}$ and $\hat{Q}$ and Hamiltonian H so far describe the intracavity field dynamics. In the experimental setting we stimulate the resonator with an input field operator $\hat{a}_{\text{in}}$ and measure a reflected response $\hat{a}_{\text{out}}$ that enter and exit the cavity via the
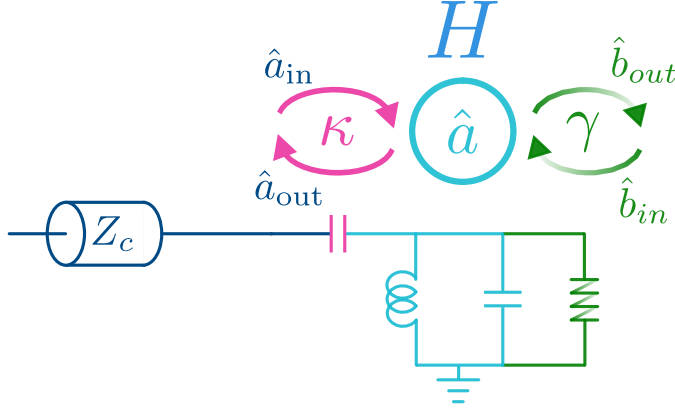
Figure 2.6: The single port input-output theory system, with input and output fields $\hat{a}_{\mathrm{in}}$ and $\hat{a}_{\mathrm{out}}$, intracavity field operator $\hat{a}$, and bath input and output fields $\hat{b}_{\mathrm{in}}$ and $\hat{b}_{\mathrm{out}}$. The input field is coupled to the cavity at rate κ, and the cavity to the bath at rate γ. The accompanying circuit is coloured according to the correspondence with the associated fields and coupling constants. The bath continuum is coupled to the circuit via the resistor.

coupling circuit. For example, a Vector Network Analyser (VNA) measures the reflection parameter $\Gamma(\omega) = \langle \hat{a}_{\mathrm{in}} \rangle / \langle \hat{a}_{\mathrm{out}} \rangle$. To obtain a classical description of the microwave response we would typically adopt a scattering matrix approach [30].

Input-Output theory, developed by Gardiner and Collett [38], extends the scattering matrix formalism to the quantum regime. Let H be the Hamiltonian written in terms of the creation and annihilation operators $\hat{a}^\dagger$ and $\hat{a}$, where H is coupled to the bath at rate γ, used to model the losses in the system, and input field $\hat{a}_{\mathrm{in}}$ at rate κ (see Figure 2.6). Gardiner and Collett provide the following Heisenberg picture master equation to describe the system:

$$\frac{\partial \hat{a}(t)}{\partial t} = \frac{[\hat{a}, H]}{i\hbar} - \bar{\kappa}\hat{a}(t) + \sqrt{\kappa}\hat{a}_{\mathrm{in}} + \sqrt{\gamma}\hat{b}_{\mathrm{in}}(t) \qquad (2.71)$$

where $\bar{\kappa} = (\gamma + \kappa)/2$. The output field operator $\hat{a}_{\mathrm{out}}$ is then given by the input-output relation:

$$\hat{a}_{\mathrm{out}}(t) - \hat{a}_{\mathrm{in}}(t) = \sqrt{\kappa}\hat{a}(t) \qquad (2.72)$$

Consider now the quantum LC resonator with the quantum harmonic oscillator Hamiltonian given by Equation 2.39. We re-write Equation 2.71 in the Fourier domain using:

$$\hat{a}[\omega] = \frac{1}{\sqrt{2\pi}} \int_{-\infty}^{\infty} e^{i\omega t} \hat{a}(t) d\omega \tag{2.73}$$

which gives:

$$-i\omega\hat{a}[\omega] = -\frac{i}{\hbar}\left[\hat{a}[\omega], \hbar\omega_0\hat{a}^\dagger[\omega]\hat{a}[\omega]\right] - \bar{\kappa}\hat{a}[\omega] + \sqrt{\kappa}\hat{a}_{\text{in}}[\omega] + \sqrt{\gamma}\hat{b}_{\text{in}}[\omega] \tag{2.74}$$

$$-i\omega\hat{a} = -i\omega_0\hat{a} - \bar{\kappa}\hat{a} + \sqrt{\kappa}\hat{a}_{\text{in}} + \sqrt{\gamma}\hat{b}_{\text{in}} \tag{2.75}$$

Substituting for $\hat{a}$ using the input output relation (Equation 2.72) yields the output field operator in terms of the input and bath fields:

$$-i\omega(\hat{a}_{\text{out}} - \hat{a}_{\text{in}}) = -(\bar{\kappa} + i\omega_0)(\hat{a}_{\text{out}} - \hat{a}_{\text{in}}) + \kappa\hat{a}_{\text{in}} + \sqrt{\frac{\gamma}{\kappa}}\hat{b}_{\text{in}} \tag{2.76}$$

$$\Rightarrow \hat{a}_{\text{out}} = \left(\frac{\kappa}{\bar{\kappa} - i(\omega - \omega_0)} - 1\right)\hat{a}_{\text{in}} + \frac{\sqrt{\gamma/\kappa}}{\bar{\kappa} - i(\omega - \omega_0)}\hat{b}_{\text{in}} \tag{2.77}$$

Treating the bath input field $\hat{b}_{\text{in}}$ as a thermal state such that $\langle\hat{b}_{\text{in}}\rangle = 0$, we retrieve the expression for the reflection parameter:

$$\Gamma[\omega] = \frac{\langle\hat{a}_{\text{out}}[\omega]\rangle}{\langle\hat{a}_{\text{in}}[\omega]\rangle} \tag{2.78}$$

$$= \frac{\kappa}{\bar{\kappa} - i(\omega - \omega_0)} - 1 \tag{2.79}$$

This matches the expression for the reflection parameter of a lumped element LC resonator, obtained using the scattering matrix approach [30].

We may now apply the same mathematics to the ideal DPA Hamiltonian (Equation 2.19) to obtain an equation relating its input and output fields. We follow the derivation of Samuel Boutin [39], first by writing the master equation in the Fourier domain as before:

$$-i\omega\hat{a} = -\left(\bar{\kappa}\hat{a} + i\Delta\hat{a} + i\frac{\xi}{2}\left[\hat{a}, \hat{a}^{\dagger 2}\right] + i\frac{\xi}{2}\left[\hat{a}, \hat{a}^2\right]\right) + \sqrt{\kappa}\hat{a}_{\text{in}} + \sqrt{\gamma}\hat{b}_{\text{in}} \tag{2.80}$$

$$-i\omega\hat{a} = -((\bar{\kappa} + i\Delta)\hat{a} + i\xi\hat{a}^\dagger) + \sqrt{\kappa}\hat{a}_{\text{in}} + \sqrt{\gamma}\hat{b}_{\text{in}} \tag{2.81}$$

Next, we take the Hermitian conjugate of both sides. Note that in the Fourier domain $(\hat{a}[\omega])^\dagger = \hat{a}^\dagger[-\omega]$. To simplify notation the frequency reversal is implied:

$$i\omega\hat{a}^\dagger = -((\bar{\kappa} - i\Delta)\hat{a}^\dagger - i\xi^*\hat{a}) + \sqrt{\kappa}\hat{a}^\dagger_{\text{in}} + \sqrt{\gamma}\hat{b}^\dagger_{\text{in}} \tag{2.82}$$

Combined with Equation 2.81, we obtain the matrix equation:

$$i\omega \begin{pmatrix} -\hat{a} \\ \hat{a}^\dagger \end{pmatrix} = \begin{pmatrix} -i\Delta - \bar{\kappa} & -i\xi \\ i\xi^* & i\Delta - \bar{\kappa} \end{pmatrix} \begin{pmatrix} \hat{a} \\ \hat{a}^\dagger \end{pmatrix} + \sqrt{\kappa} \begin{pmatrix} \hat{a}_{\text{in}} \\ \hat{a}_{\text{in}}^\dagger \end{pmatrix} + \sqrt{\gamma} \begin{pmatrix} \hat{b}_{\text{in}} \\ \hat{b}_{\text{in}}^\dagger \end{pmatrix} \qquad (2.83)$$

$$\Rightarrow \begin{pmatrix} \hat{a} \\ \hat{a}^\dagger \end{pmatrix} = -\sqrt{\kappa} \begin{pmatrix} -i\Delta + \bar{\kappa} + i\omega & -i\xi \\ i\xi^* & i\Delta - \bar{\kappa} - i\omega \end{pmatrix}^{-1} \left[\begin{pmatrix} \hat{a}_{\text{in}} \\ \hat{a}_{\text{in}}^\dagger \end{pmatrix} + \sqrt{\frac{\gamma}{\kappa}} \begin{pmatrix} \hat{b}_{\text{in}} \\ \hat{b}_{\text{in}}^\dagger \end{pmatrix} \right] \qquad (2.84)$$

$$= -\frac{\sqrt{\kappa}}{D[\omega]} \begin{pmatrix} -i\Delta + \bar{\kappa} + i\omega & -i\xi \\ i\xi^* & i\Delta - \bar{\kappa} - i\omega \end{pmatrix} \left[\begin{pmatrix} \hat{a}_{\text{in}} \\ \hat{a}_{\text{in}}^\dagger \end{pmatrix} + \sqrt{\frac{\gamma}{\kappa}} \begin{pmatrix} \hat{b}_{\text{in}} \\ \hat{b}_{\text{in}}^\dagger \end{pmatrix} \right] \qquad (2.85)$$

where $D[\omega] = \Delta^2 + (\bar{\kappa} - i\omega)^2 - |\xi|^2$. Substituting the input output relation (Equation 2.72) gives the input output equation for the ideal DPA [5]:

$$\hat{a}_{\text{out}}[\omega] = g_S[\omega]\hat{a}_{\text{in}}[\omega] + g_I[\omega]\hat{a}_{\text{in}}^\dagger[-\omega] + \sqrt{\frac{\gamma}{\kappa}}\left[(g_S[\omega] + 1)\hat{b}_{\text{in}}[\omega] + g_I[\omega]\hat{b}_{\text{in}}^\dagger[-\omega]\right] \qquad (2.86)$$

where we make the frequency reversal explicit, and:

$$g_S[\omega] = \frac{\kappa\bar{\kappa} - i\kappa(\Delta + \omega)}{D[\omega]} - 1, \quad \text{and} \quad g_I[\omega] = \frac{-i\xi\kappa}{D[\omega]} \qquad (2.87)$$

2.7 The JPA

The Josephson Parametric Amplifier (JPA) represents the state of the art for microwave frequency squeezing. Realised from both distributed microwave resonators [28, 12] and lumped element resonators [40, 22, 41, 6], the JPA consists of one or more Superconducting Quantum Interference Devices (SQUIDs), each formed by a parallel pair of Josephson junctions (see Figure 2.7a). Constructed from a pair of superconducting plates separated by a thin insulator, the Josephson junctions provide the non-linearity required for parametric amplification in the form of a non-linear inductance. Cooper pairs may tunnel through the thin insulating barrier, with the junction current set by the phase difference φ between the superconducting condensates on either side of the barrier [33]. The Josephson junction super-current and voltage are related to the phase difference φ by the DC and AC Josephson relations [8, 33]:

$$I = I_c \sin(\varphi), \qquad V = \frac{\Phi_0}{2\pi}\frac{\partial\varphi}{\partial t} \qquad (2.88)$$

where I_c is the critical current of the Josephson junction, and $\Phi_0 = h/2e$ is the flux quantum.
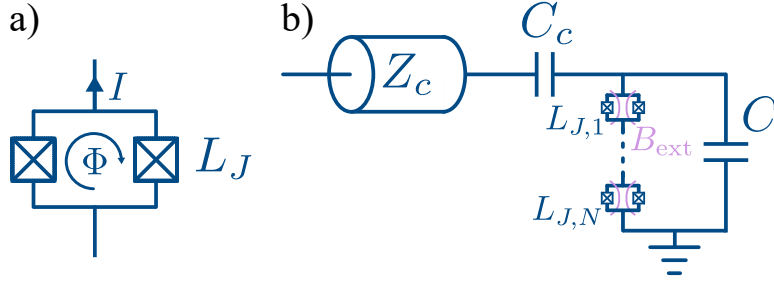
Figure 2.7: (a) The SQUID: a parallel pair of Josephson junctions with equivalent inductance L_J. The SQUID flux and current are depicted. (b) The equivalent circuit for the JPA, whereby $N \geq 1$ SQUIDs replace the inductor in the quantum LC resonator. An externally applied magnetic field B_{ext} is depicted and is one of the methods for pumping the JPA, called the flux pump.

Two Josephson junctions in a loop form a SQUID, where the current flowing through each junction is related to the flux threading the loop Φ. Configured as a SQUID, the phase difference is related to the flux by [33]:

$$\varphi(t) = 2\pi \frac{\Phi(t)}{\Phi_0} (\text{mod} \, 2\pi) \tag{2.89}$$

Applying the Josephson relation for current, and using the relation $\Phi = LI$ we find that the SQUID has a flux-dependent inductance given by [33]:

$$L_J(\Phi) = \left(\frac{\partial I}{\partial \Phi} \right)^{-1} = \frac{\Phi_0}{2\pi I_c} \sec \left(2\pi \frac{\Phi}{\Phi_0} \right) \tag{2.90}$$

The Josephson inductance may be alternatively expressed as a Taylor series expansion with respect to the current I flowing through the terminals of the SQUID [5]:

$$L_J(I) = L_{J,0} \left[1 + \frac{1}{6} \left(\frac{I}{I_c} \right)^2 + \cdots \right] \tag{2.91}$$

The microwave resonance in a JPA is formed by capacitively shunting the non-linear inductance of one or more SQUIDs to ground, as illustrated by the equivalent circuit for a JPA in Figure 2.7b. In the absence of a flux or current in the SQUID, the JPA behaves as the microwave resonators presented earlier in Sections 2.3 and 2.4. To produce parametric amplification the SQUIDs are pumped with a microwave current, thereby modulating the Josephson inductance (Equation 2.91), or via an external line that generates a flux through the SQUIDs (Equation 2.90). The former pumping scheme enables Four Wave

Device	[40]	[28]	[12]	[21]⋆	[22]	[6]
Year	1988-90	2008-09	2013	2014	2014-17	2018
Degenerate Gain (dB)*	-	16	~ 10	~ 20	6 [7]	9
GBP (MHz)*	-	11	~ 15	100	60	~ 85
1db Compression (dBm)†	-	-111	-113	-90	-103	-
$\omega_0/2\pi$ (GHz)	19.16	7.004	5.64	7.8 (7.9)	5.97	7.003
Quality Factor (Q_t)	-	620	312	-	70	65
Squeezing (dB)	3.28§	10§	4.9 ± 0.2§	≥ 12	≥ 1.2 [7]	≥ 3.84
Noise Temp. (photons)	0.146	0.23	0.16	-	-	≤ 0.046

*   Measurements reported at the operating point of maximum squeezing.

†   The 1dB compression point is referred to the output of each JPA. It is commonly reported in the literature as the input saturation power for ~ 20 dB of gain, however, we opt for the standard microwave engineering definition instead.

⋆   This device is not a DPA in the sense that it has a different Hamiltonian from Equation 2.19. Two adjacent cavities are coupled, and their modes entangled to produce squeezing.

§   Squeezing measurements are inferred at the output of the squeezer as opposed to a direct observation of noise reduction at the output of the detection chain. In the latter case, a lower bound on squeezing is measured.

Table 2.1:   Performance characteristics of various notable JPAs.

Mixing (4WM) to occur, while the latter gives rise to a 3WM process. In either case, the rotating frame Hamiltonians for both pumping schemes are approximately that of the ideal DPA (Equation 2.19) [5] and therefore the flux or current pumped JPA are capable of phase sensitive amplification and squeezing.

I only provide a brief overview of the operation of a JPA here. The complete theoretical details of this amplifier are beyond the scope of this thesis, but more detail regarding the theory of Josephson junctions and SQUIDs may be found in [8, 33] and I recommend Boutin *et al.* [5] for the theory of JPAs.

Squeezing at microwave frequencies was first demonstrated by Movshovich *et al.* in 1990 [24] using the JPA developed by Yurke *et al.* [40]. A squeezing level on the order of 3 dB was observed in a 19 GHz microwave resonator containing a single SQUID. Since

then, there has been a resurgence of interest in JPAs as a probe for weak microwave signals in cryogenic cQED experiments [14, 7, 13] and improvements in SQUID manufacturing and the use of SQUID arrays has produced improved amplifiers that attain higher levels of squeezing. Table 2.1 presents a summary of some notable JPAs and their key performance characteristics. We introduce some additional metrics for amplifier performance:

- *Gain Bandwidth Product (GBP)*: Parametric amplifiers have gain that may be tuned with the strength and frequency of the pump. However, the product of the gain and the bandwidth of the amplifier frequency response (the GBP) is approximately constant [30]. For different amplifiers set to the same gain, a higher GBP corresponds to a wider bandwidth, making the amplifier more versatile.

- *The 1dB Compression Point*: Parametric amplifiers saturate if the input power is sufficiently high. The 1 dB compression point is usually defined as the output power at which the gain of the amplifier drops by 1 dB, beyond which the amplifier no longer has a linear response [30]. Referred to the input, the 1dB compression point sets the upper limit for the usable input power.

- *Noise Temperature*: In practice, parametric amplifiers do not reach the true quantum limit according to Caves' fundamental theorems for linear amplifiers, largely due to non-negligible losses from the cavity ($\gamma > 0$ or $Q_i < \infty$). The noise temperature, reported in photons and referred to the amplifier input, is a measurement of the fluctuations of the noise operators introduced in Equations 2.5 and 2.6: $\langle \Delta \mathcal{F}_I^2 \rangle / G_I + \langle \Delta \mathcal{F}_Q^2 \rangle / G_Q$, and characterises the excess noise contributed by the amplifier.

Each of the JPAs presented in Table 2.1 represent the state of the art with respect to microwave amplifier noise performance. Some have been proven to contribute less than 1/2 a photon referred to the input in phase sensitive mode, close to the quantum limit defined in Equation 2.13. Although the input referred noise from the amplifiers of Eichler *et al.* and Zhou *et al.* was not measured [21, 22], the observation of vacuum squeezing using these devices implies comparable noise performance.

JPAs suffer from limited dynamic range quantified by their low 1dB compression power. For example, Zhong *et al.* report that their compression point of -113 dBm
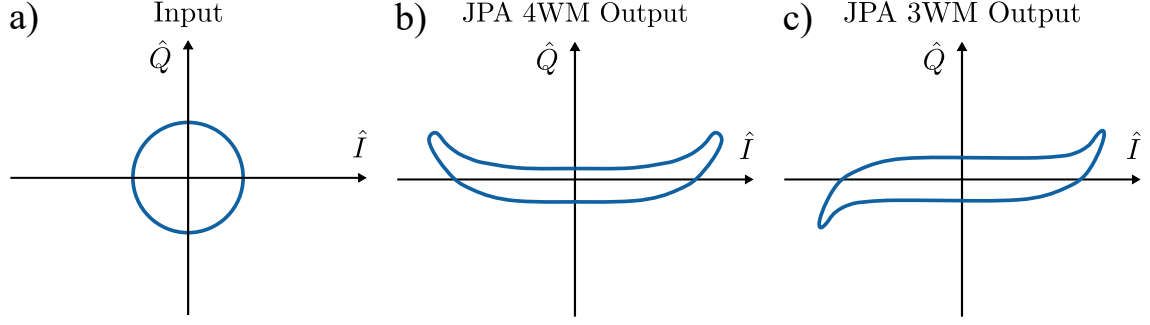
Figure 2.8: (a) The input phase space, with contour of constant magnitude depicted (blue circle). (b) Banana-type distortion of the input phase space, as observed in 4WM JPAs (e.g. [6]). (c) S-type distortion of the input phase space, as observed in 3WM JPAs (e.g. [7]).

corresponds to approximately 10 photons at the input of their device. However, the conversion from compression power to photons depends on the cavity frequency and coupling rate and will differ between devices. A compression power of -73 dBm (-93 dBm at the input) is the highest observed in any parametric amplifier based on SQUIDs [42], however, this amplifier is not a JPA/DPA and has not yet been demonstrated as a phase sensitive amplifier capable of vacuum squeezing.

From the family of devices that use the non-linear cavity model depicted in Figure 2.7, Castellanos-Beltran *et al.* hold the record for 10 dB of vacuum squeezing [28]. Eichler *et al.* deviate from this simple design by capacitively coupling two non-linear cavities of distinct resonant frequency [21]. By entangling the pair of cavity modes, they attain 12 dB of squeezing, the current state-of-the-art in microwave squeezing. Note that this device is not a DPA since its Hamiltonian differs from Equation 2.19, but as is the case with other JPAs, the use of SQUIDs will impose an upper limit on squeezing.

A recent theoretical investigation of JPAs has uncovered differences between the JPA Hamiltonian for various pumping schemes, and the Hamiltonian of the ideal DPA (Equation 2.19), which arise from the SQUID non-linearity (Equation 2.90) and become significant in the high gain limit(> 10 dB) [5]. Boutin *et al.* show that these differences, which we will refer to as Hamiltonian non-idealities, are the dominant mechanism by which squeezing is suppressed in JPAs at high gains and that minimising/eliminating these non-idealities is the path towards attaining even greater levels of squeezing [5].

Hamiltonian non-idealities, manifest themselves as a distortion of the phase space (IQ plane) as has been observed by experimentally imaging the IQ plane [6, 7], and through the measurement of statistical moments and cumulants of the noise distribution at the output of the amplifier [5]. In a 4WM JPA, this distortion is 'banana' shaped (Figure 2.8b) [6], while in a 3WM JPA the distortion appears 'S'-shaped (Figure 2.8c) [7]. The 'wings' of the distortion mix $\hat{I}$ and $\hat{Q}$ at the most amplified point, artificially increasing the output fluctuations along $\hat{Q}$ and consequently decreasing the measured squeezing. The amplified/squeezed vacuum state for the ideal DPA has a Gaussian quasi-probability distribution [43]. Phase space distortion reduces the 'Gaussianity' of the output state, and may be quantified through the statistical moments of the output field. A fundamental component of this work is the experimental characterisation of the amplifier output phase space and the statistical properties of the output noise in order to quantify the significance of Hamiltonian non-idealities in the KIPA, which we discuss in greater detail in a later chapter (Sections 5.2 and 5.6).

2.8 Kinetic Inductance

Kinetic inductance is a phenomenon of high-conductivity metals associated with the inertia of charge-carrying particles. In terms of the Drude conductivity model, kinetic inductance becomes significant in materials where the mean time between collisions τ is greater than the period of the alternating current flowing through the material. This condition is often met in superconducting films operated at low temperatures, including the NbTiN film used to define the KIPA circuit. During one period of the alternating signal, the inertia of the Cooper pairs prevents them from reversing direction instantaneously with the electric field, thus delaying the current with respect to the voltage as is similarly achieved by an inductance. The kinetic inductance L_k of a superconducting material is defined by equating the kinetic energy of the Cooper pairs with an equivalent inductive energy $1/2L_kI^2$. However, unlike a typical inductor, the kinetic inductance of superconducting films non-linearly depends on the current flowing through the film. In this section we derive an expression for the kinetic inductance following the approach of Anlage *et al.* [44], using Ginzburg and Landau's theory of superconductors.

As we considered in the distributed resonator, we model the superconducting trans-

mission line as a string of infinitesimally small lumped element inductors and capacitors. The voltage difference across one of these inductors V is related to the current flowing through it I by:

$$V = \Delta x L' \frac{\partial I}{\partial t} \tag{2.92}$$

$$= \Delta x (L'_N + L'_k) \frac{\partial I}{\partial t} \tag{2.93}$$

where Δx is the length of the lumped element inductor and L' is the inductance per unit length of the superconductor. The inductance L' may be decomposed into a sum of two contributions: L'_k the kinetic inductance, and L'_N the inductance associated with the conversion of Cooper pairs to normal electrons [45]. In this derivation we neglect any geometric inductance from the superconducting film. In the "dirty limit", the normal electron ohmic resistance is high and the time between collisions τ is short, allowing us to neglect the inductance L'_N [45]. In terms of the electric field $E = V/\Delta x$, we find:

$$E = L'_k \frac{\partial I}{\partial t} \tag{2.94}$$

The London acceleration equation for a thin film of superconducting wire states [46]:

$$\frac{\partial J}{\partial t} = \frac{n_s (2e)^2}{2m_e} E \tag{2.95}$$

where n_s is the density of Cooper pairs, which each have a mass $2m_e$ and charge $2e$. The current density $J = -2ev_s n_s$ where v_s is the super-current velocity. In the steady state, the density of Cooper pairs n_s is constant, allowing us to re-write the first London equation as the acceleration equation:

$$E = -\frac{m_e}{e} \frac{\partial v_s}{\partial t} \tag{2.96}$$

Combined with Equation 2.94 we find [44]:

$$L'_k = -\frac{m_e}{e} \left(\frac{\partial I}{\partial t} \right)^{-1} \frac{\partial v_s}{\partial t} \tag{2.97}$$

$$= -\frac{m_e}{e} \frac{\partial v_s}{\partial I} \tag{2.98}$$

We now assume operation of the film near its critical temperature T_c so that we can draw upon Ginzburg Landau theory. In the case of the thin film or wire, Ginzburg Landau

45

theory provides an analytical solution for the super-current through the cross-sectional area A [47]:

$$I = -e|\psi|^2 v_s A \tag{2.99}$$

The factor ψ is the so-called complex order parameter introduced by Ginzburg and Landau, and may be understood as a psuedo-wavefunction whereby $|\psi(x)|^2$ measures the local density of Cooper pairs at position x. Superconductors are well established as non-linear materials [48] where the non-linearity in the thin film or wire is explained in Ginzburg Landau theory by a dependence of local Cooper pair density $|\psi|^2$ on the super-current velocity v_s, according to [45, 47]:

$$\frac{|\psi|^2}{|\psi_\infty|^2} = 1 - \frac{v_s^2}{3v_m^2} \tag{2.100}$$

where v_m is the velocity corresponding to the critical (maximum) super-current I_c, and $|\psi_\infty|^2$ is the super-electron density at an infinitely far away point where local magnetic fields have decayed to zero [47]. The relative Cooper pair density increases with the velocity v_s up to v_m, beyond which depairing of electrons becomes thermodynamically favorable reducing the Cooper pair density to zero as the critical current is exceeded [44]. Substituting Equation 2.100 into our expression for current, we obtain:

$$I = -eA|\psi_\infty|^2\left(v_s - \frac{v_s^3}{3v_m^2}\right) \tag{2.101}$$

with derivative:

$$\frac{\partial I}{\partial v_s} = -eA|\psi_\infty|^2\left(1 - \frac{v_s^2}{v_m^2}\right) \tag{2.102}$$

Continuing the derivation of Analge *et al.* this derivative may now be substituted into our earlier expression for the kinetic inductance (Equation 2.98) [44]:

$$L'_k = \frac{m_e}{e^2 A|\psi_\infty|^2}\left(1 - \frac{v_s^2}{v_m^2}\right)^{-1} \tag{2.103}$$

For small currents, we may approximate $v_s/v_m \approx 2I/3I_c$ and using the Taylor series expansion for $1/(1-x)$ about $x = 0$ we obtain:

$$L'_k = \frac{m_e}{e^2 A|\psi_\infty|^2}\left[1 + \frac{4}{9}\frac{I^2}{I_c^2} + \cdots\right] \tag{2.104}$$

which may be re-written as the standard non-linear current dependence for kinetic inductance [34]:

$$L_k = L_{k,0}\left[1 + \left(\frac{I}{I_2^*}\right)^2 \cdots\right] \tag{2.105}$$

where,

$$L_{k,0} = \frac{m_e}{|\psi_\infty|^2 e^2} \frac{l}{A} \tag{2.106}$$

and l is the length of the film or wire. The kinetic inductance of the film at zero current is given by $L_{k,0}$, while I_2^* sets the strength of the quadratic non-linearity. Often we write the quotient l/A as $n_\square/t$ where t is the thickness of the film and $n_\square$ is the so-called 'number of squares' parameter corresponding to the number of $w \times w$ squares that fill in the area of the resonator.

While a number of assumptions have been made in this derivation (e.g. operation in the dirty limit and at a temperature close to T_c), the kinetic inductance current dependence on I^2 and I^4 has been shown to work well in practice [49, 50], including by this work. Equation 2.104 predicts that $I_2^* = 3/2\,I_c$, which we test experimentally in Section 4.3.

In the KIPA, the kinetic inductance of the superconducting film is the dominant source of inductance in our microwave resonator. A strong pump current modulates the inductance according to Equation 2.105 and consequently the resonant frequency of the cavity, giving rise to parametric mixing processes. In the following chapters we shall demonstrate how the non-linear current dependence of kinetic inductance may be exploited to realise a degenerate parametric amplifier capable of squeezing.

2.9   The Kinetic Inductance TWPA

The non-linearity of kinetic inductance already features in a number of cryogenic amplifiers [51, 18, 52, 20]. In contrast to the DPA which benefits from a cavity, kinetic inductance is used to generate multi-wave mixing as signal and pump microwaves propagate along a transmission line in a so-called Travelling Wave Parametric Amplifier (TWPA). Because there is no cavity involved, the TWPA is a broadband device and has been demonstrated to produce $10 - 20$ dB of gain over a multi GHz bandwidth [52, 20]. A CPW transmission line designed to have high kinetic inductance is sufficient to realise parametric amplification. However, the quadratic kinetic inductance characteristic (Equation 2.105) has been found to generate pump harmonics [51] and a number of other mixing processes that compete with the intended 3WM or 4WM [18]. Pump harmonic

generation depletes the pump while unintended mixing processes increase the noise contributed by the amplifier [20]. As such, dispersion engineering is used to attenuate pump harmonics [51] and constrain the set of frequencies able to satisfy the phase matching condition [20].

The TWPA has not yet been demonstrated to squeeze the vacuum, but has already demonstrated the potential of kinetic inductance as a non-linear medium. Output referred 1 dB compression points have been reported to be as high as -34 dBm [51], four orders of magnitude higher than observed in the best SQUID-based amplifier [42]. Recently, the input referred noise power of a kinetic inductance TWPA fabricated from NbTiN has been measured to be 0.77 ± 0.4 photons [20]. Kinetic inductance TWPAs are readily approaching the quantum limit and superconducting materials including NbTiN have robust power handling capabilities that do not appear at present an obstacle to quantum limited amplification.

Chapter 3

The Kinetic Inductance Parametric Amplifier

Across the remaining chapters in this thesis, we experimentally characterise a new type of phase-sensitive microwave parametric amplifier, that we call the Kinetic Inductance Parameteric Amplifier, or KIPA for short. We begin this chapter with a high level description of how the device works, followed by a discussion of the microwave circuit design process and parameters chosen in the case of the KIPA. We then go on to explain the manufacturing process for this device and detail its packaging. To conclude this chapter, we derive the Hamiltonian that describes the KIPA and draw connections with the ideal DPA.

It should be noted that the design, fabrication and packaging of the KIPA were all developed by another student; Mykhailo Savytskyi, and should not be considered as original work here. In addition, Sections 3.1.1, 3.1.2, 3.2 and 3.3 have been reproduced with permission. Although the work is not original, it is included here to provide the complete story of the KIPA.

The KIPA Hamiltonian deriviation (Section 3.4) is original work, and was completed in collaboration with Dr Arne Grimmsmo (University of Sydney).

3.1 Device Design and Operation

The Kinetic inductance Parametric Amplifier, depicted in Figure 3.1, is a geometrically defined microwave device, realised from a single layer of NbTiN on Silicon. The
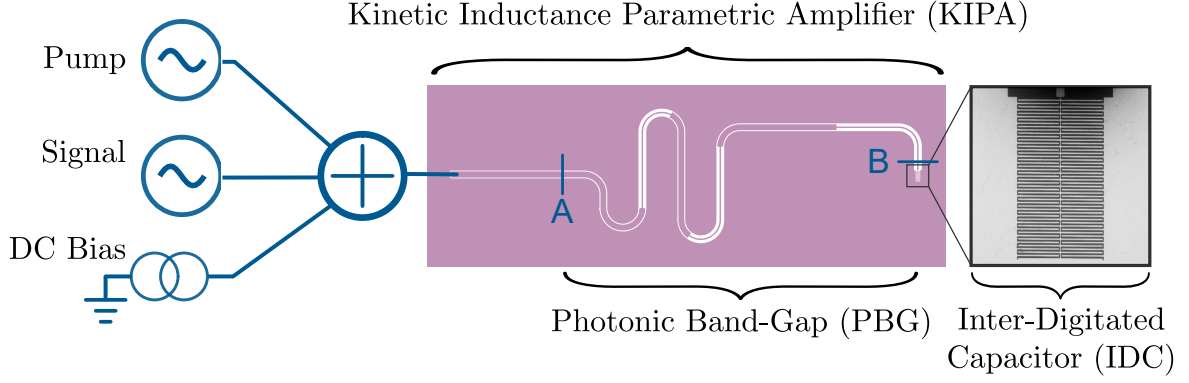
Figure 3.1: The Kinetic Inductance Parametric Amplifier (KIPA) with simplified schematic showing device operation, and SEM image of the KIPA cavity. A pump, signal and DC bias are combined and fed into the single port of the KIPA. Microwaves propagate through the Photonic Band-Gap (PBG) filter before reaching the cavity formed by an Inter-Digitated Capacitor (IDC) structure. The IDC is shorted to ground at one end, forming a $\lambda/4$ resonant cavity. The ports A and B correspond to the input and output ports of the PBG structure, and coincide with the PBG ports depicted in Figure 3.3.

device contains no Josephson junctions (making it robust to electrostatic discharge) and is produced with a single-step lithography process. The nonlinearity responsible for parametric amplification in this device originates from a kinetic inductance (see Section 2.8) intrinsic to the NbTiN film. Recall that the kinetic inductance depends non-linearly on the current flowing through the film according to [34]:

$$L_k \approx L_{k,0} \left[1 + \left(\frac{I}{I_2^*} \right)^2 \right] \tag{3.1}$$

This form of nonlinear inductance is analogous to an optical Kerr media. When a current passing through the film $I = I_{\mu w}$ consists of two different microwave tones, i.e. a signal tone and a much stronger 'pump' tone, the nonlinearity gives rise to four wave mixing (4WM), where energy transfer from the pump to the signal can effect parametric amplification [51, 52]. Introducing a DC current bias on top of the microwave tones $I = I_{\text{DC}} + I_{\mu w}$ lowers the order of the nonlinearity:

$$L_k = L_{k,0} \left[1 + \left(\frac{I_{DC}}{I_2^*} \right)^2 + 2 \frac{I_{DC} I_{\mu w}}{(I_2^*)^2} + \left(\frac{I_{\mu w}}{I_2^*} \right)^2 \right] \tag{3.2}$$

In addition to the Kerr component ($\propto I_{\mu w}^2$), a new term linear in $I_{\mu w}$ appears which can facilitate a three wave mixing (3WM) process, as has been demonstrated recently in

traveling wave devices [18, 20]. However, at high pump powers (where $I_{\mu w} \gtrsim 2I_{DC}$) the competition between 4WM and 3WM processes is known to degrade the parametric gain [53] and limit the ultimate device performance.

We exploit 3WM in a DC-current-biased resonator to produce a degenerate parametric amplifier. Critically, the resonant nature of our KIPA strongly suppresses 4WM and higher-order processes, permitting extremely high levels of pure 3WM gain. The device (see Figure 3.1) is fabricated from a 9.5 nm thick film of NbTiN on Silicon, benefiting from the high magnetic field resilience (up to $B_\perp \approx 350$ mT) and high critical temperature ($T_c \approx 10.5$ K) that are characteristic of this superconductor [54, 55]. NbTiN on Silicon can exhibit extremely low losses with internal quality factors Q_i greater than 10^6 [36], which prove crucial to the generation of highly squeezed states.

The KIPA is defined geometrically by a coplanar waveguide (CPW) quarter-wavelength resonator coupled to a single port via a microwave Bragg mirror that produces a Photonic Band-Gap (PBG) [56]. The Bragg mirror, or PBG, can equivalently be viewed as a stepped-impedance band-stop filter. The PBG (which has a frequency response depicted in Figure 3.3b) mimics the role of a capacitive coupler commonly found in JPAs [28, 21, 22], but importantly does not break the inner track of the CPW, allowing a DC current to pass through the cavity of our device. The resonator is realised using a segment of CPW featuring an interdigitated capacitor (IDC) (see Section 3.1.1) terminated in a short, and is designed to produce a resonance at the centre of the band-stop region $\omega_0/2\pi \approx 7.2$ GHz. The KIPA is designed to operate in the highly over-coupled regime, where the coupling rate to the port far exceeds the internal rate of loss ($Q_c \ll Q_i$).

3.1.1 The Resonator

For the purposes of producing parametric amplification, it is desirable to maximise the nonlinearity of the film in order to efficiently convert pump photons to signal photons, and thus reduce the required pump power in the device. That is, the objective is to minimise I_2^*, which scales with the critical current I_c. To maximise the kinetic inductance we must ensure that it dominates over the geometric inductance present in the resonator. The fraction of kinetic inductance in the resonant section of the CPW is determined by several parameters (see Section 2.8) and can enhanced by reducing the thickness of the superconducting film, which results in a higher room-temperature sheet resistance R_s and
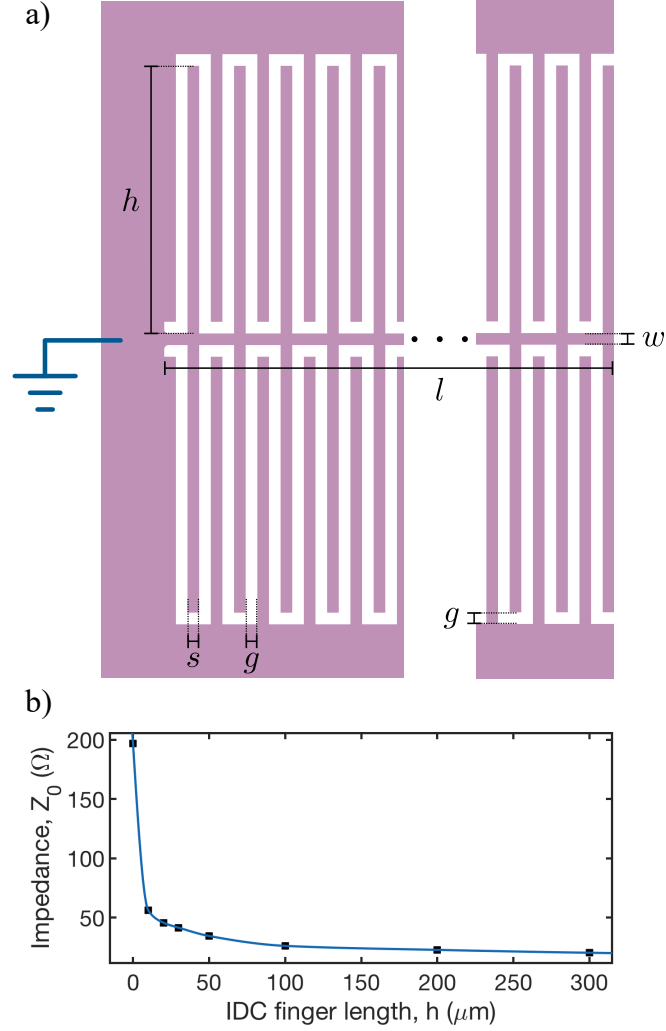
Figure 3.2: (a) The $\lambda/4$ transmission line resonator of the KIPA, drawn to scale. The resonator has length l with interdigitated capacitor fingers that provide additional capacitance to ground. The critical dimensions are labelled: the centre line width w, the gap width g, the finger width s, and the finger height h. (b) Characteristic impedance of a section of IDC as a function of the finger height h. Results are obtained from Sonnet simulations for a centre line width of $w = 2\ \mu$m.

a larger per-square value of the kinetic inductance. In addition, we may reduce the width of the central conductor w (see Equation 2.106) to raise the effective number of squares in the resonator wire and hence the total kinetic inductance. Both of these changes also result in a smaller critical current I_c. A film thickness of 9.5 nm, a centre conductor width of $w = 2$ μm, and a gap width of $g = 2$ μm were selected for the KIPA. Simulations of the complete structure in Sonnet predict a sizeable kinetic inductance of $L_{k,0} = 3.72$ nH.

Whilst the strong nonlinearity is desirable in realising a DPA, the higher inductance of the transmission line leads to a large characteristic impedance, which has several detrimental effects. A smaller resonator impedance reduces the power requirements as it provides a larger pump current for a given power. Excessive pump powers may lead to sample heating, which would prove an obstacle to quantum limited amplification. To compensate for the high kinetic inductance and reduce the impedance, we introduce an Inter-Digitated Capacitor (IDC) to the resonant CPW section. The IDC is a microwave planar capacitor that consists of a dense set of interlocking fingers between the central conductor and ground plane, as shown in Figure 3.2a. This structure boosts the capacitance per unit length and therefore lowers the characteristic impedance to $Z_0 = \sqrt{L/C}$, where L and C are the inductance and capacitance per unit length, respectively. The enhanced L and C in the resonator can considerably reduce its phase velocity $v_p = 1/\sqrt{LC}$, shortening the required resonator length l.

To engineer the IDC resonator with the desired capacitance we perform an electromagnetic simulation using Sonnet. Figure 3.2b depicts the dependence of the IDC CPW characteristic impedance Z_0 on the capacitor finger length h, extracted from Sonnet simulations for a $w = 2$ μm wide central line. A finger height of $h \approx 45$ μm and finger width of $s = 2$ μm was selected for the KIPA, giving a characteristic impedance of $Z_0 \approx 45\Omega$.

3.1.2 The Photonic Band-Gap Coupling Circuit

The photonic band-gap is formed by a periodic structure of alternating sections of transmission line of 'low' and 'high' impedance (see Figure 3.3a). The resulting circuit model is equivalent to an LC ladder filter [30]. Reflections occur at each point of abrupt change in impedance, resulting in constructive or destructive interference with the propagating signal dependent on its frequency. Consequently, the PBG has a band-stop filter response, which blocks the propagation of photons in the band-stop region, hence the
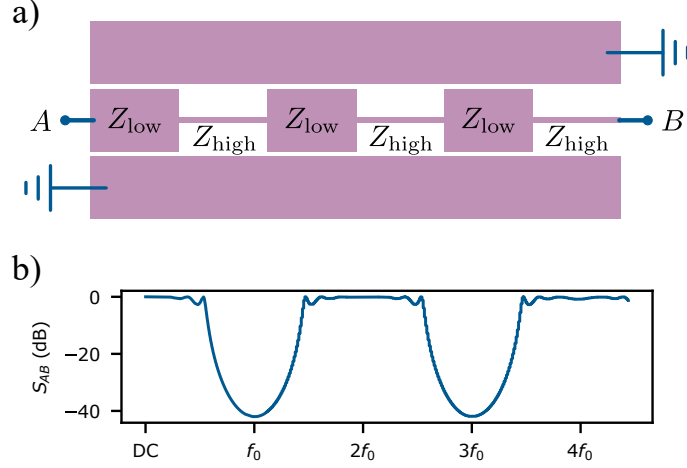
Figure 3.3: (a) Geometry of the linear photonic band-gap filter, featuring 6 sections of alternating impedance: Z_{low} and Z_{high}, with ports A and B. (b) Simulation of the transmission scattering parameter S_{AB} as obtained using the $ABCD$ matrix approach. The band-stop region is centred about the resonant frequency of the IDC: $f_0 = \omega_0/2\pi$. DC current may flow through the PBG, and the PBG is designed such that the 3WM pump at frequency $f_p \approx 2f_0$ is minimally attenuated.

name "photonic band-gap". Further, we adopt this filter geometry for the coupling circuit because the centre conductor remains unbroken throughout, allowing us to pass a DC current through the $\lambda/4$ IDC connected to one end of the PBG.

The stepped-impedance filter can readily be designed using the $ABCD$ matrix approach [30]. For a section of transmission line with length l and characteristic impedance Z_0, the $ABCD$ matrix is written in the following form:

$$\begin{pmatrix} A & B \\ C & D \end{pmatrix} = \begin{pmatrix} \cos(\beta l) & iZ_0 \sin(\beta l) \\ (i/Z_0)\sin(\beta l) & \cos(\beta l) \end{pmatrix} \tag{3.3}$$

where $\beta = \omega/v_p$ is the phase constant. We find the total $ABCD$ matrix for the complete PBG structure by taking the product of the matrices for each individual CPW section in the order that they appear in the pattern. The $ABCD$ matrix that results from the product can be conveniently converted to the conventional scattering matrix S:

$$\begin{pmatrix} S_{11} & S_{12} \\ S_{21} & S_{22} \end{pmatrix} = \begin{pmatrix} \frac{A+B/Z_0-CZ_0-D}{A+B/Z_0+CZ_0+D} & \frac{2(AD-BC)}{A+B/Z_0+CZ_0+D} \\ \frac{2}{A+B/Z_0+CZ_0+D} & \frac{-A+B/Z_0-CZ_0+D}{A+B/Z_0+CZ_0+D} \end{pmatrix} \tag{3.4}$$

Adopting the $ABCD$ matrix approach, MATLAB is used to simulate the PBG trans-
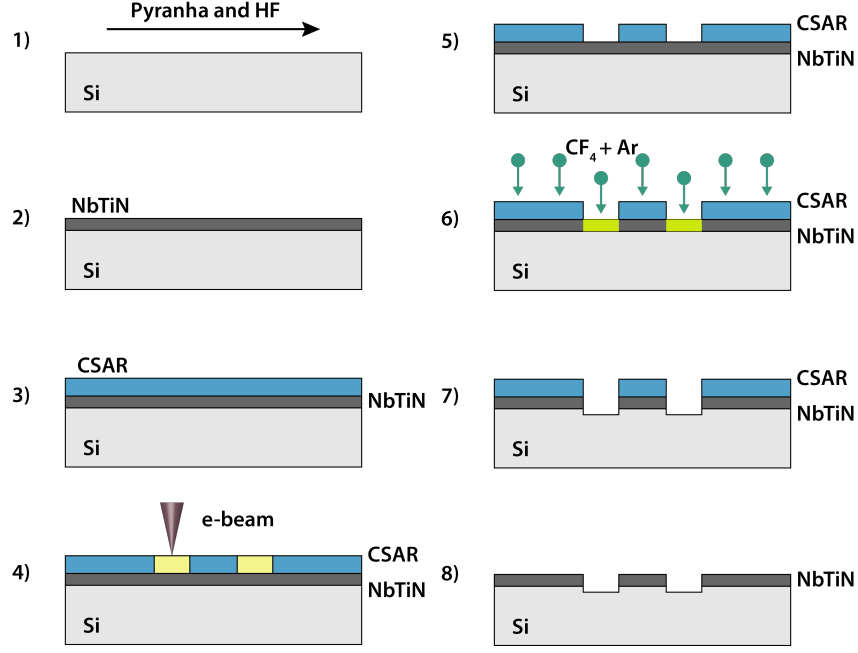
Figure 3.4: The KIPA fabrication procedure. See main text for details.

mission response S_{21} in order to determine the band-stop parameters of the PBG struc-
ture. The parameters for each CPW segment used in the calculation (i.e. the impedance
Z_0 and effective dielectric constant ϵ_{eff}) are obtained from Sonnet simulations. The low
and high impedance CPW sections have lengths $l_{\text{low}} = 3.4$ mm and $l_{\text{high}} = 3.455$ mm,
with corresponding impedances $Z_{\text{low}} = 52\ \Omega$ and $Z_{\text{high}} = 122\ \Omega$. These values produce a
band-stop region that is approximately centred about the resonant frequency of the KIPA
$\omega_0/2\pi \approx 7$ GHz, with minimal attenuation around the 3WM pump frequency $\omega_p \approx 2\omega_0$
(see Figure 3.3). The number of segments increases the depth of the band-stop region
and consequently modifies the coupling quality factor of the resonator connected to one
end of the PBG. As the KIPA is to operate in the over coupled regime, the KIPA was
designed to use 6 sections of alternating impedance (3 low impedance, 3 high impedance)
giving an approximate $Q_c \sim 100$, as obtained from Sonnet simulations.

3.2   Device Fabrication

The KIPA is fabricated from a thin NbTiN film measuring 9.5 nm in thickness and
is deposited on top of a high resistivity ($> 5\,\mathrm{k\Omega cm}$) natural silicon FZ sample. Electron

Beam Lithography (EBL) is used to pattern a resist mask onto the silicon chip. EBL was chosen for the fabrication of the KIPA as yield was expected to be high and few devices were needed, and the pattern is defined in software, facilitating rapid design iteration.

The fabrication steps for the KIPA are as follows, and are diagrammed accordingly in Figure 3.4:

1) **Clean**: The silicon sample is first cleaned in a piranha solution (a 3:1 mixture of sulfuric acid H_2SO_4 and 30% hydrogen peroxide H_2O_2) for 10 minutes on a hotplate set to 115°C in order to remove any organic contaminates. Following this the sample is rinsed in deionized (DI) water for 10 minutes. Next a 15-second dip in a hydrofluoric (HF) acid bath (10:1 mixture, with 10 parts water to 1 part 49% HF) is performed to strip the native oxide, followed by 5 minute a DI rinse.

2) **Metal Deposition**: A high quality NbTiN film is deposited on the silicon by magnetron sputtering a NbTiN target in a N_2 gas atmosphere. The sputtering is a commercial service performed by the company "Star Cryo".

3) **Resist**: We spin the positive electron-beam resist AR-P 6200 from "Allresist", referred to as CSAR 62 on top of NbTiN film at a speed 4000 RPM for 60 seconds to achieve a 200 nm thick resist layer. We bake the sample at 150°C for 3 minutes to remove solvents and harden the resist.

4) **Exposure**: Next we use a Raith-150 TWO EBL system to expose the resonator pattern on the chip at a beam acceleration of 20 kV and an aperture of $60\,\mu$m.

5) **Develop**: We develop the exposed chip in n-amyl acetate for 60 seconds, followed by a 30 second rinse in isopropanol (IPA). A short (1 minute) and low-power (50 W) oxygen plasma ash is then performed to remove and residual CSAR in the exposed and developed regions.

6) **Etch**: We remove the NbTiN regions exposed by the above steps with a Reactive Ion Etch (RIE), using an in-house built hollow cathode tool. The etch is performed with a CF_4/Ar ion plasma and removes the NbTiN at a rate of 4.5 nm/min.

7) **Post-Etch**: The KIPA is etched for 9 minutes, resulting in some etching of the Silicon. The 200 nm of CSAR is sufficient thick to survive the 9.5 nm etch of the NbTiN.

8) **Final Clean**: After the RIE we strip off any residual CSAR using the AR 600-71 remover from "Allresist". The sample is placed in the remover and left in an ultrasonic bath for 10 minutes to help remove any resist that remains on the NbTiN, followed by a 2 minute rinse in DI water.

All fabrication processes were carried out in the ANFF-NSW clean-room facilities, which are graded ISO 5/Class 100 (EBL) and ISO 7/Class 10000 (RIE).

3.3 Device Packaging

After fabrication of the KIPA, the silicon chip is secured with a small amount of wax to a PCB that was specifically designed for this chip. The PCB is made on a Rogers RO3006 0.635 mm thick laminate covered with 1 oz of copper on both sides with an immersion silver finish. This board contains of a single 50 Ω CPW trace connected to the external measurement line at one end via a surface-mount mini-SMP (SMPM) microwave connector. The other end of the PCB is wire bonded to the input port of the superconducting resonator. The bond wires are 50 μm in diameter and made from aluminum. The transmission line on the PCB is surrounded by an array of vias connecting top and bottom ground planes in order to suppress unwanted parasitic modes. The circuit board also has a milled region without any metalisation to accommodate the silicon chip. We bond across the first few cells in the resonator PBG structure in order to connect the ground planes. This is critical for suppressing parasitic CPW modes and unintended ground plane resonances in the device [57], particularly given that our PCB does not enclose the chip.

The PBG provides a means to decouple the resonator from the port. Much like an optical Bragg reflector, the PBG supports a fraction of the mode field inside it. As the ground plane separation is relatively large in this part of the device, radiation losses can't be neglected. To suppress radiation losses, we place the chip inside a 3D rectangular copper cavity with a fundamental frequency slightly higher than the superconducting resonator. The PCB allows most of the chip to protrude into the microwave cavity via a rectangular waveguide with a cutoff frequency far-exceeding that of the cavity. This helps us to maintain a high internal quality factor of the 3D cavity ($Q_i \approx 2000$), which would otherwise be destroyed by the presence of the PCB and bond wires. The copper enclosure
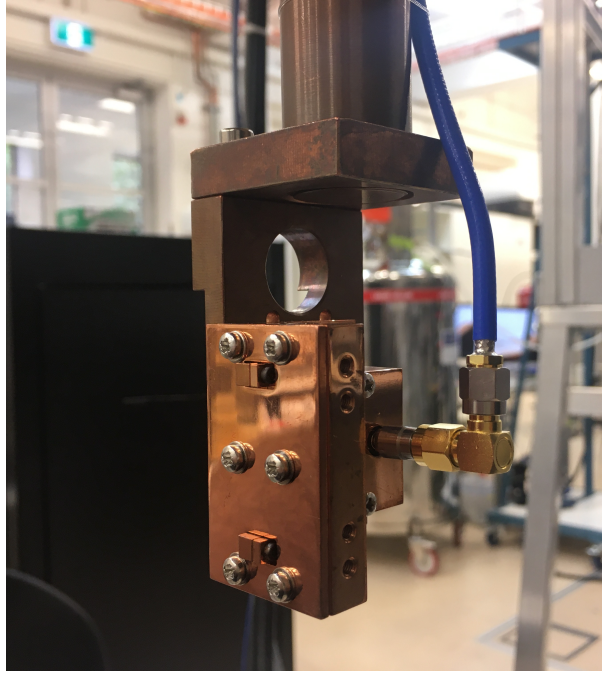
Figure 3.5: An image of the KIPA enclosure mounted to our dilution refrigerator.

is thermally anchored to the mixing plate of our dilution refrigerator, as depicted in Figure 3.5.

3.4 The KIPA Hamiltonian

3.4.1 The Cumulative Charge and Flux of the Pump & Bias

In Section 2.4 we codified the $\lambda/4$ resonator problem in terms of a cumulative flux $\Phi(x,t)$ and a cumulative charge $Q(x,t)$. Before attempting to write down the Hamiltonian for the KIPA in the presence of a pump, we begin by determining the relationship between voltage and Q, and current and Φ.

Using the fact that $q_n = C_0 V_n$, where q_n is the charge on the n-th node and V_n is the voltage on the n-th node, combined with the definition of the cumulative charge (Equation 2.46):

$$Q_n = C' \sum_{i=0}^{n} V_i \Delta x \tag{3.5}$$

In the limit of $\Delta x \to 0$ the spatial distribution of charge is:

$$Q(x) = C' \int_0^x V(u)\, du \tag{3.6}$$

By the fundamental theorem of calculus, we have:

$$\frac{\partial Q}{\partial x} = C'V(x) \tag{3.7}$$

In the presence of a DC bias current and a pump tone, we may decompose the total cumulative charge into its constituent components: $Q_{\text{tot}} = Q_{\text{DC}} + Q_{\text{AC}} + Q$ where Q is the charge associated with the cavity mode. We note here that the DC bias does not contribute a charge component. Because the NbTiN film is superconducting, the device displays zero DC resistance for all x and therefore the bias does not contribute a DC voltage. As per Equation 3.6, we have $Q_{\text{DC}} = 0$ and hence $\dot{Q}_{\text{DC}} = 0$ and $\partial Q_{\text{DC}}/\partial x = 0$.

Using Equation 3.7, the spatial and time derivatives of the total charge in the KIPA transform into:

$$\frac{\partial Q_{\text{tot}}}{\partial x} = C'(V(x) + V_{\text{AC}}) = \frac{\partial Q}{\partial x} + C'V_{\text{AC}} \tag{3.8}$$

$$\dot{Q}_{\text{tot}} = \dot{Q} + I_{\text{AC}} \tag{3.9}$$

Conversely, the momentum variable of the mode $L_T\dot{Q}$ introduces a current I_Q that perturbs the inductance:

$$I_Q = \dot{Q} \tag{3.10}$$

which we later use in our expression of the Lagrangian for the KIPA.

3.4.2 The Pump Mode

Before proceeding to evaluate the Hamiltonian, we first address the spatial distribution of the pump. As the cavity is a transmission line with a shorted end, the pump must obey the telegrapher equations with a null at $x = l$. The pump used to operate KIPA is close to twice the resonant frequency of the circuit: $\omega_p \approx 2\omega_0$. Therefore, we approximate the spatial distribution by the half wavelength mode to simplify the derivation of the Hamiltonian:

$$I_{\text{AC}}(x,t) = \cos\left(\frac{\pi}{l}(x-l)\right)I_{\text{AC}}(t) \tag{3.11}$$

$$V_{\text{AC}}(x,t) = \sin\left(\frac{\pi}{l}(x-l)\right)V_{\text{AC}}(t) \tag{3.12}$$

where the time dependencies are $I_{\text{AC}}(t) = I_p\cos(\omega_pt + \phi_p)$ and $V_{\text{AC}}(t) = V_p\sin(\omega_pt + \phi_p)$ with peak pump current I_p and voltage V_p.

3.4.3 The Lagrangian and Hamiltonian

We start our derivation with the Lagrangian for a $\lambda/4$ resonator, as we derived in Section 2.4:

$$\mathcal{L} = \frac{1}{2} \int_0^l L' \dot{Q}_{\text{tot}}^2 - \frac{1}{C'} \left(\frac{\partial Q_{\text{tot}}}{\partial x} \right)^2 dx \qquad (3.13)$$

Next, we apply a DC current I_{DC} and an AC pump with current $I_{\text{AC}}(x,t)$ and voltage $V_{\text{AC}}(x,t)$ through the device. Substituting in the quadratic expression for kinetic inductance and applying Equations 3.8 and 3.9, we obtain the Lagrangian:

$$\mathcal{L} = \frac{1}{2} \int_0^l L'_{k,0} \left[1 + \left(\frac{\dot{Q} + I_{\text{DC}} + I_{\text{AC}}}{I^*} \right)^2 \right] (\dot{Q} + I_{\text{AC}})^2 - \frac{1}{C'} \left(\frac{\partial Q}{\partial x} + C' V_{\text{AC}} \right)^2 dx \qquad (3.14)$$

where $L'_{k,0}$ is the kinetic inductance per unit length at zero current.

As previously, we apply the Legendre transformation to obtain the Hamiltonian, this time using the *SymPy* symbolic algebra package to expand $\mathcal{L}$ with respect to $\dot{Q}$:

$$H_{\text{KIPA}} = \dot{Q} \frac{\partial \mathcal{L}}{\partial \dot{Q}} - \mathcal{L} \qquad (3.15)$$

$$= H_0 + H_1 \qquad (3.16)$$

where H_0 is the Hamiltonian for the $\lambda/4$ resonator obtained in Section 2.4 but now with a biased inductance,

$$H_0 = \frac{1}{2} \int_0^l \frac{1}{C'} \left(\frac{\partial Q}{\partial x} \right)^2 + L'_{k,0} \left[1 + \left(\frac{I_{\text{DC}}}{I_2^*} \right)^2 \right] \left(\frac{\partial Q}{\partial t} \right)^2 dx \qquad (3.17)$$

and H_1 captures the nonlinear terms and the fast-oscillating linear components introduced through the kinetic inductance:

$$H_1 = \int_0^l V_{\text{AC}} \frac{\partial Q}{\partial x} + \mathcal{A}(\dot{Q})^4 + \mathcal{B}(\dot{Q})^3 + \mathcal{C}(\dot{Q})^2 dx \qquad (3.18)$$

with coefficients:

$$\mathcal{A} = \frac{3 L'_{k,0}}{2(I_2^*)^2} \qquad (3.19)$$

$$\mathcal{B} = 2 L'_{k,0} \frac{2 I_{\text{AC}} + I_{\text{DC}}}{(I_2^*)^2} \qquad (3.20)$$

$$\mathcal{C} = L'_{k,0} \frac{3 I_{\text{AC}}(I_{\text{DC}} + I_{\text{AC}})}{(I_2^*)^2} \qquad (3.21)$$

All constants terms are dropped for brevity. From Section 2.4 we have the mode expansion that diagonalises our system with respect to H_0. As the only mode used for

amplification in the KIPA is the fundamental, we truncate the expansion to the first mode:

$$Q(x) = A_0 \cos\left(\frac{\pi}{2l}(x - l)\right)\hat{Q} \tag{3.22}$$

$$\Phi(x) = \frac{A_0}{lk_0} \sin\left(\frac{\pi}{2l}(x - l)\right)\hat{\Phi} \tag{3.23}$$

The mode solution for the flux was found by inserting Equation 2.51 into the telegrapher Equation 2.48. Recall, the operators are given by:

$$\hat{Q} = i\sqrt{\frac{\hbar}{2Z_0}}(\hat{a}^\dagger - \hat{a}) \tag{3.24}$$

$$\hat{\Phi} = \sqrt{\frac{\hbar Z_0}{2}}(\hat{a}^\dagger + \hat{a}) \tag{3.25}$$

We note that now the total inductance is now given by $L_T = L_{k,0}(1 + (I_{\mathrm{DC}}/I_2^*)^2)$, the resonance frequency $\omega_0 = \pi/2\sqrt{L_T C_T}$ is shifted by the DC bias, and the characteristic impedance of the fundamental is given by $Z_0 = L_T\omega_0$. We again take advantage of the first telegrapher equation (Equation 2.48) to express the derivative of the charge in terms of the flux operator:

$$\frac{\partial Q}{\partial t} = \frac{A_0}{L_T} \cos\left(\frac{\pi}{2l}(x - l)\right)\hat{\Phi} \tag{3.26}$$

Combining everything together, we evaluate the integrals for the fundamental cavity mode and pump mode:

$$H_0 = \frac{1}{2}\left[L_T\omega_0^2\hat{Q}^2 + \frac{1}{L_T}\hat{\Phi}^2\right] \tag{3.27}$$

$$H_1 = \mathcal{A}'\hat{\Phi}^4 + \mathcal{B}'\hat{\Phi}^3 + \mathcal{C}'\hat{\Phi}^2 - \frac{4V_{\mathrm{AC}}(t)}{3\sqrt{2}}\hat{Q} \tag{3.28}$$

where,

$$\mathcal{A}' = \frac{9}{4((I_2^*)^2 + I_{\mathrm{DC}}^2)L_T^3} \tag{3.29}$$

$$\mathcal{B}' = \frac{32(6I_{\mathrm{AC}}(t) + 5I_{\mathrm{DC}})}{15\pi^2\sqrt{2}((I_2^*)^2 + I_{\mathrm{DC}}^2)L_T^2} \tag{3.30}$$

$$\mathcal{C}' = \frac{3I_{\mathrm{AC}}(t)(I_{\mathrm{AC}}(t) + I_{\mathrm{DC}})}{2((I_2^*)^2 + I_{\mathrm{DC}}^2)L_T} \tag{3.31}$$

3.4.4 The Hamiltonian in the Rotating Frame

Substituting the operator definitions for $\hat{Q}$ and $\hat{\Phi}$ from Equations 3.24 and 3.25, we rewrite the total Hamiltonian in the Fock basis:

$$H = \hbar\omega_0\hat{a}^\dagger\hat{a} + \mathcal{A}''(\hat{a}^\dagger + \hat{a})^4 + \mathcal{B}''(\hat{a}^\dagger + \hat{a})^3 + \mathcal{C}''(\hat{a}^\dagger + \hat{a})^2 - i\frac{2V_{\mathrm{AC}}(t)\sqrt{\hbar Z_0}}{3}(\hat{a}^\dagger - \hat{a}) \tag{3.32}$$

where,

$$\mathcal{A}'' = \frac{9\hbar^2\omega_0^2}{16((I_2^*)^2 + I_{\mathrm{DC}}^2)L_T} \tag{3.33}$$

$$\mathcal{B}'' = \frac{8\hbar\omega_0\sqrt{\hbar\omega_0 L_T}(6I_{\mathrm{AC}}(t) + 5I_{\mathrm{DC}})}{15\pi^2((I_2^*)^2 + I_{\mathrm{DC}}^2)L_T} \tag{3.34}$$

$$\mathcal{C}'' = \frac{3\hbar\omega_0 I_{\mathrm{AC}}(t)(I_{\mathrm{AC}}(t) + I_{\mathrm{DC}})}{4((I_2^*)^2 + I_{\mathrm{DC}}^2)} \tag{3.35}$$

Rewriting $I_{\mathrm{AC}}(t) = I_p(e^{j(\omega_p t + \varphi_p)} + e^{-j(\omega_p t + \varphi_p)})/2$ and dropping all fast rotating and constant terms, the Hamiltonian simplifies to:

$$H/\hbar = (\omega_0 + K + \delta\omega)\hat{a}^\dagger\hat{a} + \frac{\xi}{2}e^{-j\omega_p t}\hat{a}^{\dagger 2} + \frac{\xi^*}{2}e^{j\omega_p t}\hat{a}^2 + \frac{K}{2}\hat{a}^{\dagger 2}\hat{a}^2 \tag{3.36}$$

where,

$$K = \frac{27\hbar\omega_0^2}{8((I_2^*)^2 + I_{\mathrm{DC}}^2)L_T} \tag{3.37}$$

$$\xi = \frac{3\omega_0 I_{\mathrm{DC}} I_p e^{-j\varphi_p}}{4((I_2^*)^2 + I_{\mathrm{DC}}^2)} \tag{3.38}$$

$$\delta\omega = -\frac{3\omega_0 I_p^2}{8((I_2^*)^2 + I_{\mathrm{DC}}^2)} = -\frac{|\xi|}{2}\frac{I_p}{I_{\mathrm{DC}}} \tag{3.39}$$

The $\delta\omega$ term arises from the square of the pump current found in $\mathcal{C}''$, which has a non-zero average value of $I_p^2/2$ and causes an effective detuning of the cavity frequency.

In a frame rotating at half the pump frequency $\omega_p/2$, the KIPA Hamiltonian becomes:

$$H_{\mathrm{KIPA}}/\hbar = \Delta\hat{a}^\dagger\hat{a} + \frac{\xi}{2}\hat{a}^{\dagger 2} + \frac{\xi^*}{2}\hat{a}^2 + \frac{K}{2}\hat{a}^{\dagger 2}\hat{a}^2 \tag{3.40}$$

with detuning $\Delta = \omega_0 + K + \delta\omega - \omega_p/2$.

The KIPA Hamiltonian resembles the Hamiltonian of an ideal DPA with an additional Kerr shift $H_{\mathrm{Kerr}} = (K/2)\hat{a}^{\dagger 2}\hat{a}^2$:

$$H_{\mathrm{KIPA}} = H_{\mathrm{DPA}} + H_{\mathrm{Kerr}} \tag{3.41}$$

Thus, the KIPA will behave as a degenerate parametric amplifier. In later sections we show that the Kerr term, which is limited by the material parameters and resonator geometry, is negligible. Because K is independent of the pump, we find the KIPA to well approximate the ideal DPA Hamiltonian even at high signal gains ($G \approx 30$ dB).

Chapter 4

Amplifier Performance

In this chapter we characterise the KIPA as a classical amplifier. We begin with a summary of the experimental setup used to perform each of the measurements presented in this chapter. The experiments start with a characterisation of the bias current response to determine an appropriate operating point for the current bias and pump frequency. We then measure and fit the gain in non-degenerate and degenerate modes of operation. To conclude, we measure the 1 dB compression power of the device at various phase sensitive gains.

4.1 Cryogenic Setup

Figure 4.1 depicts the microwave circuit employed for the experiments detailed in this chapter. Microwave components are distributed between the different temperature stages of the fridge to supply the amplifier input signal, bias current, and pump tone without significant conduction of room temperature noise. A circulator redirects the reflected KIPA output signal to a High Electron Mobility Transistor (HEMT) amplifier situated at 4K, where the signal is amplified up to room temperature.

4.1.1 The Signal Line

Three $20\,\mathrm{dB}$ attenuators are used to thermalize the line and minimise the transmission of thermal noise above $20\,\mathrm{mK}$, and are situated at the $4\,\mathrm{K}$, $100\,\mathrm{mK}$ and $20\,\mathrm{mK}$ stages, respectively. The number of noise photons at frequency ω at the output of an attenuator
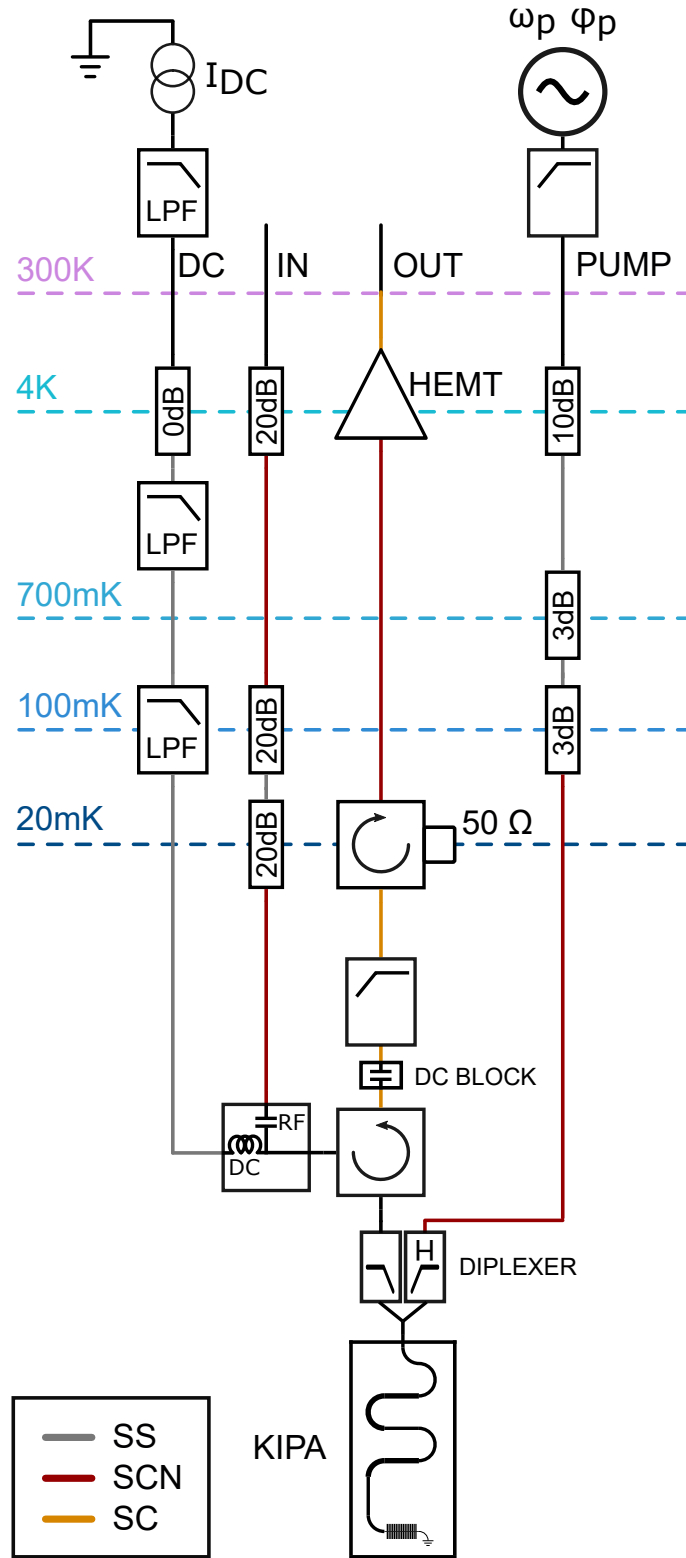
Figure 4.1: Cryogenic microwave setup for amplifier characterisation experiments. The legend defines the type of coaxial cables used throughout the setup: Stainless Steel (SS), Silver Cupro-Nickel (SCN) and Silver-plated Copper (SC).

at temperature T_{att} is given by:

$$n_{\mathrm{out}} = \lambda_{\mathrm{att}} n_{\mathrm{in}} + (1 - \lambda_{\mathrm{att}}) \frac{1}{2} \coth\left(\frac{\hbar\omega}{k_B T_{\mathrm{att}}}\right) \tag{4.1}$$

where $k_B = 1.38 \times 10^{-23}$ is the Boltzmann constant, and λ_{att} is the power transmission coefficient. The number of input noise photons is similarly given by $1/2 \coth(\hbar\omega/k_B T_{\mathrm{in}})$ where T_{in} is the temperature of the input noise. Applying Equation 4.1 for the three 20 dB attenuators at their three respective temperatures, we find good thermal isolation at 7 GHz with the addition of only 2.4×10^{-3} photons from the higher temperature stages down to 20 mK, in principle.

Before arriving at the KIPA, the signal is directed through the high frequency port of a bias-T (PE1615 Pasternack Enterprises), followed by a cryogenic circulator (CTH0408KCS Quinstar Technology Inc.), and then the low frequency port of our diplexer (DPX-1114 Marki Microwave Inc.), as illustrated in Figure 4.1. The purpose of the diplexer is to combine the pump and signal onto the same line while minimising the coupling of the reflected amplified signal back into the pump line. It is preferable to place the diplexer before the circulator to minimise insertion loss along the detection path. However, this was not possible because the ~ 14 GHz pump was out of the bandwidth of our cryogenic circulator.

4.1.2 The DC Line

A current source (GS2000 Yokogawa Electric Corp.) at room temperature supplies the DC bias current required to operate the KIPA. The bias current is directed through a series of base-band low pass filters (VLF-105+ MiniCircuits Technologies), used to minimise the conduction of room temperature noise at the pump and signal frequencies down to the base temperature stage at 20 mK. Additionally, A 0 dB attenuator is used to thermalize the DC line to the 4 K stage. The DC current is combined with the signal line using a bias-T, where it has a direct conduction path through the circulator, the diplexer and then the KIPA.

4.1.3 The Pump Line

An E8267D microwave source (Keysight Technologies Inc) supplies the pump tone for all experiments via a high-pass filter. The E8267D produces a sub-harmonic at the

detrimental frequency of $\omega_p/2$, that is 60 dB weaker than the output, resulting in room temperature signal powers as high as -56 dBm in our experiments. The high-pass filter reduces the sub-harmonic by a further 25 dB.

As with the signal line, a series of three attenuators at different temperature stages are used to thermalize the line and minimise the conduction of room temperature noise at the signal/cavity frequency ω_0. A 10 dB attenuator is used at the 4 K temperature stage, followed by two 3 dB attenuators at the 900 mK (still) and 100 mK stages, respectively. Taking into consideration the 40 dB stop-band rejection of the diplexer at $\omega_0 \sim 7$ GHz, only 2.5×10^{-3} photons at ω_0 reach the 20 mK stage.

Repeating the calculation at the pump frequency, we find that 9.42 photons reach the input port of the device. The 'noisy' pump is not anticipated to influence the operation of the device, which operates in the strong pump limit.

4.1.4   The Detection Path

A cryogenic circulator (CTH0408KCS Quinstar Technology Inc.) routes the reflected output of the KIPA through the detection chain. A DC block immediately follows to prevent the bias current from reaching the DC sensitive HEMT. A band-pass filter (BPC50403-01 Microtronics Engineering) then heavily attenuates any pump power leakage that reaches the circulator and HEMT. An isolator (Raditek RADC-4-10-Cryo-0.02-4K-S23-1WR-DMS-b) thermalize the line to 20 mK and absorb any reflections or noise originating from the HEMT. The HEMT (LNF-LNC4 Low Noise Factory), situated at 4 K, amplifies the KIPA output by approximately 40 dB and is connected directly to the output of the fridge.

4.2   Room Temperature Setup

For the bias current response experiment (Section 4.3) and the phase insensitive gain measurement (Section 4.4), the room temperature setup is simply the VNA with an additional 35 dB microwave pre-amplifier connected to the detection chain, as diagrammed in Figure 4.2.

The phase sensitive gain characterisation (Section 4.5) and 1 dB-compression point measurement (Section 4.6) require an additional microwave source (see Figure 4.2). The
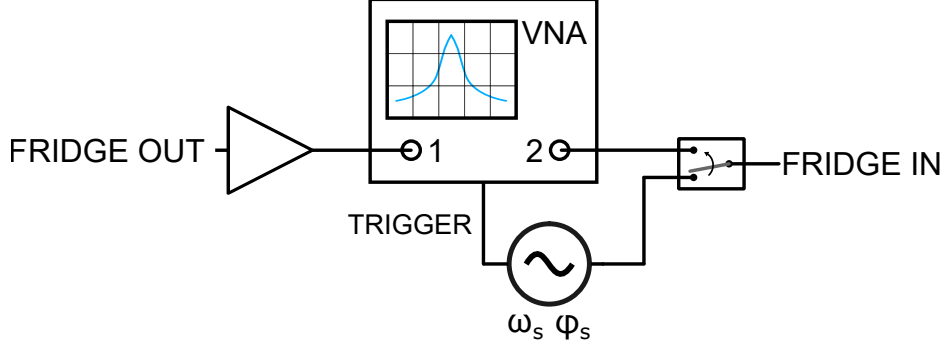
Figure 4.2: Room temperature microwave setup for amplifier characterisation. A microwave switch allows us to perform a traditional VNA style measurement, or alternatively supply the signal from a separate microwave source while using one port of the VNA as a spectrum analyser. The microwave source generates a pulse at the beginning of each phase modulation period, which is used to trigger the VNA in the phase sensitive amplification experiment.

signal port of the VNA is terminated with $50\,\Omega$ by a microwave switch and configured for a zero span measurement at frequency $\omega_p/2$. Although still configured for an S_{21} type measurement, the VNA functions as a spectrum analyser, while the separate microwave source is used to stimulate the device. The microwave source is programmed for sawtooth phase modulation at half the pump frequency $\omega_p/2$, ramping the phase from -2π to 2π on each cycle. The microwave source concurently generates a trigger pulse at the beginning of each period of the phase ramp, which is used to trigger the zero-span data acquisition on the VNA. As there is no direct path from the VNA signal port to the VNA detection port, we cannot rely on the incident power reported from the VNA. Instead, we perform consecutive measurements with the KIPA on and off, and measure the difference in microwave power (i.e. the gain).

4.3   Bias Current Response

To operate the KIPA we must first choose the two parameters: the bias current I_{DC} and the pump frequency ω_p. A non-zero bias current is needed for 3WM to occur. Therefore, we first choose a bias current and then optimise the pump frequency accordingly. We begin the experimental characterisation of the KIPA by measuring the response of

the resonator to the bias current without the pump active.

The resonant frequency of the KIPA is given by:

$$\omega_0(I) = \frac{1}{\sqrt{(L_g + L_k(0) + \Delta L_k(I))C}} \tag{4.2}$$

where L_g is the geometric inductance of the circuit, $L_k(0)$ is the kinetic inductance for zero bias current, and C the capacitance of the resonator. We define $\Delta L_k(I) = L_k(I) - L_k(0) = L_{k,0}(I^2/I_2^{*2} + \cdots)$, where $L_k(I)$ is the current dependent kinetic inductance defined in Equation 2.105. By definition $\Delta L_k(0) = 0$. Approximated to the first order, the resonant frequency changes linearly with the kinetic inductance:

$$\omega_0(I) \approx \frac{1}{\sqrt{(L_g + L_k(0))C}} - \frac{1}{2(L_g + L_k(0))\sqrt{(L_g + L_k(0))C}}\Delta L_k(I) \tag{4.3}$$

While the capacitance and the geometric inductance may be approximated from simulation, we treat them here as unknowns. It is therefore useful to consider the relative frequency shift:

$$\Delta\omega_0(I) = \omega_0(I) - \omega_0(0) \tag{4.4}$$

$$\approx -\frac{1}{2(L_g + L_k(0))\sqrt{(L_g + L_k(0))C}}\Delta L_k(I) \tag{4.5}$$

$$\approx -\frac{\omega_0(0)}{2}\frac{L_{k,0}}{L_g + L_{k,0}}\left[\left(\frac{I}{I_2^*}\right)^2 + \cdots\right] \tag{4.6}$$

$$\approx -\frac{\omega_0(0)}{2}\left[\left(\frac{I}{I_2^*}\right)^2\right] \tag{4.7}$$

where we use $L_{k,0} \gg L_g$ in the last line, as has been intentionally designed for through the resonator geometry and choice of superconductor. Without knowing L_g, $L_k(0)$ or C, Equation 4.7 provides us with a means to quantify the KIPA non-linearity constant I_2^* by observing the resonance frequency shift with an applied DC current.

4.3.1 Measurement

To measure the resonator response we perform a reflection measurement using the VNA, where one port of the VNA is used to stimulate the KIPA via the signal line, and a second port measures the reflected response routed through the detection chain via the circulator. Meanwhile, a bias current is applied through the DC port of our setup.

Because the KIPA is deliberately over-coupled ($\kappa \gg \gamma$), the magnitude response of the cavity reflection parameter (Equation 2.79) near the resonance frequency ω_0 is:

$$|\Gamma(\omega)| \approx \left| \frac{2\kappa}{\kappa + \gamma} - 1 \right| \tag{4.8}$$

$$\approx 1 \tag{4.9}$$

Due to the flat magnitude response and the orders of magnitude difference between κ and γ, an accurate fit to the reflection parameter (Equation 2.79) is not possible. However, the resonance frequency may be extracted from the phase response, where a 2π phase shift occurs centred about the resonance frequency.

Sweeping the bias current from 0 mA up to the approximate critical current $I_c = 0.9$ mA, we observe the phase response of the KIPA, as shown in Figures 4.3a and 4.4. Line delay is first removed from the phase response by subtracting a linear fit to the phase away from the resonance. Further complicating the fitting of the resonance are significant ripples that are present throughout the phase response (see Figure 4.3a) that are likely due to microwave reflections in the setup.

In order to robustly extract the resonant frequency from this data, we take the difference between traces at adjacent bias currents I_j and I_{j+1}, as illustrated in Figure 4.3b. Since the ripples are common to each measurement, taking the difference between traces leaves behind the difference in phase responses while the ripples cancel. For the ideal reflection style resonator, a peak occurs exactly half-way between the two distinct resonant frequencies. A Savitzky-Golay filter (window length: 253, polynomial order: 5) is applied to the data to reduce noise, after which the frequency at the peak is extracted. We use this value to estimate the resonant frequency at $(I_j + I_{j+1})/2$, as plotted in Figure 4.4 (white diamonds).

We measure a native resonance frequency of $\omega_0 = \omega_0(0) = 7.2898$ GHz, and over 100 MHz of frequency tunability. The error (standard deviation) on the predicted resonant frequency is measured at $\sigma = 2.16$ MHz.

We proceed to fit our quadratic expression for the relative frequency shift (Equation 4.7) to the extracted resonant frequencies and find good agreement with theory. We extract a second order non-linearity of $I_2^* = 5.102$ mA. Ginzburg Landau theory predicts $I_2^* = 3/2 I_c$ (see Section 2.8), which is not reflected in our data. However, the derivation presented in Section 2.8 assumes operation near the critical temperature. For NbTiN this
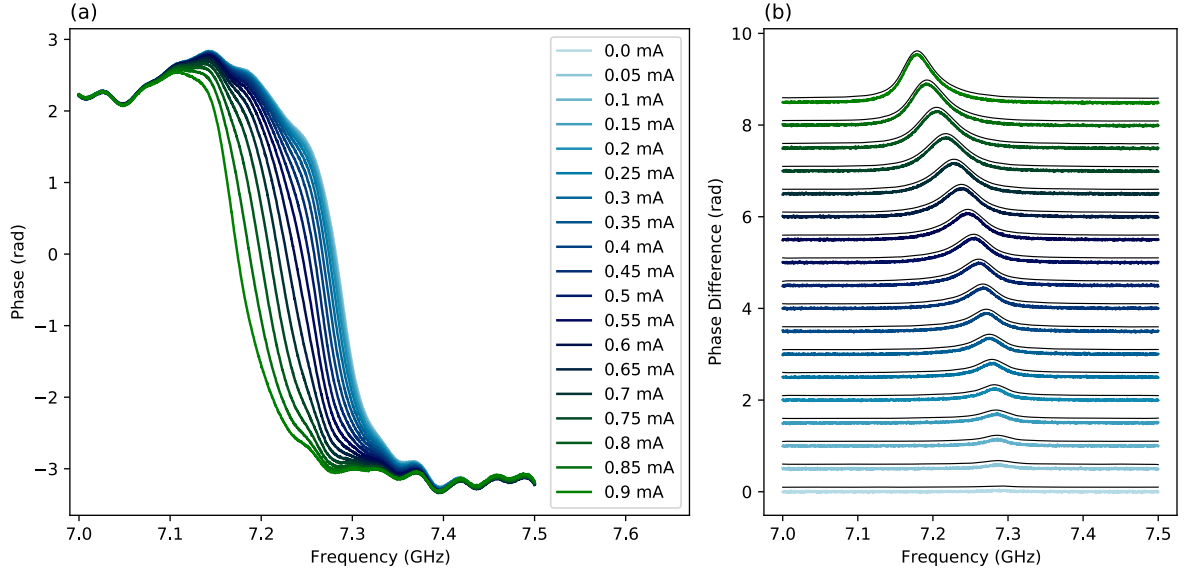
Figure 4.3: (a) The phase response at different bias currents after line delay removal. Due to the current dependence of kinetic inductance, the resonant frequency changes resulting in a frequency shift in the phase response. Note the significant ripples present throughout the frequency span of the measurement. (b) The difference in phase response at adjacent bias currents. Data is offset for illustrative purposes. The ripples cancel, leaving behind a peak at the average of the two resonant frequencies. The data is filtered (black traces) to reduce noise in the peak measurement. The filtered data is also slightly offset for visual clarity.
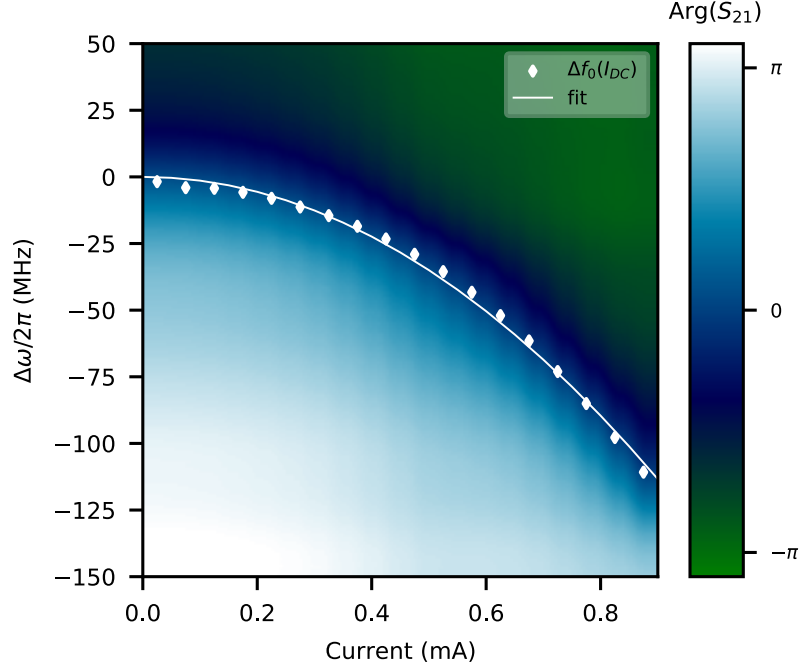
Figure 4.4: KIPA phase response as a function of bias current. The measured resonance frequency (diamonds) is fit to theory (solid line). The vertical axis is the frequency shift $\Delta\omega = \omega(I) - \omega_0(0)$.

is approximately $T_c \approx 10.5$ K [54, 55], well above the device temperature of 20 mK used in these experiments and is a likely cause for this discrepancy. In addition, the if the critical current is limited by local defects or nonidealities in the fabrication (such as edge roughness, constrictions etc.), then we would also expect a discrepancy. Despite this, the predicted quadratic approximation fits the data well.

4.3.2 Kerr Shift

A comparison of the expressions for K (Equation 3.37) and ξ (Equation 3.38) reveals why the KIPA functions as an ideal DPA: the photon energy is a minuscule fraction of the characteristic nonlinear inductive energy (i.e. $\hbar\omega_0/(L_T((I_2^*)^2 + I_{DC}^2)) \approx \hbar\omega_0/(L_T I_2^{*2}) \ll 1$) by virtue of I_2^* being large. In fact, one can show that $L_T I_2^{*2} = E_p$, where E_p is the superconducting pairing energy [34], which itself depends on the effective volume of the nonlinear inductance.

The greater the volume over which L_T is spread, the smaller the Kerr interaction. On the other hand, the 3WM strength is in some sense independent of I_2^*, since I_{DC} and I_p

can always be raised to a sizable fraction of I_2^*, with the provision that they are kept sufficiently small so that device heating does not occur.

In the worst case, setting $I_{\mathrm{DC}} = 0$ gives the highest value for the Kerr coefficient K. Using the estimated kinetic inductance of $L_{k,0} = 3.72$ nH, we find $K \leq 1.13$ Hz, a completely negligible quantity relative to all other system parameters. Compared to the coupling rate, we achieve the ratio: $K/\kappa \sim 10^{-7}$, smaller than the typical values of $K/\kappa > 10^{-4}$ seen in JPAs [5]. Because the Kerr term is so small, we approximate the Hamiltonian for the KIPA with the Hamiltonian for the ideal DPA for the remainder of this work:

$$H_{\mathrm{KIPA}} \approx H_{\mathrm{DPA}} \tag{4.10}$$

4.3.3 Choice of Bias Current

Figure 4.5 depicts the reflection response of a device similar to the KIPA, with a different resonator geometry and a coupling circuit designed to be closer to critical coupling than the KIPA. As such, the magnitude response shows a distinct dip and both the loss rate $\gamma = \omega_0/Q_i$ and coupling rate $\kappa = \omega_0/Q_c$ may be extracted. Although resonator losses are sensitive to the device geometry, we observe a current dependent loss rate in this similar device. We are unable to perform an equivalent measurement in the KIPA due to its coupling regime, however, a current dependent loss rate may be used to inform the choice of bias current. From the input output relation for the DPA (Equation 2.86), bath photons couple into the output field at a rate proportional to $\sqrt{\gamma}$. To maximise the achievable squeezing for the ideal DPA it makes sense to optimise the bias current such that γ is minmal (Q_i is large). Alternatively, squeezing might be measured as a function of bias current, and the operating bias current determined by the measured maximum. If the KIPA and this device share a similar current dependence for losses, then a small bias current is preferable.

Conversely, a large bias current minimises the required pump power to achieve the same gain since the mixing strength $|\lambda| \propto I_{\mathrm{DC}} I_p$. For the experiments detailed in this chapter, we elected to use a bias current of $I_{\mathrm{DC}} = 0.834$ mA; close to the critical current of the film but with a sufficient margin for additional microwave currents applied through the pump and signal. From the fit to the bias current response, we extract a resonant frequency of $\omega_0 = 7.1924$ GHz at this bias current. The corresponding pump power for
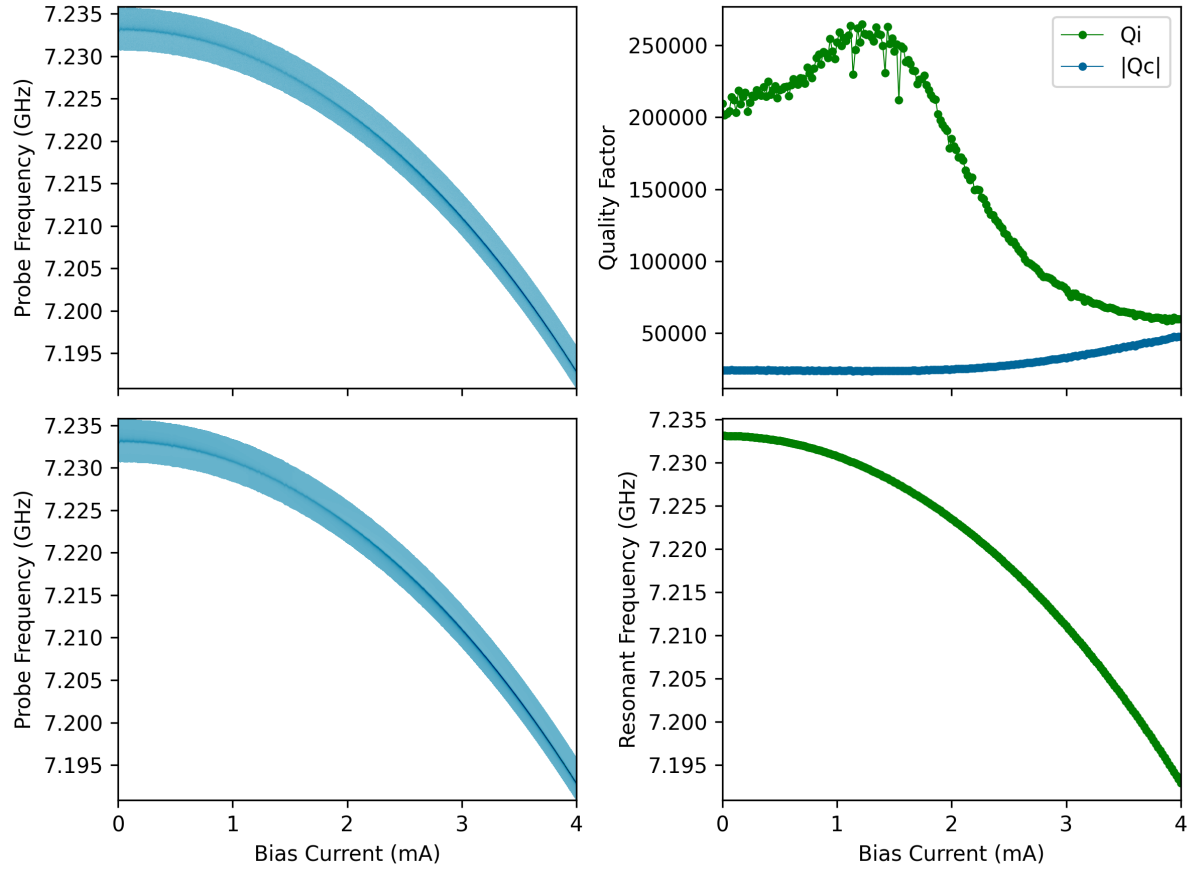
Figure 4.5: Magnitude response (top left) and fit (bottom left) of a similar device to the KIPA. Coupling and internal quality factors were extracted from the fits (top right), as was the resonance frequency (bottom right).
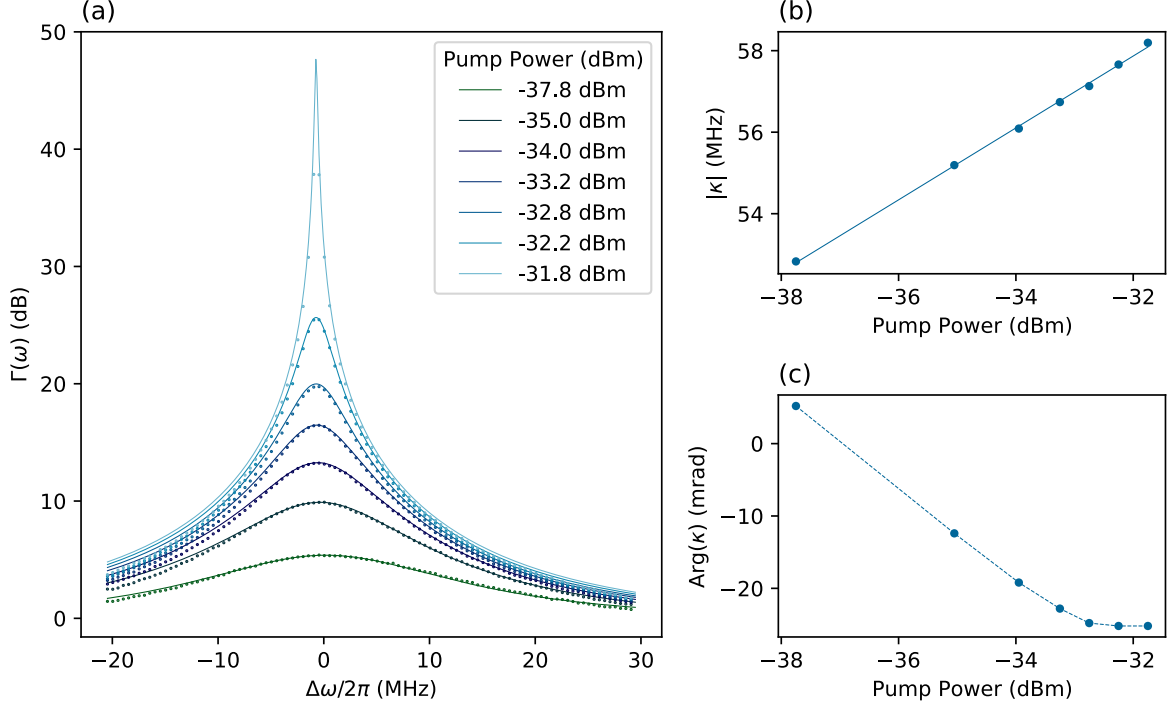
Figure 4.6: (a) Phase insensitive gain as a function of frequency $\omega = \Delta\omega + \omega_p/2$ for different pump powers (circles). Traces are labelled by the pump power at the cavity input. The fitted theoretical frequency response is plotted (solid lines). The parameters $|\kappa|$, $\mathrm{Arg}(\kappa)$ and the pump line transmittance λ_p were the only free parameters. (b) $|\kappa|$ as a function of the estimated pump current in the device (circles), with linear fit (solid line). (c) $\mathrm{Arg}(\kappa)$ as a function of pump power. The dashed line is a guide for the eye.

20 dB of gain with this bias current was within 15 dB of the maximum operating power of our source. Weaker biases may necessitate additional amplification of the pump tone, additional filtering (with associated insertion loss) between the KIPA and the HEMT, and/or increases the potential for sample heating. Hence, to simplify the initial experiments, we characterise the KIPA's performance as a microwave amplifier and a squeezer at a bias current close to the critical current. The value of $I_{\mathrm{DC}} = 0.834$ mA is used for the remainder of the experiments presented in this thesis.

4.4 Phase Insensitive Gain

Phase insensitive gain is readily observable using a VNA once an appropriate pump tone and bias current are applied to the device concurrently. For the following measure-

ments we chose a pump frequency of $\omega_p/2\pi = 14.381\,\mathrm{GHz} \approx \omega_0/\pi$, close to twice the resonant frequency of $\omega_0 = 7.1924$ GHz for the bias current $I_{\mathrm{DC}} = 0.834$ mA. Ideally, the KIPA should be operated at precisely $\omega_p = 2(\omega_0 + \delta\omega)$ for maximal squeezing (see Section 5.5.1). However, in our experiments we optimised the pump frequency for gain at a fixed pump power and bias current, arriving at a close to optimal pump configuration. A fixed pump frequency of $\omega_p/2\pi = 14.381$ GHz is used throughout these experiments despite the expected shift in resonance (see Equation 3.39).

The VNA supplies a signal tone, which is swept about $\omega_p/2$, while the reflected response from the KIPA is measured. Because the magnitude response of the KIPA is approximately flat, we measure gain by taking the difference between the response with the pump on and the pump off, depicted in Figure 4.6 at different pump powers. The KIPA produces an amplified signal tone ω_s at its output, along with an idler at ω_i such that energy is conserved in the 3WM process $\omega_p = \omega_s + \omega_i$. Phase insensitive gain occurs when $\omega_s = \omega_p/2 + \Delta\omega$ with $|\Delta\omega|$ exceeding the measurement bandwidth resolution. Gain increases with the pump power and is found to be in excess of $40\,\mathrm{dB}$ before the KIPA crosses the threshold where spontaneous parametric oscillations occur (see below).

4.4.1 Gain Feature Fits

To characterise the line-shape of the amplification feature, we assume that the KIPA operates as an ideal DPA and use Boutin's reflection parameter for the signal gain rewritten in the lab frame ($g_S[\omega] \to \Gamma(\omega)$ using $\omega \to \omega - \omega_p/2$: see Equation 2.87) [5]:

$$\Gamma(\omega) = \frac{\kappa(\kappa+\gamma)/2 + i\kappa(\Delta + \omega - \omega_p/2)}{\Delta^2 + \left[(\kappa+\gamma)/2 + i\omega - i\omega_p/2\right]^2 - |\xi|^2} - 1 \tag{4.11}$$

To fit the data in Figure 4.6, we adopt a complex coupling rate in the reflection model $\Gamma(\omega)$ (Equation 4.11): $\kappa \in \mathbb{R} \to \kappa \in \mathbb{C}$, with complex phase $\mathrm{Arg}(\kappa)$. A complex quality factor may be used to model an asymmetric response that occurs due to an impedance mismatch across the coupling circuit where reflections at the coupler interfere with photons exiting the resonator [58]. This is a standard trick [59] [58], which has been routinely used in our lab to fit similar NbTiN resonators showing clear evidence of an asymmetric magnitude response, including the fits depicted in Figure 4.5.

The pump current in our device is not precisely known. Assuming the simulated impedance of $Z_0 = 45\Omega$, we introduce a loss parameter λ_p that quantifies the amount

of pump power transmitted from room temperature down to the sample such that $I_p^2 = 2\lambda_p P_{\text{pump}}/Z_0$, where P_{pump} is the pump power at room temperature.

We may predict the parameter $\Delta = \omega_0 + \delta\omega - \omega_p/2$ from our theory (Equation 3.39) as ω_p and I_{DC} are known, and we have measured ω_0 and I_2^* in Section 4.3. Further, Equation 3.38 allows us to also predict $|\xi|$ as a function of the pump current in the sample. To further constrain the model we estimate the internal quality factor $Q_i = \omega_0/\gamma$ to be 10^5 for all pump powers. We base this estimate on the internal quality factors observed in similar devices (e.g. the device measured in Figure 4.5), and note that in the over-coupled regime Q_i has minimal impact on the predicted gain as $\kappa + \gamma \approx \kappa$.

We are left with a model where the only free parameters are $|\kappa|$, $\text{Arg}(\kappa)$ and λ_p. We impose the additional constraint that λ_p is constant across each of the pump powers. Fits were performed using the *FitKit* fitting framework in Python [60].

We observe a log-linear shift in κ from ~ 52 MHz to ~ 56 MHz corresponding to a coupling quality factor of $Q_c \approx\sim 135$. There are two plausible explanations for the change in κ with pump power. The pump current increases the kinetic inductance thus modifying the loading on the coupling circuit which results in a shift in coupling rate κ. Alternatively, an error in the estimate of ω_0 and hence $\delta\omega$ can be compensated for by a shift in κ by the model. Likely a combination of both effects occurs here. To minimise the error on the fit to ω_0, one could redevelop the theory with an additional quartic term in the expansion for kinetic inductance (Equation 2.105) and reduce errors in the fit to the frequency shift depicted in Figure 4.4. A weak drift (~ 30 mrad) in the phase of the coupling rate was necessary to fit the data (see Figure 4.6c). This is not unreasonable, as a small shift in the cavity impedance due to the pump current will influence any reflections that occur at the cavity input.

From the fits, we extract a pump attenuation of $-10\log(\lambda_p) = 35.75$ dB. Based on the room temperature attenuation of the lines and room temperature insertion losses of components, we estimate this loss to be on the order of ~ 30 dB. We find good agreement between experiment in theory here as the ~ 6 dB discrepancy may be explained by loss in the band-pass region of the PBG filter and the drop in pump current due to slight pump depletion, neither of which are taken into account in the loss estimate of 30 dB. We aim to characterise both the pump loss in the PBG structure and the pump depletion phenomenon in our device in future measurements to validate the extracted value of λ_p.
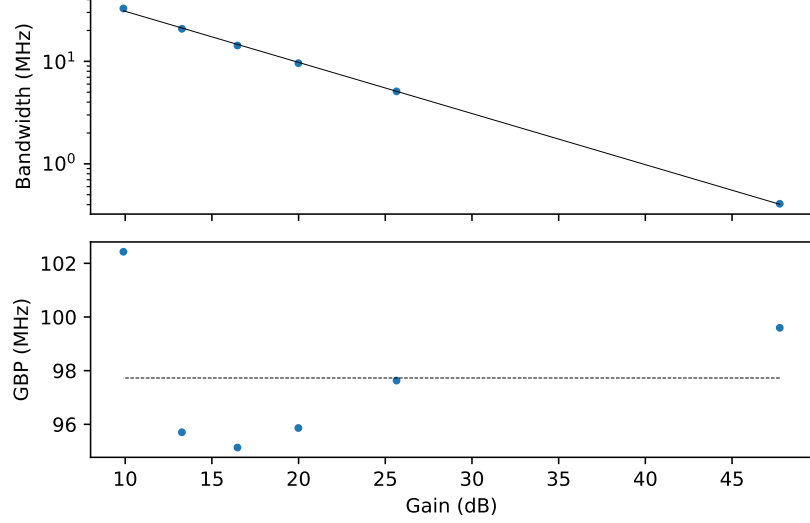
Figure 4.7: Bandwidth vs peak phase insensitive gain (top) and Gain Bandwidth Product (GBP) vs peak phase insensitive gain (bottom). The solid black line is a log-linear fit to the bandwidth as a function of gain in dB. The dashed black line is the average GBP across all gains.

Overall, we find excellent quantitative agreement with our theory, and are able to predict the observed gain curves from our expression for the KIPA Hamiltonian (Equations 3.40, 3.38 and 3.39) derived in the previous chapter.

4.4.2 Gain Bandwidth Product

From the fits to the amplification features depicted in Figure 4.6, we can extract the Gain Bandwidth Product (GBP), defined by the product of the peak phase insensitive gain G and the bandwidth when the gain drops to $G/2$ [22]. We find that the GBP of the KIPA shows good consistency across the different pump powers, as evidenced by the highly linear log-log plot of the gain and bandwidth (see Figure 4.7), and we extract an average GBP of 98 MHz.

4.4.3 Parametric Self Oscillations

Increasing the pump current I_p, and hence the mixing strength ξ, will not increase the gain indefinitely. Past a certain threshold, the device enters the regime of parametric self-oscillation and ceases to behave as an amplifier [61]. Pumped at twice the resonant
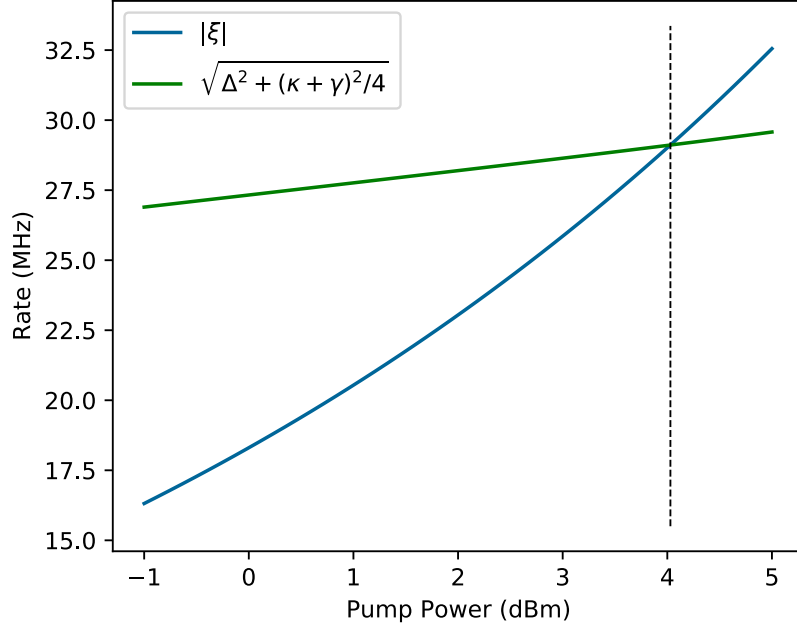
Figure 4.8: The mixing rate $|\xi|$ and parametric self oscillation threshold $\sqrt{\Delta^2 + (\kappa + \gamma)^2/4}$ vs the pump power at the output of our microwave source. The parametric self oscillation threshold occurs at the intersection of these curves indicated by the black dashed line at $P_{\mathrm{pump}} = 4.033$ dBm.

frequency, the cavity spontaneously produces photons at ω_0 that grow exponentially in number [61]. Competition from system non-linearities eventually limit growth, resulting in a fixed power ω_0 tone in steady state.

Although, we do not study the KIPA in the self-oscillation regime in this work, we have sufficient theory to predict the range of pump currents at which the KIPA behaves as a parametric amplifier. The parametric oscillation threshold corresponds to the zero crossing of the denominator of $|\Gamma(\omega)|$. At the point of maximum phase sensitive amplification, spontaneous oscillations occur when $|\xi|^2 \geq \Delta^2 + (\kappa + \gamma)^2/4$. Using our theory (Equations 3.38 and 3.39) along with the coupling rate $|\kappa|$ extracted from the fits depicted in Figure 4.6, we can predict the pump current at which parametric self-oscillation occurs. We assume a real coupling rate κ to simplify the analysis.

Figure 4.8 depicts the predicted $|\xi|$ as a function of pump power alongside the predicted threshold of parametric self-oscillation: $\sqrt{\Delta^2 + (\kappa + \gamma)^2/4}$. The threshold increases with the pump power due to the pump dependent detuning $\delta\omega$, which increases Δ^2 as the pump current increases. The curves intersect at a pump power of $P_{\mathrm{pump}} = 4.030$
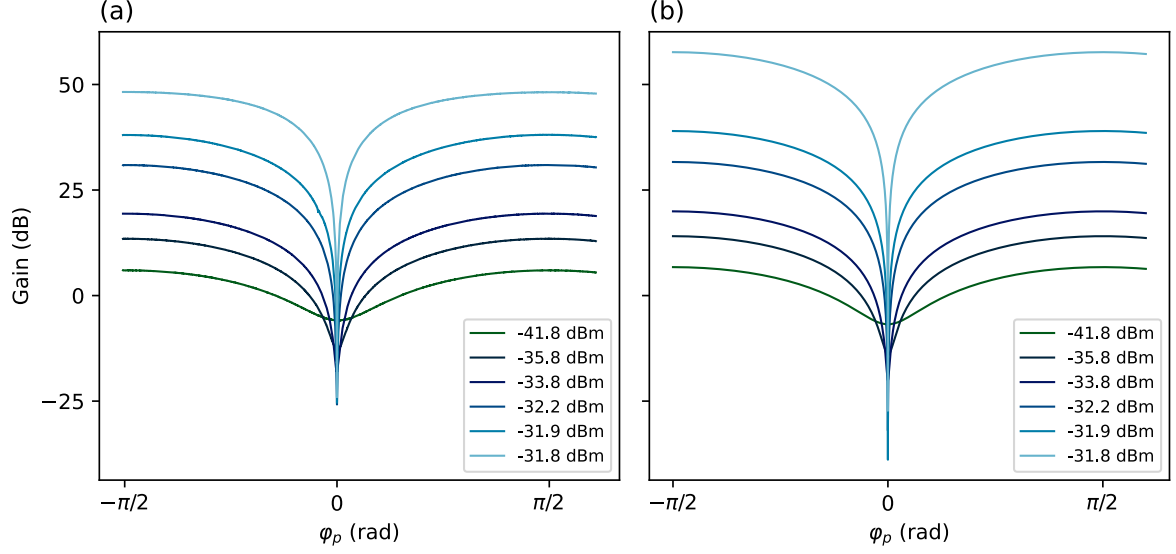
Figure 4.9: Measured gain (a) and theoretical gain (b) as a function of the pump/signal phase for an input signal of frequency $\omega_s = \omega_p/2$. Traces are labelled by the pump power at the cavity input. Disagreement between theory and experiment at the highest pump power (-31.8 dBm) is due to an increasing sensitivity of the peak theoretical gain to coupling rate $|\kappa|$. The discrepancy is explained by a small error in the fitted parameter, arising from the manual fitting process.

dBm referred to the output of our microwave source.

We found during the experiment that increasing the pump power to 4.10 dBm from 4.00 dBm would cause the KIPA to self-oscillate. Again, we find excellent quantitative agreement between experiment and theory.

4.5 Phase Sensitive Amplification

When applying a signal tone at half the pump frequency $\omega_s = \omega_p/2$, the KIPA enters the degenerate mode of operation, producing phase sensitive gain as the signal and idler tones interfere. From Boutin's input output equations (see Equation 2.87), the rotating frame gain is: $\Gamma(\varphi_p) = g_S[0] + g_I[0]$. More explicitly, the phase sensitive gain is:

$$|\Gamma(\varphi_p)| = \left| \frac{\kappa(\kappa + \gamma)/2 + i\kappa\Delta + i\kappa|\xi|e^{-j\varphi_p}}{\Delta^2 + (\kappa + \gamma)^2/4 - |\xi^2|} - 1 \right| \tag{4.12}$$

$$= \sqrt{\left[\frac{\kappa((\kappa + \gamma)/2 - |\xi|\sin(\varphi_p))}{\Delta^2 + (\kappa + \gamma)^2/4 - |\xi|^2} - 1 \right]^2 + \left[\frac{\kappa(\Delta + |\xi|\cos(\varphi_p))}{\Delta^2 + (\kappa + \gamma)^2/4 - |\xi|^2} \right]^2} \tag{4.13}$$

where we separate out the modulus of ξ and its argument corresponding to the pump phase φ_p (see Equation 3.38). From Equation 4.13 we observe that the KIPA gain is sensitive to the pump phase φ_p.

Experimentally, we observe phase sensitive amplification by modulating the phase of a signal tone of frequency $\omega_p/2 = 7.1905$ GHz, as is described in Section 4.2. As φ_p represents the phase difference between the signal and the pump, phase modulation of either tone will allow us to characterise the phase sensitive gain. Figure 4.9a depicts the gain of the KIPA as a function of pump phase, where up to 26 dB of de-amplification and close to 50 dB of amplification are observed. Compared to phase insensitive amplification, additional gain is observed in degenerate mode due to the constructive interference that occurs between the signal and idler. The traces are aligned such that the point of maximum de-amplification occurs for $\varphi_p = 0$.

Figure 4.9b depicts the phase sensitive gain predicted by our theory (Equation 4.13), where we apply the linear fit to κ shown in Figure 4.6, the extracted pump loss $\lambda_p = 35.75$ dB, and the pump current dependent expressions for ξ and $\delta\omega$ from our Hamiltonian derivation (Equations 3.38 and 3.39). We find excellent agreement in theory for each pump power aside from $P_p = -31.8$ dBm. Both the degenerate and non-degenerate gain become increasingly sensitive to the value of κ as the asymptote of parametric self oscillation is approached. Consequently, the discrepancy in the predicted phase sensitive gain at the highest pump power before self-oscillation may be explained by small errors in the linear fit to κ (see Figure 4.6). Further, the theory predicts greater de-amplification than is observed experimentally for the three highest operating points. To obtain the data plotted in Figure 4.9a, significant averaging was required to reduce noise. We believe that the maximum de-amplification of 26 dB measured is limited by our ability to resolve the sharp gain feature at $\varphi_p = 0$, which is highly sensitive to instrumental phase noise and slow phase drifts between the signal and pump.

4.6   1dB Compression Power

We anticipate that the KIPA is most likely to be used as a phase sensitive amplifier where input referred noise is minimal. As such, the 1 dB compression point of the KIPA is characterised here in phase sensitive mode. After calibrating the phase of the pump
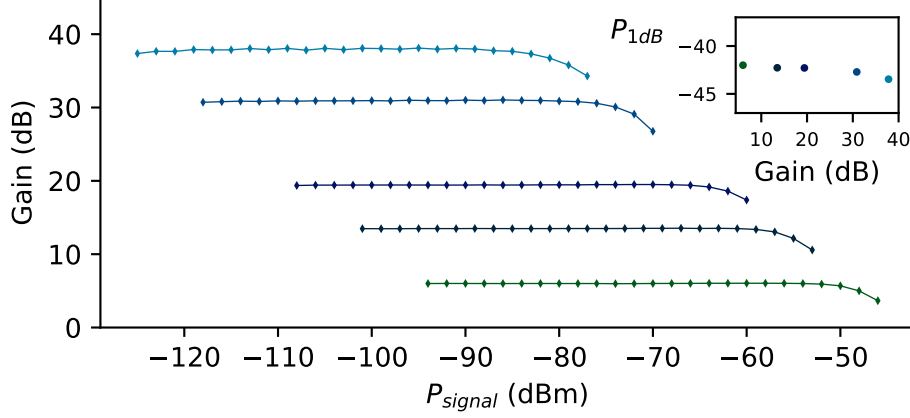
Figure 4.10:   Peak phase sensitive gain as a function of the input signal power at the sample, with 1 dB compression power (referred to the output of the device) as a function of the KIPA gain (inset).

to achieve maximum amplification (i.e. $\varphi_p \approx \pi/2$), we characterise the degenerate 1 dB compression point of the KIPA by increasing the signal power until the gain drops by 1 dB, as is presented in Figure 4.10. For $\sim 20\,\mathrm{dB}$ of phase sensitive gain, we find a minimum compression power of $-43\,\mathrm{dBm}$ at the KIPA output, comparable to the compression performance of kinetic inductance travelling wave amplifiers [51, 18, 20].

Our HEMT saturates for approximate input powers of ~ -50 dBm. Factoring in the loss between the KIPA and the HEMT, we are unable to rule out the possibility that the measured the 1 dB compression point is limited by the HEMT, and that the dynamic range of the KIPA is indeed higher. We speculate that the linear range of operation for the KIPA is limited either by the critical current of the film or by two photon losses, which become significant at high input powers [32].

Among the family of quantum limited amplifiers, the KIPA offers unprecedented levels of gain with a 1 dB compression comparable to the state-of-the-art.

Chapter 5

Quantum Characteristics

In this chapter we document a series of experiments used to understand the quantum behaviour of the KIPA. While we have not yet successfully measured squeezing with the KIPA, we show near quantum limited noise performance and provide a body of evidence to support the claim that the KIPA behaves as a highly idealised DPA.

I'd like to acknowledge Dr Arne Grimmsmo for his contributions to the noise temperature theory presented here.

5.1   Experimental Setup

For the experiments outlined in this chapter, we use the same Cryogenic setup as described in Chapter 4. However, a different room temperature setup is required for homodyne detection and the characterisation of the KIPA noise temperature, as is depicted in Figure 5.1.

The output of the fridge connects directly to a $\sim$ 30 dB gain microwave HEMT low noise amplifier. In our efforts to measure squeezing and the noise temperature of our device, it is desirable to minimise the noise along the detection chain where possible. However, we note that the dominant source of detection chain noise arises from the HEMT at 4 K. A microwave switch follows the microwave amplifier, allowing us to select between a spectrum analyser or an IQ demodulator for microwave detection.

Our homodyne detection setup consists of an IQ mixer (IQ4509, Marki Microwave Inc), driven by a local oscillator supplied from an additional microwave source (E8267D, Keysight Technologies) that is phase-locked with the pump source using a 1 GHz refer-
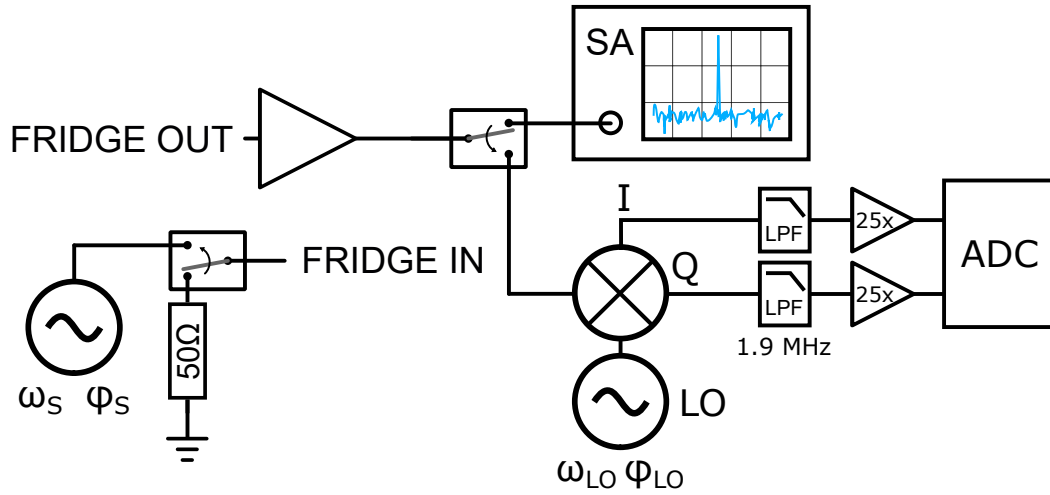
Figure 5.1: The room temperature setup used for the experiments in this chapter. A microwave switch passes a coherent signal tone of frequency ω_s and variable phase φ_s to the input of the fridge, or disables the input altogether with a 50Ω load allowing the KIPA cavity to reside in the vacuum state. The detection path now consists of a room temperature microwave amplifier followed by a homodyne detection circuit driven by an independent microwave source as the local oscillator. The baseband I and Q signals are low pass filtered down to 1.9 MHz and then amplified further before digitisation by an ADC. Alternatively, a microwave switch can redirect the detected microwaves to a spectrum analyser used to characterise the noise temperature of the KIPA.

ence. The high frequency reference is crucial to slowing phase drifts between the sources, allowing for longer measurement times and more averaging before we are required to re-calibrate the measurement. The baseband I and Q quadratures output from the mixer are then filtered by 1.9 MHz low pass filters (SLP-1.9+, Mini-Circuits Technologies) and then amplified by a series pair of $5\times$ JFET pre-amps (SIM914, Stanford Research Systems), providing a baseband gain of $\sim$ 18 dB. The amplified baseband signal is then sampled at 6.25 MHz using two digitiser channels of a PXI card (M3300A, Keysight Technologies).

We begin this chapter by imaging the squeezing transformation (see Section 5.2) where we supply a microwave tone at the degenerate amplification frequency ($\omega_s = \omega_p/2$) and vary its phase using a third microwave source (E8267D, Keysight Technologies) that is again phase-locked with the pump and local oscillator using the 1 GHz reference clock. By probing the KIPA output for different signal phases (φ_s) we may image the phase sensitive transformation of the output field using our homodyne detection setup.

In addition, we study the output noise spectrum of the detection chain as a function of fridge temperature and in the absence of a coherent tone, allowing us to extract the noise temperature of the KIPA. For these experiments we use the microwave switch on the detection side to select the spectrum analyser.

In the remaining measurements, we study the response of the KIPA to input vacuum fluctuations where we measure squeezing and perform statistical analyses of the noise field. To prepare the KIPA cavity in the vacuum state, we use a microwave switch on the fridge input to provide a 50Ω termination. The 50Ω load presents 300 K noise to the input line, which we have previously shown is sufficiently attenuated along the signal line down to 20 mK such that vacuum fluctuations are the dominant source of noise at the operating frequency of $\sim$ 7 GHz (see Section 4.1.1).

5.2   The Squeezing Transformation

The phase-dependent interference of the signal and idler fields in a DPA results in an affine transformation applied to the IQ-plane of the input field, also commonly called the squeezing transformation [1]. As this affine transformation acts equally on both coherent inputs and the vacuum, we begin with a characterisation of the squeezing transformation for coherent inputs. The fields, which initially occupy a circular region on the IQ-plane,
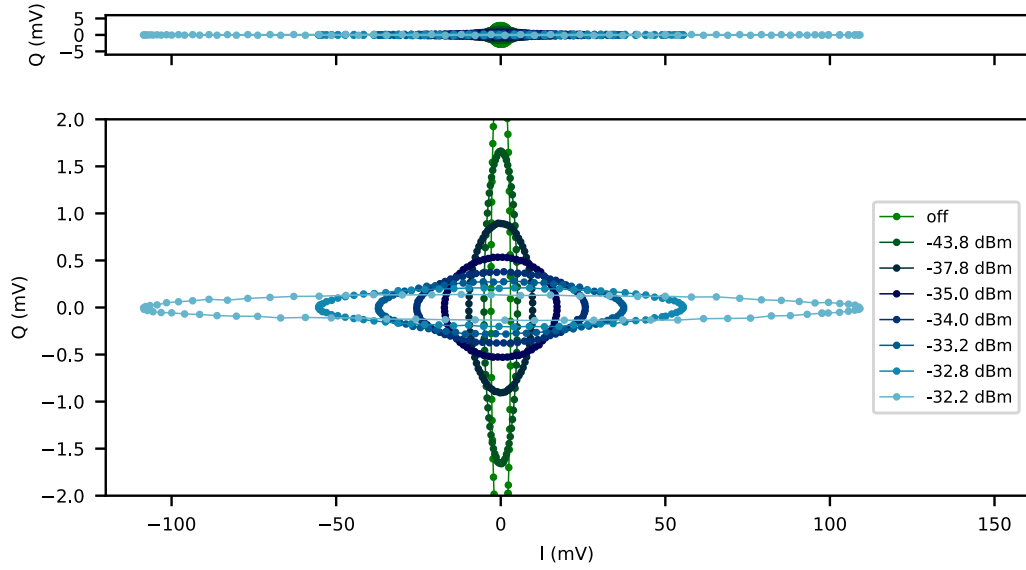
Figure 5.2: KIPA response to coherent inputs of constant amplitude and varying phase plotted on two different scales. Top: outputs are plotted with an equal aspect ratio, where the reflected input sweep with the KIPA off is observed as a circle (green). Turning the KIPA on stretches the circle to an ellipse, which resembles a blue line in this plot. Bottom: the same outputs plotted with an exaggerated scale along Q so that the elliptical transformation may be observed. Solid lines are a guide for the eye.

are stretched to form an ellipse, with the area being conserved in the process. One quadrature is amplified, while the orthogonal quadrature is said to be 'deamplified'. Coherent states are useful for studying the squeezing transformation since any noise field that couples into the cavity through the loss channel γ may be neglected (see Section 5.3), permitting a clear inspection of any deviations from the expected transformation. Hamiltonian non-idealities manifest as an S or 'banana'-shaped distortion (see Figure 2.8) of the phase space at high gains, as has been experimentally observed [7, 6] and modelled [5] in JPAs for gains typically exceeding $\sim 10\,\mathrm{dB}$. While the deamplification of coherent inputs are related to a device's squeezing potential, the deamplification level is not in general equal to squeezing as mixing of the bath field contributes additional variance to the squeezed vacuum. Instead, the de-amplification presents an upper limit on the squeezing a device may produce.

We probe the squeezing transformation by sweeping the phase of a coherent state incident on the KIPA and use homodyne detection to measure the transformed output. A coherent tone of power -100 dBm at the KIPA input, corresponding to approximately 250 intracavity photons on average. This input power was optimised to provide good signal-to-noise without saturating the amplifier chain. Our results are shown in Figure 5.2 for different pump powers. When the KIPA is off the input coherent state phase sweep traces out a circle on the IQ-plane. Activating the KIPA maps the circle to an ellipse at the detector with no noticeable S-type distortion, even for a degenerate gain of 30 dB. This exceeds the achievable phase-sensitive gain without distortion observed in JPAs by approximately two orders of magnitude [7, 6]. Further, increases in gain (up to 50 dB) did not produce any obvious distortions, though at these higher gains the signal power had to be reduced to avoid saturating the cryogenic HEMT and room temperature amplifiers, resulting in significant degradation in the SNR. The lack of S-type features at high gain support the idea that the KIPA is well-approximated by an ideal DPA and that the self-Kerr correction may be neglected.

In the following sections, we show that the data illustrated in Figure 5.2 may be entirely explained by the input output theory of the ideal DPA in conjunction with weak microwave reflections that occur in the experimental setup, providing further evidence that the KIPA behaves as a highly idealised squeezer.

5.3 Squeezing Transformation of the DPA

Re-writing Boutin's input ouptput relation (Equation 2.86) in the degenerate case $(\omega = 0)$ [5], we find:

$$a_{\text{out}} = g_s a_{\text{in}} + g_i a_{\text{in}}^\dagger + \sqrt{\frac{\gamma}{\kappa}}\left((g_s + 1)b_{\text{in}} + g_i b_{\text{in}}^\dagger\right) \tag{5.1}$$

$$a_{\text{out}}^\dagger = g_s^* a_{\text{in}}^\dagger + g_i^* a_{\text{in}} + \sqrt{\frac{\gamma}{\kappa}}\left((g_s^* + 1)b_{\text{in}}^\dagger + g_i^* b_{\text{in}}\right) \tag{5.2}$$

giving the output quadrature relations:

$$I_{\text{out}} = \frac{1}{2}(a_{\text{out}}^\dagger + a_{\text{out}}) \tag{5.3}$$

$$= \frac{1}{2}\left[\epsilon a_{\text{in}} + \epsilon^* a_{\text{in}}^\dagger + \sqrt{\frac{\gamma}{\kappa}}\left((\epsilon + 1)b_{\text{in}} + (\epsilon^* + 1)b_{\text{in}}^\dagger\right)\right] \tag{5.4}$$

$$Q_{\text{out}} = \frac{i}{2}(a_{\text{out}}^\dagger - a_{\text{out}}) \tag{5.5}$$

$$= \frac{i}{2}\left[\epsilon'^* a_{\text{in}}^\dagger - \epsilon' a_{\text{in}} + \sqrt{\frac{\gamma}{\kappa}}\left((\epsilon'^* + 1)b_{\text{in}}^\dagger - (\epsilon' + 1)b_{\text{in}}\right)\right] \tag{5.6}$$

where $\epsilon = g_s + g_i^*$ and $\epsilon' = g_s - g_i^*$. Using the identities:

$$\frac{1}{2}\left[\epsilon^* a^\dagger + \epsilon a\right] = \text{Re}(\epsilon)I - \text{Im}(\epsilon)Q \tag{5.7}$$

$$\frac{i}{2}\left[\epsilon^* a^\dagger - \epsilon a\right] = \text{Re}(\epsilon)Q + \text{Im}(\epsilon)I \tag{5.8}$$

we arrive at a set of linear equations for the output field quadratures:

$$\begin{pmatrix} I_{\text{out}} \\ Q_{\text{out}} \end{pmatrix} = A_G \begin{pmatrix} I_{\text{in}} \\ Q_{\text{in}} \end{pmatrix} + \sqrt{\frac{\gamma}{\kappa}}(A_G + \mathbb{1}) \begin{pmatrix} I_b \\ Q_b \end{pmatrix} \tag{5.9}$$

where I_b and Q_b are the quadratures of the bath field. As a function of the pump phase φ_p, the affine transformation of the quadratures A_G is given by:

$$A_G(\varphi_p) = \begin{pmatrix} \text{Re}(\epsilon) & -\text{Im}(\epsilon) \\ \text{Im}(\epsilon') & \text{Re}(\epsilon') \end{pmatrix} \tag{5.10}$$

$$= \frac{\kappa}{\Delta^2 + (\kappa + \gamma)^2/4 - |\xi|^2}\begin{pmatrix} (\kappa + \gamma)/2 - |\xi|\sin(\varphi_p) & -|\xi|\cos(\varphi_p) + \Delta \\ -|\xi|\cos(\varphi_p) - \Delta & (\kappa + \gamma)/2 + |\xi|\sin(\varphi_p) \end{pmatrix} - \mathbb{1} \tag{5.11}$$

The pump phase φ_p has the effect of rotating the basis of the transformation. In fact, one can show that $A_G(\varphi_p) = R^T(\varphi_p)A_G(0)R(\varphi_p)$ where $R(\theta)$ is the standard 2×2 rotation matrix.
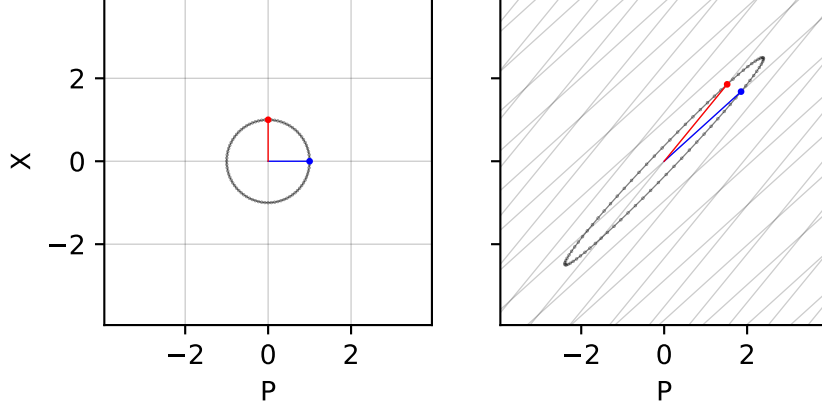
Figure 5.3: Visualisation of the linear transformation $A_G(0)$ acting on points on the unit circle. The red (blue) points/lines correspond to the standard basis vectors in V.

As the bath is a thermal state, taking the expectation of both sides of Equation 5.9 gives the simple expression:

$$\begin{pmatrix} \langle I_{\text{out}} \rangle \\ \langle Q_{\text{out}} \rangle \end{pmatrix} = A_G(\varphi_p) \begin{pmatrix} \langle I_{\text{in}} \rangle \\ \langle Q_{\text{in}} \rangle \end{pmatrix} \tag{5.12}$$

Assuming $\Delta = 0$ we find $A_G \to \mathbb{1}$ in the limit that $|\xi| \to 0$, as expected. Conversely, if $\Delta \neq 0$ then A_G is an affine transformation that will always mix the input quadratures to some degree, limiting the achievable squeezing for a given mixing rate ξ. Figure 5.3 illustrates the mapping of points on the unit circle $(I, Q)^T = (\sin(\phi), \cos(\phi))^T$ in the vector space $V \in \mathbb{R}^2$ by the linear transformation $A_G(0) : V \to W$. Setting $\varphi_p = 0$ yields a mapping where the standard unit vectors in V do not map to the standard unit vectors in W, nor do they correspond to the principal axes of the elliptical output state.

We may align the axis of amplification along Q, as depicted in Figure 5.4, by choosing $\varphi_p = \pi/2 - \arccos(-\Delta/|\xi|)$. Note that in Figure 5.4, we deliberately set $\Delta \neq 0$ to illustrate the fact that orthogonal vectors in V do not necessarily map to orthogonal vectors in W. On the other hand, when $\Delta = 0$, the optimal angle of rotation will correspond to $\varphi_p = 3\pi/2$ giving a strictly diagonal matrix $A_G(\varphi_p)$ with partial diagonal elements $(\kappa + \gamma)/2 + |\xi|$ and $(\kappa + \gamma)/2 - |\xi|$, such that orthogonality is preserved. Degenerate amplification increases as $|\xi|$ approaches the asymptote of self oscillation ($|\xi|^2 = \Delta^2 + (\kappa + \gamma)^2/4$), while simultaneously, deamplification approaches 0.
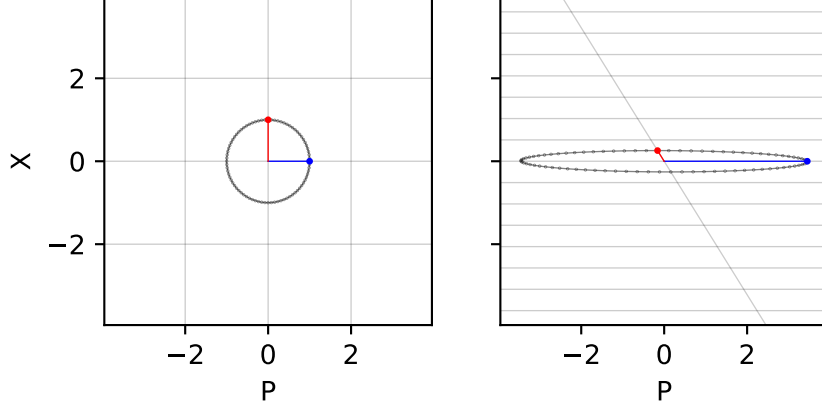
Figure 5.4: Visualisation of the linear transformation $A_G(\pi/2 - \arccos(-\Delta/|\xi|))$ acting on points on the unit circle. The red (blue) points/lines correspond to the standard basis vectors in V.

The expression for gain as a function of the pump phase φ_p, as given by:

$$g(\varphi_p) = \frac{||(\langle I_{\text{out}} \rangle, \langle Q_{\text{out}} \rangle)^T||}{||(\langle I_{\text{in}} \rangle, \langle Q_{\text{in}} \rangle)^T||} \tag{5.13}$$

$$= \sqrt{\frac{(I_{\text{in}} g_{11}(\varphi_p) + Q_{\text{in}} g_{12}(\varphi_p))^2 + (I_{\text{in}} g_{21}(\varphi_p) + Q_{\text{in}} g_{22}(\varphi_p))^2}{I_{\text{in}}^2 + Q_{\text{in}}^2}} \tag{5.14}$$

corresponds exactly with the expression for phase sensitive gain given earlier in Equation 4.13, where g_{ij} are the matrix elements of $A_G(\varphi_p)$.

5.3.1 Reflections with the Predicted DPA Transformation

The ellipses depicted in Figure 5.2 are not simply a result of the squeezing transformation applied to coherent inputs of fixed magnitude. Because our setup is not perfectly impedance matched, reflections will occur at the input to KIPA (e.g. from the PCB and input connector) that superimpose on the squeezing transformation. Although these reflections are account for a small percentage of the detected signal, they become considerable as the deamplification increases.

To be precise, we define 'reflections' to be the total microwave signal that propagates towards the HEMT input that has not been amplified by the KIPA. The total reflected signal will have a constant amplitude that is a fraction of the input amplitude, and, relative to the KIPA output, will be offset in phase according to the difference in path length. Taking the vector sum between the total reflected signal and the phase sensitive
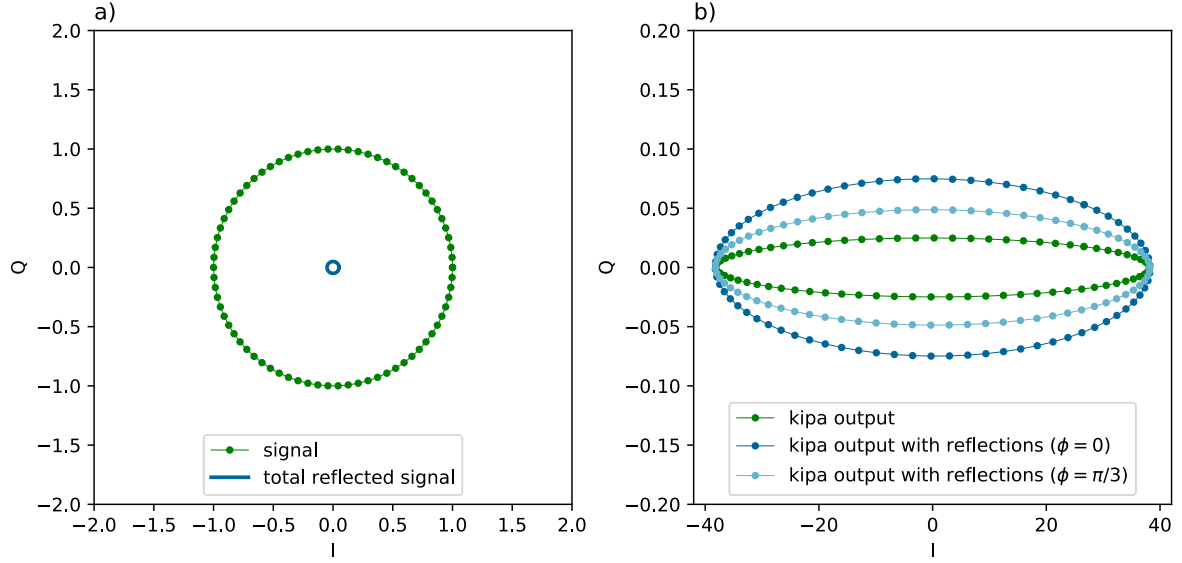
Figure 5.5: (a) An input signal (green) represented by points of constant amplitude on the IQ-plane, with a 5% reflected signal (blue). (b) The theoretical output of the KIPA (green) superimposed with the total reflected signal with a phase shift of zero (dark blue) and a phase shift of $\pi/3$ (light blue).

output of the KIPA gives a resulting ellipse that we observe at the output of our fridge (see Figure 5.5). That is,

$$\begin{pmatrix} \langle I_{\text{out}} \rangle \\ \langle Q_{\text{out}} \rangle \end{pmatrix} = \left[\mathcal{T} A_G(\varphi_p) + \mathcal{R} R(\phi) \right] \begin{pmatrix} \langle I_{\text{in}} \rangle \\ \langle Q_{\text{in}} \rangle \end{pmatrix} \tag{5.15}$$

where $\mathcal{T}$ is the fraction of the input signal transmitted to the KIPA, $\mathcal{R}$ is the fraction of the input signal that is reflected and $R(\phi)$ is the standard rotation matrix that accounts for a phase shift of ϕ. Figure 5.5b illustrates the effect of a 5% reflection on the measurement of the output of a DPA. In the worst case of $\phi = 0$, the output of the KIPA and the reflected signal constructively interfere and increase the observed deamplification by ~ 9 dB. The error introduced by the reflected signal will depend on the phase relationship between the KIPA output and the reflected signal, which in general is unknown. To proceed with the analysis, we define an in-phase reflection coefficient $\mathcal{R}'$ and set $\phi = 0$. The in-phase reflection coefficient $\mathcal{R}'$ represents a lower bound for the reflections that may occur in our setup.

Using Equation 5.15 combined with the DPA parameters extracted from the fits in Chapter 4 (κ, $|\xi|$, Δ, etc.), we are able to predict the transformation of a unit magnitude
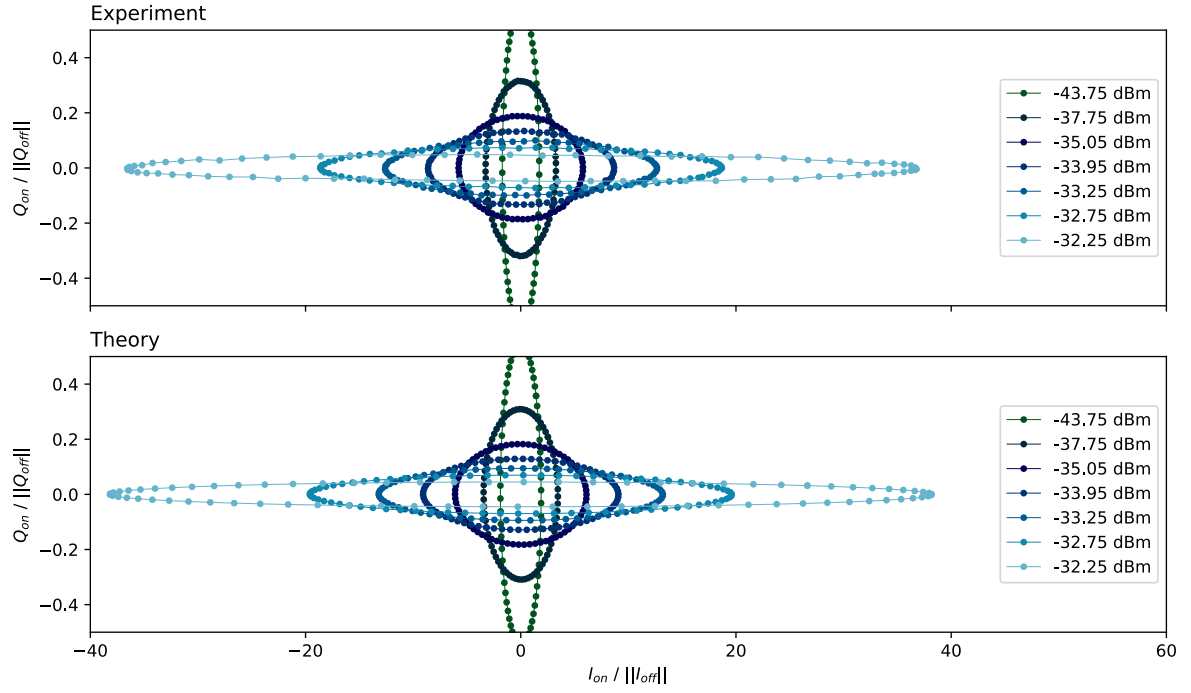
Figure 5.6: Top: Ellipses measured by sweeping the phase of a fixed amplitude input, normalised by the amplitude of the input ($||I_{\mathrm{off}}||$ or $||Q_{\mathrm{off}}||$). This is the same data as is presented in Figure 5.2. Bottom: Predicted ellipses from the DPA squeezing transformation with a 2% in-phase reflection coefficient.
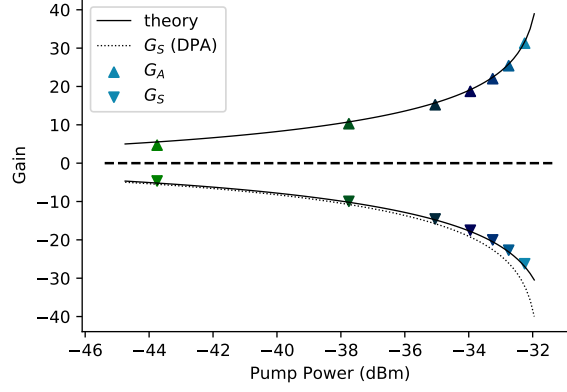
Figure 5.7: Amplification and de-amplification as a function of pump power (triangles) with theoretical gain with a 2% in-phase reflection coefficient (solid black lines). The predicted deamplification for an ideal DPA with no reflected component is also plotted (dashed black line), indicating the discrepancy produced by the reflected input.

input by the KIPA for different levels of in-phase reflection. We fit the in-phase reflection coefficient to be $\sim 2\%$ and find excellent agreement between theory and experiment (see Figure 5.6).

The most likely sources of reflections from our setup are the connection from the coaxial lines to our bespoke PCB, and at the junction between the PCB and the chip. Assuming $50\,\Omega$ lines down to the sample, a 2% reflection rate corresponds to an equivalent PCB impedance of:

$$Z_{\mathrm{PCB}} = Z_{\mathrm{CPW}}\frac{1 - \mathcal{R}}{1 + \mathcal{R}} = 48\ \Omega \tag{5.16}$$

which is entirely realistic accounting for the uncertainty in the design and manufacturing tolerances of the PCB.

The maximum deamplification level G_S is defined as the greatest reduction in amplitude of a coherent input by the squeezing transformation. We additionally define the maximum amplification level G_A as being the corresponding increase in gain that occurs orthogonal to the axis of deamplification. G_S and G_A are measured by comparing the input and output amplitudes of the ellipses presented in Figure 5.2 as a function of the input phase. We plot the maximum deamplification and maximum amplification in Figure 5.7, where up to $26\,\mathrm{dB}$ of deamplification is observed for $30\,\mathrm{dB}$ of amplification. We repeat the process of measuring G_S and G_A from our theoretically predicted ellipses over a finer sweep of pump powers, and again find excellent agreement with theory where the

fits deviate by less than 1 dB from the measurements. Deviation between experiment and theory seems to increase as the gain goes to zero. We attribute this to increased sensitivity to the quadrature and phase imbalance of our demodulator at low gains. We observe some asymmetry $G_S \neq G_A$ in our data as shown in Figure 5.7, as has been attributed to weak reflections in the experimental setup. The ideal amplifier symmetrically transforms both quadratures (i.e. $G_S = G_A$) [1], however, according to our model for the squeezing transform, symmetry is broken if either $Q_i < \infty$ or $|\Delta| > 0$. While some asymmetry is expected, for our estimate of $Q_i = 10^5$ this asymmetry is small and is evident in Figure 5.7 where we show the predicted G_S for the reflection-less DPA measurement.

5.4   Noise Temperature

5.4.1   Non-Degenerate Noise Temperature Theory

The output fluctuations of the KIPA operating as a non-degenerate amplifier are given by the input output theory for the KIPA (Equation 2.86) as:

$$\langle \Delta I_{\text{out}}^2 \rangle = \left(|g_s|^2 + \frac{\gamma}{\kappa} |g_s + 1|^2 \right) \left(\frac{n_{\text{th}}}{2} + \frac{1}{4} \right) + |g_i|^2 \left(1 + \frac{\gamma}{\kappa} \right) \left(\frac{n_{\text{th}}}{2} + \frac{1}{4} \right) \tag{5.17}$$

where the signal and idler gains ($g_s(\omega)$ and $g_i(\omega)$) depend on the frequency of the signal being amplified.

One fundamental identity of the DPA is the relationship between the signal and idler gains [5]:

$$|g_i|^2 \left(1 + \frac{\gamma}{\kappa} \right) = |g_s|^2 + \frac{\gamma}{\kappa} |g_s + 1|^2 - 1 \tag{5.18}$$

which holds for all ω (see Equation 2.87), and is a by-product of the KIPA output field satisfying the commutation relation $[\hat{a}_{\text{out}}, \hat{a}_{\text{out}}^\dagger] = 1$. Substituting Equation 5.18 into our expression for the quadrature fluctuations along $\hat{I}$, we obtain:

$$\langle \Delta I_{\text{out}}^2 \rangle = \left(|g_s|^2 + \frac{\gamma}{\kappa} |g_s + 1|^2 \right) \left(n_{\text{th}} + \frac{1}{2} \right) - \frac{n_{\text{th}}}{2} - \frac{1}{4} \tag{5.19}$$

Referring the quadrature fluctuations to the input of the KIPA and subtracting the

vacuum contribution, we find:

$$\frac{\langle \Delta I_{\text{out}}^2 \rangle}{|g_s|^2} - \frac{1}{4} = \left(1 + \frac{\gamma}{\kappa}\frac{|g_s + 1|^2}{|g_s|^2}\right)\left(n_{\text{th}} + \frac{1}{2}\right) - \frac{n_{\text{th}}}{2|g_s|^2} - \frac{1}{4|g_s|^2} - \frac{1}{4} \tag{5.20}$$

$$\geq \frac{1}{4}\left(1 - \frac{1}{|g_s|^2}\right) + \frac{\gamma}{\kappa}\frac{|g_s + 1|^2}{2|g_s|^2} \tag{5.21}$$

$$\geq \frac{1}{4}\left(1 - \frac{1}{|g_s|^2}\right) \tag{5.22}$$

As required by Cave's fundamental theorem of phase sensitive amplifiers, the KIPA/DPA does indeed add 1/4 photons to the input referred noise in the limit of high gain [1]. Further, equality only holds in the limit of zero temperature $(T \to 0)$ and no losses $(\gamma \to 0)$.

To maintain consistency with the input-output models for phase sensitive amplifiers used later in this section (see Equation 5.34), we write the phase insensitive output of the KIPA as follows:

$$\langle \Delta I_{\text{out}}^2 \rangle = G_k\left(\frac{n_{\text{th}}}{2} + \frac{1}{4}\right) + (G_k - 1)\left(\frac{n_{\text{th}}}{2} + \frac{n_k}{2} + \frac{1}{4}\right) \tag{5.23}$$

where $G_k = |g_s|^2$ and n_k is the input referred noise contribution by the KIPA. Comparing Equation 5.19 with the $(G_k - 1)$ term from this expression we obtain a relation for the additional noise photons contributed by the KIPA n_k:

$$n_k = \frac{2}{|g_s|^2 - 1}\left(\langle \Delta I_{\text{out}}^2 \rangle - |g_s|^2\left(\frac{n_{\text{th}}}{2} + \frac{1}{4}\right)\right) - n_{\text{th}} - \frac{1}{2} \tag{5.24}$$

$$= \frac{2}{|g_s|^2 - 1}\left(\left(\frac{n_{\text{th}}}{2} + \frac{1}{4}\right)(|g_s|^2 - 1) + \frac{\gamma}{\kappa}|g_s + 1|^2\left(\frac{n_{\text{th}}}{2} + \frac{1}{2}\right)\right) - n_{\text{th}} - \frac{1}{2} \tag{5.25}$$

$$= \frac{\gamma}{\kappa}\frac{|g_s + 1|^2}{|g_s|^2 - 1}(n_{\text{th}} + 1) \tag{5.26}$$

The temperature dependence for n_k is depicted in Figure 5.8 for various internal quality factors, and using the same DPA parameters as were measured in the previous chapter. Compared to n_{th} the change in n_k is small even as we leave the over-coupled regime with $Q_i \sim 10^3$. At zero temperature n_k appears to decrease by an approximate order of magnitude for every increase in the order of magnitude for Q_i, further motivating the desire to maximise the Q_i of a DPA.

Operating the KIPA such that $\hbar\omega_0 \ll k_B T$, we have:

$$n_{k0} = \frac{\gamma}{\kappa}\frac{|g_s + 1|^2}{|g_s|^2 - 1} \tag{5.27}$$

We plot n_{k0} as a function of $Q_i = \omega_0/\gamma$ and observe rapid convergence to zero as $Q_i \to \infty$.
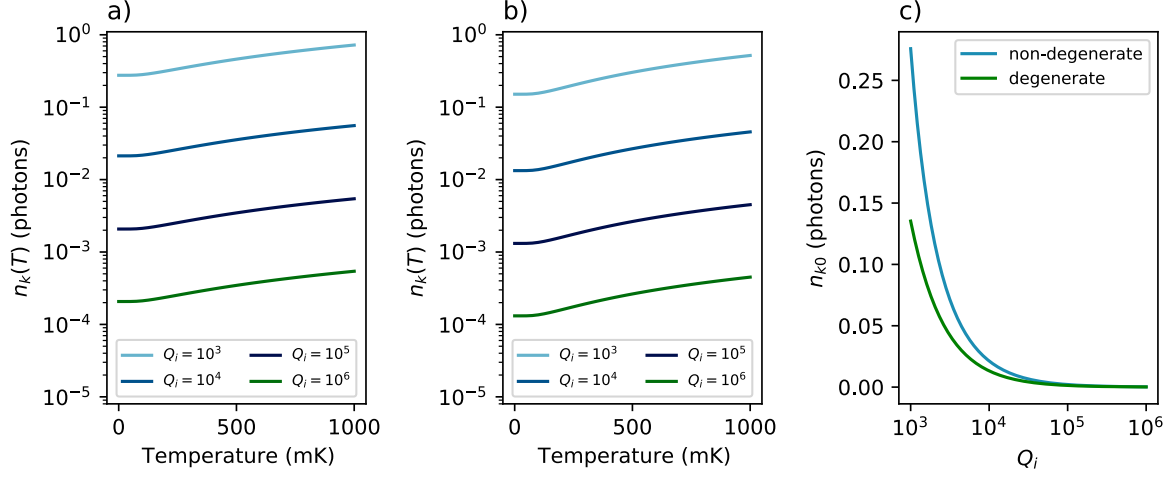
Figure 5.8: (a) The simulated non-degenerate noise photon number n_k as a function of temperature for different values of Q_i. (b) The simulated degenerate noise photon number n_k as a function of temperature for different values of Q_i. (c) The simulated degenerate (non-degenerate) noise photon number for $G_k = 31$ dB (25 dB) as a function of the internal quality factor Q_i.

5.4.2   Degenerate Noise Temperature Theory

The output fluctuations of the KIPA in degenerte mode as a function of the pump phase φ_p are given by (see Section 5.5.1):

$$\langle \Delta I_{\text{out}}(\varphi_p)^2 \rangle = |g_s + g_i^*(\varphi_p)|^2 \left(\frac{n_{\text{th}}}{2} + \frac{1}{4} \right) + \frac{\gamma}{\kappa} |g_s + 1 + g_i^*(\varphi_p)|^2 \left(\frac{n_{\text{th}}}{2} + \frac{1}{4} \right) \tag{5.28}$$

with phase sensitive power gain $G_k(\varphi_p) = |g_s + g_i^*(\varphi_p)|^2$. Referred to the KIPA input, the excess quadrature fluctuations contributed by the amplifier are:

$$\frac{\langle \Delta I_{\text{out}}(\varphi_p)^2 \rangle}{G_k(\varphi_p)} - \frac{1}{4} = \frac{n_{\text{th}}}{2} + \frac{\gamma}{\kappa} \frac{|g_s + 1 + g_i^*(\varphi_p)|^2}{|g_s + g_i^*(\varphi_p)|^2} \left(\frac{n_{\text{th}}}{2} + \frac{1}{4} \right) \geq 0 \tag{5.29}$$

As predicted by Caves, the excess quadrature fluctuations referred to the input can be as small as zero in limit of $\hbar\omega \ll k_B T$ and provided there are no losses in the system (i.e. $\gamma = 0$) [1].

Writing $G_k = |g_s + g_i^*(\varphi_p)|^2$, we define a similar expression to Equation 5.23 for the phase sensitive amplifier, along the amplified quadrature:

$$\langle \Delta I_{\text{out}} \rangle = G_k \left(\frac{n_{\text{th}}}{2} + \frac{1}{4} \right) + (G_k - 1) \left(\frac{n_k}{2} \right) \tag{5.30}$$

95
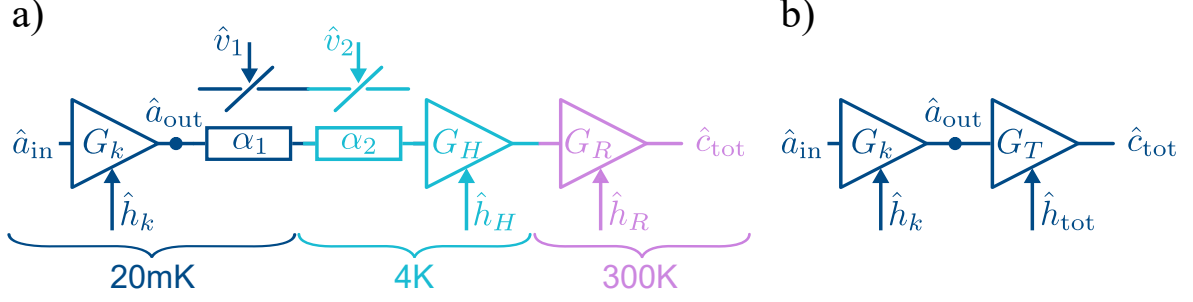
Figure 5.9: (a) The complete detection chain model, consisting of the KIPA and attenuator α_1 at 20mK, attenuator α_2 and the HEMT at 4K, and the room temperature amplifier at 300K. The attenuators are modeled as beam splitters, mixing in the thermal operators $\hat{v}_1$ and $\hat{v}_2$ with the detected field as it propagates along the detection chain. Each amplifier contributes noise to its output, denoted here by the field operators $\hat{h}_k$ (KIPA), $\hat{h}_H$ (HEMT), and $\hat{h}_R$ (room temperature amplifier). (b) The simplified detection chain model, where the attenuators and amplifiers after the KIPA may be modeled as an effective amplifier with gain G_T and noise field $\hat{h}_{\text{tot}}$.

with,

$$n_k = \frac{\gamma}{\kappa} \frac{|g_s + 1 + g_i^*|^2}{|g_s + g_i^*|^2 - 1} \left(n_{\text{th}} + \frac{1}{2} \right) \tag{5.31}$$

$$n_{k0} = \frac{\gamma}{2\kappa} \frac{|g_s + 1 + g_i^*|^2}{|g_s + g_i^*|^2 - 1} \tag{5.32}$$

Again, we simulate n_k for varied internal quality factors and temperatures and find similar behaviour to the non-degenerate case. In the limit of high gain, the minimum noise added n_{k0} is approximately half the corresponding noise added in the non-degenerate case (see Figure 5.8).

5.4.3 Noise Temperature Measurement

The detection chain of the KIPA consists of a series of amplifiers and attenuators, which we depict in Figure 5.9a. Directly after the KIPA there are microwave losses associated with the diplexer, the circulator and the microwave lines. To model the detection chain we divide these losses into two effective attenuators, one at 20mK and the other at 4K. Each attenuator acts like an optical beam splitter, where the transmitted field is reduced by $\sqrt{\alpha}$ and the open port mixes the thermal field $\hat{v}$ into the output according to

the beam splitter equation [27]:

$$\hat{c}_{\text{out}} = \sqrt{\alpha}\,\hat{c}_{\text{in}} + \sqrt{1-\alpha}\,\hat{v} \tag{5.33}$$

At 4K we have the HEMT amplifier, followed by a second microwave amplifier at room temperature. Each amplifier contributes additional noise to its output field as follows [1]:

$$\hat{c}_{\text{out}} = \sqrt{G_{\text{amp}}}\,\hat{c}_{\text{in}} + \sqrt{G_{\text{amp}} - 1}\,\hat{h}^{\dagger} \tag{5.34}$$

Combining the attenuator models for α_1 and α_2 (Equation 5.33), with the amplifier models for the HEMT and room temperature amplifier (Equation 5.34), we may simplify the detection chain to a single equivalent amplifier with gain G_T and noise contribution $\hat{h}_{\text{tot}}$ (see Figure 5.9b). The total output field at the end of the detection chain is given by:

$$\hat{c}_{\text{tot}} = \sqrt{G_T}\,\hat{a}_{\text{out}} + \sqrt{G_T - 1}\,\hat{h}^{\dagger}_{\text{tot}} \tag{5.35}$$

where,

$$G_T = G_R G_H \alpha_1 \alpha_2 \tag{5.36}$$

$$\hat{h}^{\dagger}_{\text{tot}} = \sqrt{\frac{G_R G_H}{G_T - 1}}\left[\sqrt{\alpha_1(1-\alpha_1)}\,v_1 + \sqrt{(1-\alpha_2)}\,v_2 + \sqrt{\frac{G_H - 1}{G_H}}\,\hat{h}^{\dagger}_H + \sqrt{\frac{G_R - 1}{G_R G_H}}\,\hat{h}^{\dagger}_R\right] \tag{5.37}$$

Rewriting the output field $\hat{c}_{\text{out}}$ as a pump phase dependent quadrature operator $\hat{I}_{\text{out}}(\varphi_p) = (\hat{c}^{\dagger}_{\text{out}}e^{-i\varphi_p} + \hat{c}_{\text{out}}e^{i\varphi_p})/2$, we have:

$$\hat{I}_{\text{tot}}(\varphi_p) = \sqrt{G_T}\,\hat{I}_{\text{out}}(\varphi_p) + \sqrt{G_T - 1}\,\hat{I}_h(-\varphi_p) \tag{5.38}$$

where $\hat{I}_{\text{out}}(\varphi_p)$ is the pump phase dependent quadrature operator at the KIPA output, and $\hat{I}_h$ is the detection chain noise quadrature operator $\hat{I}_h(-\varphi_p) = (\hat{h}^{\dagger}_{\text{tot}}e^{i\varphi_p} + \hat{h}_{\text{tot}}e^{-i\varphi_p})/2$.

Assuming $\hat{h}_{\text{tot}}$ and $\hat{a}_{\text{out}}$ are composed of uncorrelated thermal states, we have $\langle\hat{I}_{\text{out}}\rangle = \langle\hat{I}_h\rangle = 0$ and therefore the quadrature fluctuations at the detector simplify to:

$$\langle\Delta\hat{I}^2_{\text{tot}}\rangle = G_T\langle\Delta\hat{I}^2_{\text{out}}\rangle + (G_T - 1)\langle\Delta\hat{I}^2_h\rangle \tag{5.39}$$

$$= G_T\langle\Delta\hat{I}^2_{\text{out}}\rangle + (G_T - 1)\left(\frac{n_{\text{sys}}}{2} + \frac{1}{4}\right) \tag{5.40}$$

where we introduce the effective system noise photon number n_{sys}:

$$n_{\text{sys}} = \langle \hat{h}^{\dagger}_{\text{tot}} \hat{h}_{\text{tot}} \rangle \tag{5.41}$$

$$= \frac{G_R G_H}{G_T - 1} \left[\alpha_2 (1 - \alpha_1)(n_{\text{20mK}} + 1) + (1 - \alpha_2)(n_{\text{4K}} + 1) + \frac{G_H - 1}{G_H} n_H + \frac{G_R - 1}{G_R G_H} n_R \right] \tag{5.42}$$

The average microwave noise power that would be measured by a spectrum analyser is simply the sum of the output quadrature variances:

$$\bar{P}_{\text{tot}} = z(\langle \Delta I^2_{\text{tot}} \rangle + \langle \Delta Q^2_{\text{tot}} \rangle) \tag{5.43}$$

We introduce the parameter z here that converts the units from photons to Watts as is measured by the spectrum analyser.

In non-degenerate operation, the variance of both the KIPA output and the system noise fields are independent of the pump phase, allowing us to write the measured microwave power as:

$$\bar{P}_{\text{tot}} = z G_T (\langle \Delta \hat{I}^2_{\text{out}} \rangle + \langle \Delta \hat{Q}^2_{\text{out}} \rangle) + z(G_T - 1)\left(n_{\text{sys}} + \frac{1}{2} \right) \tag{5.44}$$

$$= 2 z G_T \langle \Delta \hat{I}^2_{\text{out}} \rangle + z(G_T - 1)\left(n_{\text{sys}} + \frac{1}{2} \right) \tag{5.45}$$

In non-degenerate mode, the output fluctuations of the KIPA are given by (see Section 5.4.1):

$$\langle \Delta \hat{I}^2_{\text{out}} \rangle = G_k \left(\frac{n_{\text{th}}}{2} + \frac{1}{4} \right) + (G_k - 1)\left(\frac{n_{\text{th}}}{2} + \frac{n_k}{2} + \frac{1}{4} \right) \tag{5.46}$$

with $G_k = |g_s|^2$ as defined in Equation 2.87, thermal noise population $n_{\text{th}} = \langle \hat{a}^{\dagger}_{\text{in}} \hat{a}_{\text{in}} \rangle$, and additional noise photons added by the KIPA $n_k = \langle \hat{h}^{\dagger}_k \hat{h}_k \rangle$. In the non-degenerate case, the idler mode contributes a minimum $n_{\text{th}}/2 + 1/4$ input referred photons to the variance at the signal frequency, while an additional $n_k/2$ photons arise from internal cavity losses. The excess noise n_k is expected to vary with temperature (see Section 5.4.1), however, for $Q_i > 10^4$ this dependence is negligible compared to $n_{\text{th}} \gg n_k$ and therefore we approximate $n_k \approx n_{k0}$ to be constant with temperature.

Substituting Equation 5.46 into Equation 5.45, we arrive at:

$$\bar{P}_{\text{tot}} = z G_T G_k \left(n_{\text{th}} + \frac{1}{2} \right) + z G_T (G_k - 1)\left(n_{\text{th}} + n_{k0} + \frac{1}{2} \right) + z(G_T - 1)\left(n_{\text{sys}} + \frac{1}{2} \right) \tag{5.47}$$
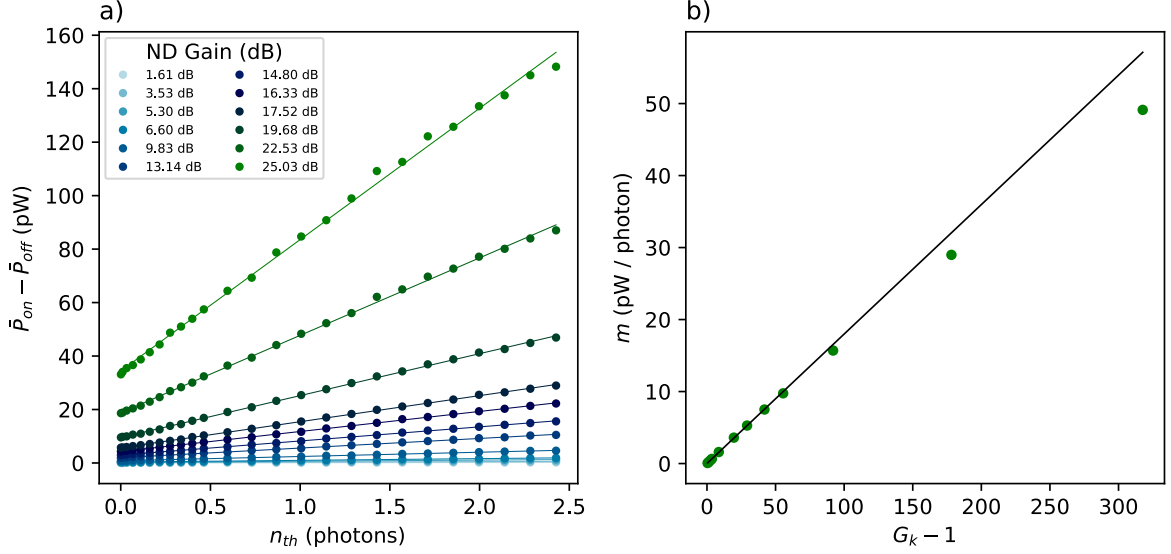
Figure 5.10: (a) The difference power reported by the spectrum analyser for the KIPA on vs off in non-degenerate mode as a function of the thermal photon population at the mixing plate for different non-degenerate (ND) gains (see legend). Solid lines are linear fits. (b) The gradient m of the linear fits presented in (a) ($\bar{P}_{\text{on}} - \bar{P}_{\text{off}} = m \cdot n_{\text{th}} + b$) vs $G_k - 1 = |g_s|^2 - 1$.

Both n_{sys} and the conversion factor zG_T are unknown. We begin by finding zG_T, observing that when the KIPA is off (i.e. $G_k = 1$), Equation 5.47 simplifies to:

$$\bar{P}_{\text{off}} = zG_T\left(n_{\text{th}} + \frac{1}{2}\right) + z(G_T - 1)\left(n_{\text{sys}} + \frac{1}{2}\right) \tag{5.48}$$

The difference in power when the KIPA is on compared to off removes the dependence on n_{sys}:

$$\bar{P}_{\text{tot}} - \bar{P}_{\text{off}} = zG_T(G_k - 1)\left(2n_{\text{th}} + n_{k0} + 1\right) \tag{5.49}$$

To extract zG_T and n_{sys} we sweep the temperature of the mixing chamber of our dilution refrigerator while operating the KIPA as a non-degenerate amplifier (500kHz detuned from $\omega_p/2$). At each temperature, we measure the noise power at the output of our detection chain using a spectrum analyser configured in zero-span mode with a measurement bandwidth of 130 kHz. At each KIPA gain $G_k = |g_s|^2$, we expect the difference in power to increase linearly according to $\bar{P}_{\text{on}} - \bar{P}_{\text{off}} = m \cdot n_{\text{th}} + b$ with gradient $m = 2zG_T(G_k - 1)$ and intercept $b = zG_T(G_k - 1)(n_{k0} + 1)$. Results are presented in Figure 5.10a and show clear linearity with n_{th} for various non-degenerate gains.

Using the fact that $m = 2zG_T(G_k - 1)$, we plot m against $G_k - 1$ to determine the conversion factor $zG_T = 89.9\,\mathrm{fW/photon}$ (see Figure 5.10b). We constrain the linear fit to the lower gain points as the four highest gains deviate from the expected linear behaviour. We attribute this to the amplified noise feature narrowing with gain as is observed for coherent inputs (e.g. Figure 4.6). The total noise power measured corresponds to the integrated power spectral density over the measurement bandwidth. At the lower gains this is approximately flat over the 130 kHz bandwidth, however at the higher gains this approximation no longer holds.

To determine n_{sys} we consider only the noise measurements where $n_{\mathrm{th}} = 0$, allowing us to re-write Equation 5.48 as:

$$n_{\mathrm{sys}} \approx \frac{\bar{P}_{\mathrm{off}}}{zG_T} - 1 \tag{5.50}$$

where we approximate $G_T - 1 \approx G_T$. Given that $G_T = \alpha_1\alpha_2 G_H G_R \sim 70$ dB, this is justified. We extract $n_{\mathrm{sys}} = 84.7$ photons. To validate this number, we substitute data-sheet values for the HEMT and room temperature amplifier into Equation 5.42 and estimate the losses α_1 and α_2 based on cable, circulator and diplexer insertion losses at room temperature. Equation 5.42 gives $\tilde{n}_{\mathrm{sys}} \approx 64$ photons – a reasonable agreement provided the uncertainty in the estimated losses.

Given the conversion factor G_T we may extract the noise temperature of the KIPA in non-degenerate mode by considering the noise referred to the input of the KIPA in photon units and observing that as $G_k \to \infty$:

$$n_{\mathrm{tot}} = \frac{\bar{P}_{\mathrm{tot}}}{zG_T G_k} \tag{5.51}$$

$$\approx (2n_{\mathrm{th}} + n_{k0} + 1) + \frac{1}{G_k}\left(n_{\mathrm{sys}} - n_{\mathrm{th}} - n_{k0}\right) \tag{5.52}$$

$$\to 2n_{\mathrm{th}} + n_{k0} + 1 \tag{5.53}$$

The input referred noise term n_{k0} is the only unknown in this expression. We fit Equation 5.52 to the experimentally measured noise power referred to KIPA input and converted into photons, as is shown in Figure 5.11. From the fit we extract $n_{k0} = 0.16$ photons. On a single measurement quadrature the total input referred fluctuations (including the vacuum contribution) are $\langle \Delta I_{\mathrm{amp}}^2 \rangle = 0.58$ photons, very near the standard quantum limit of 0.5 photons. However, according to theory this is higher than we should expect for $Q_i \approx 10^5$. Figure 5.8c suggests that Q_i should be closer to $2{,}000$, however,
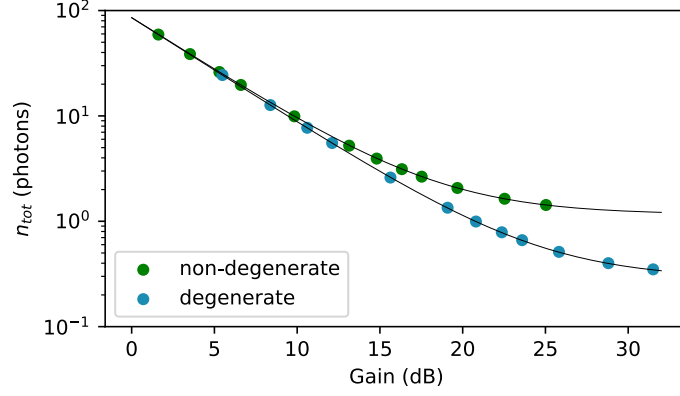
Figure 5.11: The input referred noise n_{tot} measured by the spectrum analyser and converted to photon units for the KIPA operating as a degenerate (blue points) and non-degenerate amplifier (green points). Fits to theory are depicted in black.

we note that this Figure cannot be used to read off the correct Q_i as n_k depends on the gain, which itself is dependent on Q_i. In addition, such a Q_i would produce a measurable dip in the resonator S_{11} response, which was not observed. One possibility is that n_{th}, which we simply calculate here based on the reading of a thermometer on the dilution refrigerator mixing chamber plate, is not an accurate measurement of the actual thermal photon occupation of the electromagnetic field. This could arise from inadequate filtering or thermalisation of cables. In particular, the DC current line must remain unattenuated at temperatures below 4 K (a method typically used to thermalise the inner conductor of the cable) due to the high resistance of the attenuators and risk of heating. The DC line is instead heavily filtered at 7 GHz, however, we cannot be certain of the exact physical temperature of the cable. Future work will improve the thermalisation and filtering of the lines to remove this potential thermal contribution. In addition, a calibrated cryogenic noise source could be used to precisely measure the thermal population of the field at the base temperature of the fridge.

We turn our attention now to the degenerate gain. Because the fluctuations along one quadrature of the KIPA output are squeezed and are therefore considerably smaller than the fluctuations along the orthogonal amplified quadrature, the total noise power

measured at the spectrum analyser may be approximated by:

$$\bar{P}_{\text{tot}} = zG_T(\langle \Delta \hat{I}_{\text{out}}^2 \rangle + \langle \Delta \hat{Q}_{\text{out}}^2 \rangle) + z(G_T - 1)\left(n_{\text{sys}} + \frac{1}{2}\right) \tag{5.54}$$

$$\approx zG_T\langle \Delta \hat{I}_{\text{out}}^2 \rangle + z(G_T - 1)\left(n_{\text{sys}} + \frac{1}{2}\right) \tag{5.55}$$

From Equation 5.30, we have:

$$\bar{P}_{\text{tot}} = zG_TG_k\left(\frac{n_{\text{th}}}{2} + \frac{1}{4}\right) + zG_T(G_k - 1)\left(\frac{n_{k0}}{2}\right) + z(G_T - 1)\left(n_{\text{sys}} + \frac{1}{2}\right) \tag{5.56}$$

giving:

$$n_{\text{tot}} = \frac{\bar{P}_{\text{tot}}}{zG_TG_k} \tag{5.57}$$

$$\approx \frac{n_{\text{th}}}{2} + \frac{n_{k0}}{2} + \frac{1}{4} + \frac{1}{G_k}\left(n_{\text{sys}} + \frac{1}{2} - \frac{n_{k0}}{2}\right) \tag{5.58}$$

As before, we fit Equation 5.58 to the measured noise power at the spectrum analyser, referred to the input of the KIPA and expressed in photons. The results are depicted in Figure 5.11. We find $n_{k0} = 0.07$ photons, very close to half the value of n_{k0} in the non-degenerate case as is predicted by theory.

We conclude that the KIPA is near quantum limited. However, discrepancy between theory and experiment suggests that our initial guess of $Q_i = 10^5$ based on measurements in similar devices is perhaps too optimistic or additional thermalisation and filtering of the measurement lines is warranted.

5.5 Vacuum Squeezing

In this section we present our efforts towards measuring vacuum squeezing produced the KIPA 5.1. To measure squeezing in the presence of a substantial system noise n_{sys}, we observe the reduction in variance along the squeezed quadrature with the KIPA on compared to off using our homodyne detection setup. The difference in variance reduces to $\Delta\sigma^2 = zG_T(1-G_k)(n_{k,0}/2+1/4)$ free from n_{sys}. To measure the squeezing, we convert to photon units by dividing by zG_T and apply this reduction to the output fluctuations, giving $\langle \Delta \hat{Q}_{\text{out}}^2 \rangle = n_{k,0}/2 + 1/4 - \Delta\sigma^2/zG_T$. We observe a reduction in the variance with phase sensitive KIPA gain (see Figure 5.12), which is indicative of squeezing. However, the decrease in variance we observe is greater than the vacuum fluctuations. These are delicate measurements where quadrature imbalance, and HEMT saturation are important
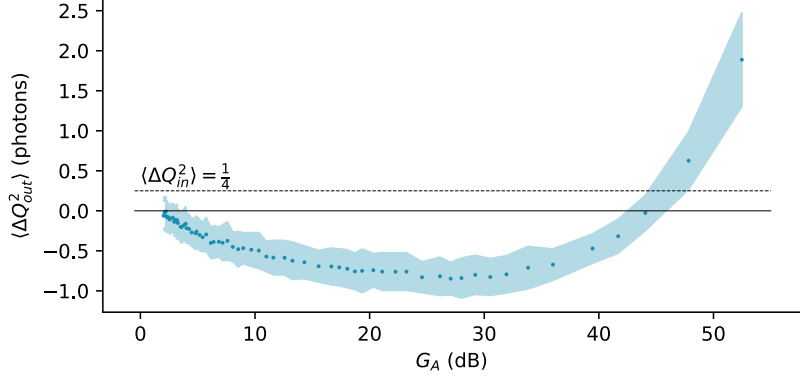
Figure 5.12: The measured KIPA output variance in photon units along the squeezed quadrature $\hat{Q}$. The data show a non-physical reduction in variance and must be a result of analysis or methodological errors in its measurement.

to quantify and as such we don't obtain quantitative agreement with theory. Further, the transformation of the measured data into photon units is highly sensitive to the value of zG_T and any thermal offset that may be present in the cavity, both of which are subject to uncertainty. In order to reduce this uncertainty our group is in the process of repeating the experiment, this time keeping the temperature of the mixing plate fixed and varying the temperature of the KIPA input using a heated attenuator as a calibrated noise source, the methodology used by Zhong *et al.* [12]. Combined with a calibration of the quadrature imbalance of our detection chain and a thorough characterisation of its saturation point, we are optimistic we can resolve the squeezing level produced by the KIPA.

In the context of the experimental setup presented here, measuring squeezing by the KIPA is challenging. On a single quadrature, the detection chain contributes a variance of $n_{\mathrm{sys}}/2 + 1/4 \approx 43$ photons, while the squeezing amounts to at most a 1/4 photon reduction in variance along the squeezed quadrature. The data presented in Figure 5.12 were collected close to the quantisation limits of our digitiser as a comparatively high full scale voltage is required to avoid clipping. Further, the magnitude of the reduction in variance is sensitive to channel imbalances in our setup arising from the mixer and baseband preamps. We did not realise this when performing the squeezing measurement and had insufficient data to compensate for the imbalance during analysis. We aim to repeat this measurement by first learning the linear transformation applied by our detection

103

chain, and then applying its inverse to the noise samples collected in order to minimise its influence on the squeezing measurement.

We are also investigating the possibility of using two KIPAs back-to-back to directly measure the squeezing. A follow on KIPA used as a phase insensitive amplifier will dramatically reduce n_{sys} and place an upper bound on squeezing by measuring $\langle \Delta Q^2_{\text{tot}} \rangle / \langle \Delta Q^2_{\text{off}} \rangle$, as has been successfully demonstrated by Malnou *et al.* [6].

While the source of error here is still under investigation, we use this section to articulate some of the theory we have developed in our efforts to understand the KIPA as a microwave squeezer.

5.5.1 Squeezing Theory

In this section we assume that squeezing is measured over a narrow-band such that the frequency dependence of g_s and g_i may be ignored, allowing us to draw on the theory presented in Section 5.3. Extending this theory to arbitrary bandwidths is beyond the scope of this thesis but will become important to explain an observed squeezing level over a bandwidth that is 'useful' (e.g. the $1-5$ MHz range).

In terms of the matrix elements g_{ij} of the squeezing transformation matrix A_G, Equation 5.9 becomes:

$$
\begin{pmatrix} I_{\text{out}} \\ Q_{\text{out}} \end{pmatrix} = A_G(\theta) \begin{pmatrix} I_{\text{in}} \\ Q_{\text{in}} \end{pmatrix} + \sqrt{\frac{\gamma}{\kappa}} \left(A_G(\theta) + \mathbb{1} \right) \begin{pmatrix} I_b \\ Q_b \end{pmatrix} \tag{5.59}
$$

$$
= \begin{pmatrix} g_{11} & g_{12} \\ g_{21} & g_{22} \end{pmatrix} \begin{pmatrix} I_{in} \\ Q_{in} \end{pmatrix} + \sqrt{\frac{\gamma}{\kappa}} \begin{pmatrix} g_{11}+1 & g_{12} \\ g_{21} & g_{22}+1 \end{pmatrix} \begin{pmatrix} I_b \\ Q_b \end{pmatrix} \tag{5.60}
$$

To obtain expressions for the vacuum squeezing, we now model the input field as a vacuum state with variances $\langle \Delta I^2 \rangle = \langle \Delta Q^2 \rangle$ and zero mean: $\langle I \rangle = \langle Q \rangle = 0$ Assuming the bath and the input fields are uncorrelated, and using the fact that $\langle IQ \rangle + \langle QI \rangle = 0$, we may write the system of linear equations for the second order moments of the output quadratures:

$$
\begin{pmatrix} \langle I^2_{\text{out}} \rangle \\ \langle Q^2_{\text{out}} \rangle \end{pmatrix} = \begin{pmatrix} g^2_{11} & g^2_{12} \\ g^2_{21} & g^2_{22} \end{pmatrix} \begin{pmatrix} \langle I^2_{\text{in}} \rangle \\ \langle Q^2_{\text{in}} \rangle \end{pmatrix} + \frac{\gamma}{\kappa} \begin{pmatrix} (g_{11}+1)^2 & g^2_{12} \\ g^2_{21} & (g_{22}+1)^2 \end{pmatrix} \begin{pmatrix} \langle I^2_b \rangle \\ \langle Q^2_b \rangle \end{pmatrix} \tag{5.61}
$$

Since the vacuum and bath fields are at the same temperature, we define $\langle \Delta I^2_v \rangle = \langle I^2_{\text{in}} \rangle = \langle I^2_b \rangle = 1/4$ and $\langle \Delta Q^2_v \rangle = \langle Q^2_{\text{in}} \rangle = \langle Q^2_b \rangle = 1/4$. Thus, the variances of the output
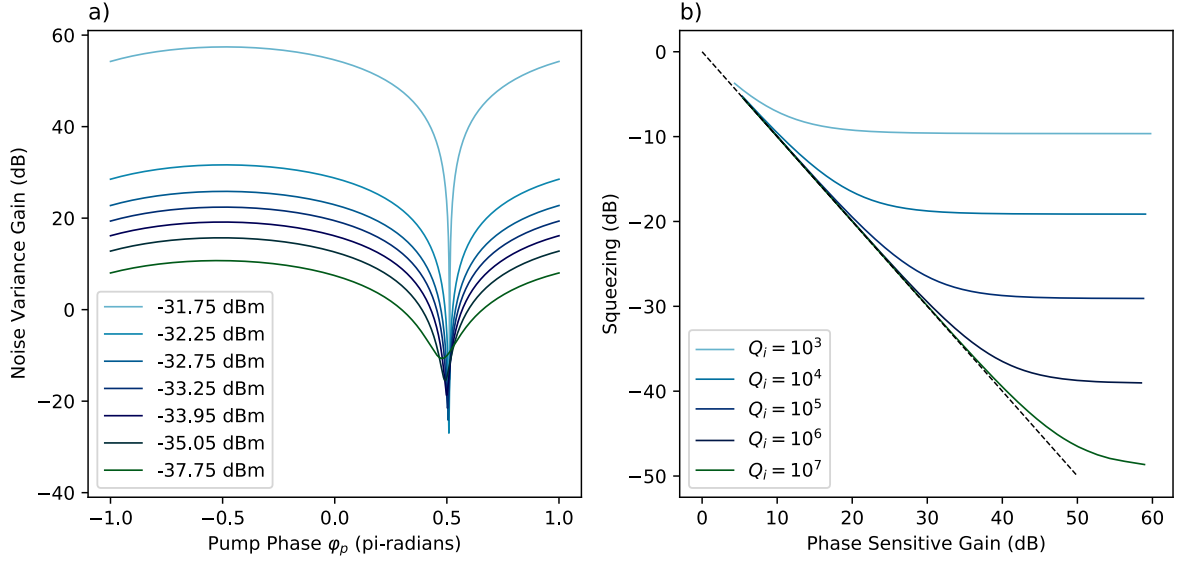
Figure 5.13: (a) The simulated noise variance gain $\mathcal{S}(\varphi_p)$ as a function of the pump phase using the DPA parameters obtained in Section 4.4, for an assortment of pump powers. (b) The vacuum squeezing level $\mathcal{S}_v$, as a function of the phase sensitive gain using the DPA parameters obtained in Section 4.4 for different internal quality factors. The line of symmetric phase sensitive gain is plotted (black dashed line).

quadratures are given by:

$$
\begin{pmatrix} \langle \Delta I_{\text{out}}^2 \rangle \\ \langle \Delta Q_{\text{out}}^2 \rangle \end{pmatrix} = \left[\begin{pmatrix} g_{11}^2 & g_{12}^2 \\ g_{21}^2 & g_{22}^2 \end{pmatrix} + \frac{\gamma}{\kappa} \begin{pmatrix} (g_{11}+1)^2 & g_{12}^2 \\ g_{21}^2 & (g_{22}+1)^2 \end{pmatrix} \right] \begin{pmatrix} \langle \Delta I_v^2 \rangle \\ \langle \Delta Q_v^2 \rangle \end{pmatrix} \tag{5.62}
$$

The increase/decrease in quadrature variance as a function of the pump phase φ_p is described by:

$$
\mathcal{S}(\varphi_p) = 10 \log_{10} \frac{\langle \Delta I_{\text{out}}^2 \rangle}{\langle \Delta I_v^2 \rangle} = 10 \log_{10} \left(g_{11}^2 + g_{12}^2 + \frac{\gamma}{\kappa}((g_{11}+1)^2 + g_{12}^2) \right) \tag{5.63}
$$

and the vacuum squeezing level $\mathcal{S}_v$ is defined by the minimum of $\mathcal{S}$:

$$
\mathcal{S}_v = \min_{\varphi_p} \mathcal{S}(\varphi_p) \tag{5.64}
$$

Using the DPA parameters extracted from the phase-insensitive gain features (see Section 4.4), we can simulate the expected noise variance gain (Equation 5.63) as a function of the pump phase, again assuming a $Q_i \approx 10^5$. The results are depicted in Figure 5.13a, where we observe a similar phase dependent response as was measured in

Section 4.5 for strong coherent inputs. In contrast to the phase-sensitive gain for coherent inputs, the coupling of the bath mode into the cavity requires a strictly asymmetric noise variance gain such that $(\min_{\varphi_p} S(\varphi_p) \times \max_{\varphi_p} S(\varphi_p)) \geq 1$, where equality holds only in the limit of $Q_i \to \infty$. We observe a weak shift in the pump phase corresponding to the point of maximum squeezing as the pump power increases, which is a consequence of the non-zero detuning between the cavity and the pump Δ.

Equipped with this squeezing model and a realistic set of resonator parameters, we can study the effect of Q_i on the maximum attainable squeezing. Figure 5.13b plots the vacuum squeezing level $\mathcal{S}_v$ against the maximum variance gain, or anti-squeezing gain. In the limit of no losses, Cave's theory predicts symmetric squeezing and anti-squeezing with zero noise photons contributed by the amplifier [1]. We observe here that the squeezing/anti-squeezing relationship of the KIPA closely follows the expected symmetric behaviour before the squeezing level plateaus to a constant level as the anti-squeezing gain increases. The squeezing level plateaus as the total cavity fluctuations are limited by the bath mode variance, which is not squeezed by the KIPA since:

$$\left(A_G + \mathbb{1}\right)\begin{pmatrix}\mathrm{Var}(I_b)\\\mathrm{Var}(Q_b)\end{pmatrix} \geq \begin{pmatrix}\mathrm{Var}(I_b)\\\mathrm{Var}(Q_b)\end{pmatrix} \tag{5.65}$$

We observe an approximate 10 dB improvement in the maximum achievable squeezing for each order of magnitude increase in Q_i. The order of magnitude improvement in squeezing performance is a result of the corresponding order of magnitude decrease in γ/κ, which sets the magnitude of the bath variance contribution to the KIPA output (see Equation 5.9). For our estimate of $Q_i = 10^5$, our theory predicts up to $\mathcal{S}_v \approx -29$ dB of squeezing produced by the KIPA, corresponding to approximately 40 dB of phase sensitive gain.

5.6 Statistical Properties of the Output Field

The Wigner function of the vacuum state $|0\rangle$ is a Gaussian quasi-probability distribution with variance $1/4$ along each axis in the I, Q basis. According to Equation 5.9, the ideal DPA linearly transforms this probability distribution (to a bivariate Gaussian with unequal quadrature variances) and mixes in a statistically uncorrelated vacuum state from the bath. Assuming our detection chain is linear and only contributes thermal noise
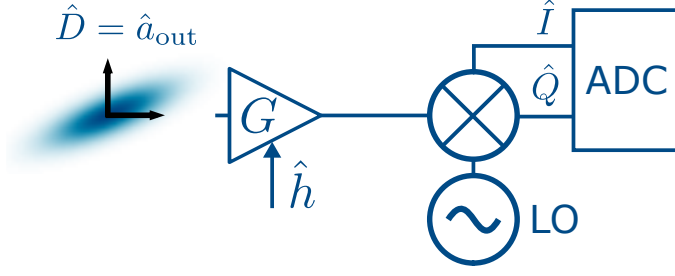
Figure 5.14: The simplified detection chain model used in the statistical analysis of the output field. The KIPA output field $\hat{D} = \hat{a}_{\mathrm{out}}$ is depicted as a squeezed Gaussian quasi-probability distribution. The detection chain is simplified to a single amplifier with equivalent gain G and noise contribution $\hat{h}$ referred to the KIPA output. The output of the detection chain is down-converted into $\hat{I}$ and $\hat{Q}$ observables by a mixer, and the noise is digitised by an Analog to Digital Converter (ADC).

to the detected output, it is expected that the quasi-probability distribution of the noise we measure at room temperature is also Gaussian.

As was the case for coherent inputs, a non-linear distortion of the phase space (see Figure 2.8) is an indication of Hamiltonian non-idealities. In the context of measuring noise, a non-linear distortion of the phase space may be quantified by the statistical moments of the output field. Boutin *et al.* demonstrate that deviations from Gaussianity measured using the statistical moments or cumulants of the observed output noise field are a symptom of the system Hamiltonian deviating from the Hamiltonian of the ideal DPA, which in turn limits the attainable squeezing of a device [5]. In this section we infer the moments and cumulants of the KIPA output field using Eichler *et al.*'s single path reconstruction technique [43] to support the claim that the KIPA is a highly idealised DPA that produces squeezed Gaussian noise.

To study the statistical properties of the KIPA, we consider the simplified detection chain model presented in Figure 5.14, where the detection chain gain is represented by a single amplifier with gain G with noise contribution $\hat{h}_{\mathrm{tot}}$ as is similarly defined in Section 5.4. The output field of the detection is down-converted using a microwave mixer, allowing us to measure the quadrature observables $\hat{I}$ and $\hat{Q}$, which we refer here to the output of the KIPA to simplify notation. Adopting Boutin *et al.*'s notation, we denote the *output* field of the KIPA by the operator $\hat{D} = \hat{a}_{\mathrm{out}}$, and define $\hat{h}$ as the noise operator $\hat{h}_{\mathrm{tot}}$ referred to the output of the KIPA (i.e. $\hat{h} = \hat{h}_{\mathrm{tot}}/\sqrt{G}$). From the beam splitter relations for the

mixer, it follows that [43]:

$$\hat{D} + \hat{h}^\dagger = \sqrt{2}(\hat{I} + i\hat{Q}) = \hat{S} \tag{5.66}$$

Using the complex observable $\hat{S}$ we may reconstruct the moments and cumulants of the KIPA output field $\hat{D}$ and the equivalent detection chain noise field $\hat{h}$.

5.6.1 Moments

Experimentally, we collect $N = 10^6$ samples of the operators $\hat{I}$ and $\hat{Q}$, allowing us to estimate the complex quasi-probability distribution $P_{\text{on(off)}}(\hat{S})$ of the observable $\hat{S}$ with the KIPA on (off) using a 2-dimensional histogram of the (I, Q) sample pairs, which we denote $P^\star_{\text{on(off)}}[i,j]$ at bin position (i,j). The axes of the 2-dimensional histogram correspond to the real and imaginary parts of the observable $\hat{S}$, or equivalently $\sqrt{2}\hat{I}$ and $\sqrt{2}\hat{Q}$. By definition, the normally ordered moments of $\hat{S}$ are given by:

$$\langle (\hat{S}^\dagger)^n \hat{S}^m \rangle_{\text{on(off)}} = \int_S (\hat{S}^*)^n \hat{S}^m P_{\text{on(off)}}(S)dS \tag{5.67}$$

$$\approx 2^{(n+m)/2} \sum_k \sum_j (I[k] - iQ[j])^n (I[k] + iQ[j])^m P^\star_{\text{on(off)}}[k,j]\Delta I \Delta Q$$

$$\tag{5.68}$$

where $I[k]$ and $Q[j]$ are the quadrature voltages at bin positions k and j respectively, and ΔI and ΔQ are the histogram bin widths. We construct the histogram $P^\star$ by binning the sampled noise pairs into 256×256 bins over a $\pm 4mV$ range, and then use Equation 5.68 to obtain the moments for $\hat{S}$. Histograms for the KIPA on ($G_A \approx 30$ dB) and the KIPA off are depicted in Figure 5.15 along with the uni-variate histograms of $\hat{I}$ and $\hat{Q}$. Along one axis, amplification of the noise is obvious when the KIPA is active. Due to the 84.7 noise photons contributed by the detection chain, there is little discernible difference along the squeezed quadrature which can at most reduce by $1/2$ a photon. As discussed previously, we infer the squeezing from this weak difference in noise. Gaussian fits to the uni-variate histograms for both the KIPA on and the KIPA off case show no evidence of non-gaussian character, which we now examine more closely from the inferred moments of the KIPA output field.

As $\hat{D}$ is a squeezed thermal state that is uncorrelated with the detection chain noise
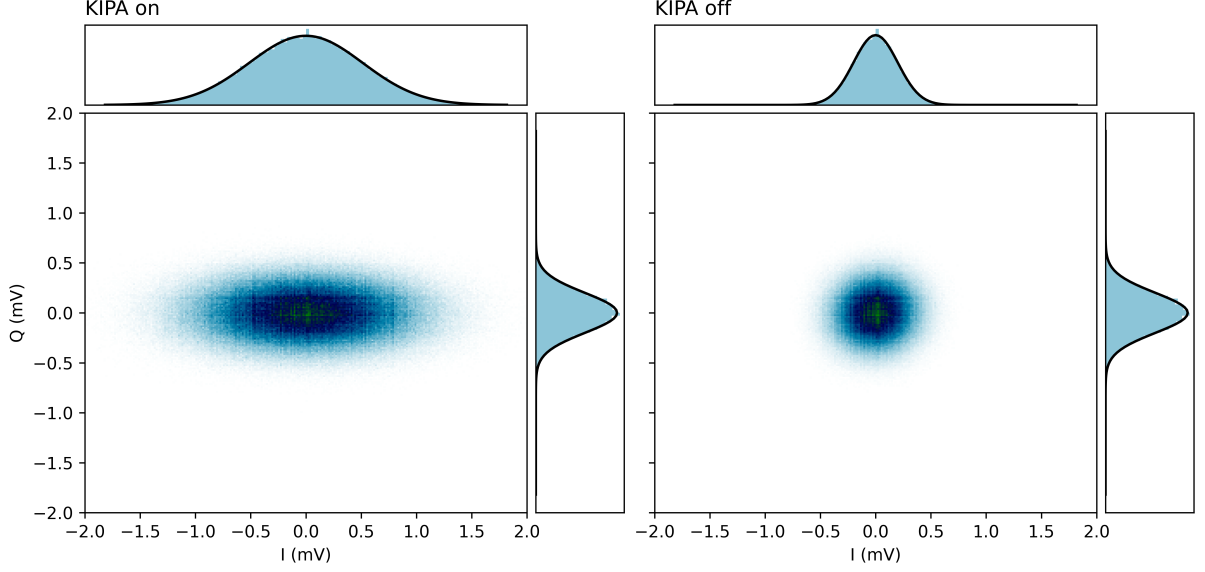
Figure 5.15: Two dimensional histograms (256×256 bins) of the output field with the KIPA on (left) and the KIPA off (right) obtained from $N = 10^6$ samples of noise on each detection quadrature. Histograms of the marginal distributions are shown (light blue) with Gaussian fits (solid black line).

field $\hat{h}$, we may expand the normally ordered moments of $\hat{S} = \hat{D} + \hat{h}^\dagger$, giving [43]:

$$\langle (\hat{S}^\dagger)^n \hat{S}^m \rangle_{\text{on(off)}} = \sum_{k,j=0}^{n,m} \binom{n}{k} \binom{m}{j} \langle (\hat{D}^\dagger)^k \hat{D}^j \rangle \langle h^{n-k}(h^\dagger)^{m-j} \rangle \tag{5.69}$$

When the KIPA is off ($I_p = 0$), the output field is simply in the vacuum state, corresponding to $\langle (D^\dagger)^n D^m \rangle = 0$ for all $n, m \neq 0$. Thus, Equation 5.69 simplifies to:

$$\langle (\hat{S}^\dagger)^n \hat{S}^m \rangle_{\text{off}} = \langle h^n (h^\dagger)^m \rangle \tag{5.70}$$

Using this equation to calculate the moments of the detection chain noise field when the device is off, we may reconstruct the moments of the field $\hat{D}$ by solving Equation 5.69 recursively and using the fact that $\langle (\hat{D}^\dagger)^0 \hat{D}^0 \rangle = 1$:

$$\langle (\hat{D}^\dagger)^n \hat{D}^m \rangle = \langle (\hat{S}^\dagger)^n \hat{S}^m \rangle_{\rho_a} - \sum_{k \neq n \wedge j \neq m}^{n,m} \binom{n}{k} \binom{m}{j} \langle (\hat{D}^\dagger)^k \hat{D}^j \rangle \langle h^{n-k}(h^\dagger)^{m-j} \rangle \tag{5.71}$$

In order to quantify differences between our measured moments and the ideal DPA and detection chain, which produce Gaussian noise fields, we construct a Gaussian model for our system that uses the mean and covariance matrix measured from our raw data. The ideal Gaussian fields are then sampled $N = 10^6$ times (the same as the number
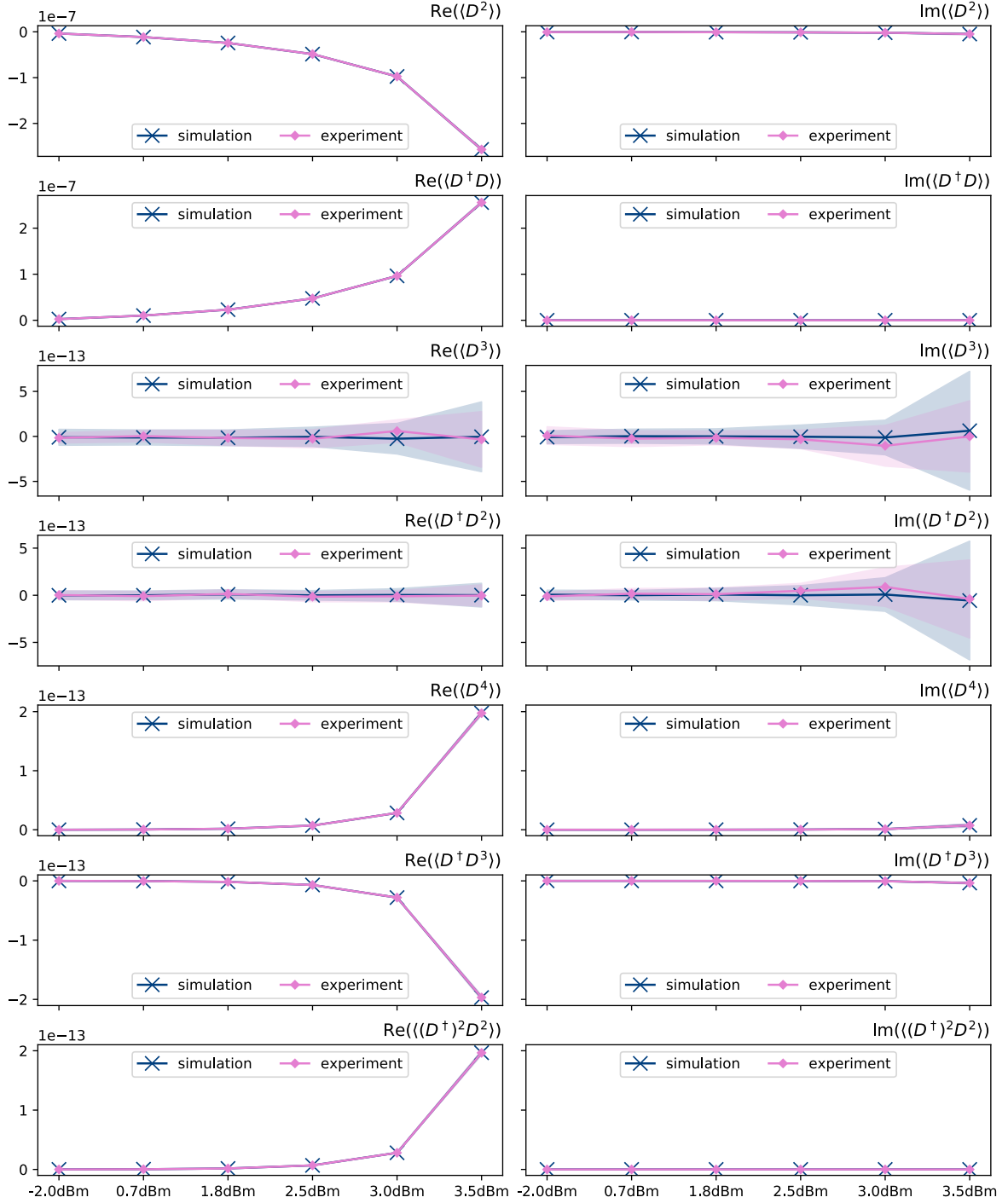
Figure 5.16: The real and imaginary parts of the moments of the field $\hat{D}$ evaluated recursively using Equation 5.71. All data is presented with error bars obtained from repeated measurement/simulation (blue and pink shaded areas). Vertical axes are in arbitrary units and are kept consistent between real and imaginary parts. The horizontal axis defines the pump power at the microwave source.

of samples collect in the experiment) to artificially generate noise data that follow the expected distribution for the DPA and detection chain. Note that this simulated data does not model any theoretical behaviour of the KIPA, but is simply used to reveal deviation from Gaussianity if present, and quantify errors in moment estimation due to sampling and the approximation we make in Equation 5.68.

The statistical moments of the KIPA output field $\hat{D}$ up to order 4 (presented in Figure 5.16) show excellent agreement with the simulated Gaussian noise. Both the experimental and simulated second and fourth order moments coincide with near negligible errors. The third order moments for an ideal Gaussian distribution are zero, which is reflected in both the experimental and simulated data where error bars in each case cross zero. The error bars on the third order moments are comparable for the experimental and simulated datasets, indicating that the errors we see on the experimental data are determined by the collection of a finite number of samples or equivalently the finite resolution of the 2-dimensional histogram. While not visible in Figure 5.16, the error bars the for the remaining moments are comparable between the simulated and experimental data, lending more evidence to this claim.

From the moments of the KIPA output field, we are unable to find evidence of any deviation from Gaussianity to within the sensitivity permitted by a 256×256 pixel estimate of the output quasi-probability distribution and $N = 10^6$ noise samples. This supports the derived KIPA Hamiltonian (see Section 3.4) and its negligible Kerr term.

5.6.2 Cumulants

Typically, the cumulants of the noise are been presented in microwave squeezing work [21, 12, 5], as the cumulants of a Gaussian distribution should be exactly zero for $n+m > 2$ and deviations from Gaussianity appear more obvious. Cumulants of a uni-variate distribution also offer the advantage of being able to reconstruct the density function using the Gram-Charlier or Edgeworth series, however extending these reconstruction techniques to the bivariate case is beyond the scope of this work. The cumulants, denoted $\langle\langle \cdots \rangle\rangle$, are derived from the statistical moments using the formula [62]:

$$\langle\langle (b^\dagger)^n b^m \rangle\rangle = \frac{\partial^n}{\partial x^n} \frac{\partial^m}{\partial y^m} \log \left[\sum_{i,j} \frac{\langle (b^\dagger)^n b^m \rangle x^i y^j}{i! j!} \right] \Bigg|_{x=y=0} \qquad (5.72)$$

Neglecting moments greater than order 4, we extract expressions for the cumulants
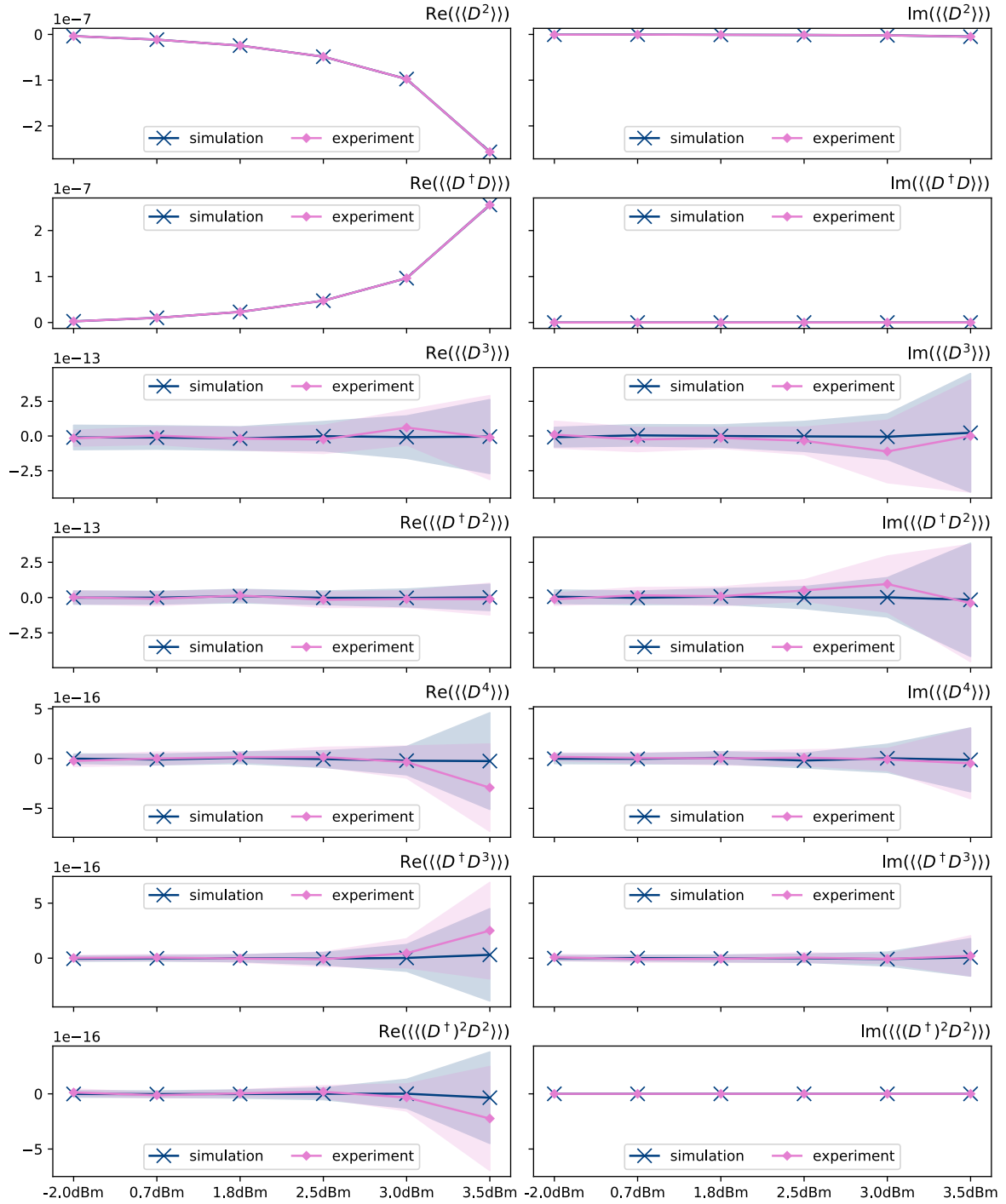
Figure 5.17: The real and imaginary parts of the cumulants of the field $\hat{D}$ evaluated using the experimentally measured moments and simulated Gaussian moments that are presented in Figure 5.16. All data is presented with error bars obtained from repeated measurement/simulation (blue and pink shaded areas). Vertical axes are in arbitrary units and are kept consistent between real and imaginary parts. The horizontal axis defines the pump power at the microwave source.

using the Python computer algebra library *SymPy*. The algebraic expressions for the cumulants up to order four may be found in Appendix A. Using the results obtained for the moments from the previous section, we extract the cumulants, presented in Figure 5.17. The error bars of all third and fourth order cumulants cross over zero, as is expected for Gaussian fields. Further, comparing the experimental and artificial noise we find that the third and fourth order cumulants and their error bars have significant overlap. We are unable to rule out that the error bars and small deviations from zero aren't a consequence of sampling aretfacts, as the sampled simulated distributions would suggest. The increase in error with pump power is a by-product of the increase in the anti-squeezed variance, which factors into the calculation of the moments of $\hat{S}$ (see Equation 5.68). Again, there is no significant evidence to suggest that the KIPA output field is any less Gaussian than our artificially generated Gaussian noise, further supporting the hypothesis that the KIPA Hamiltonian well approximates the Hamiltonian of the DPA.

Chapter 6

Conclusion

In this thesis we have presented the theoretical and experimental characterisation of a novel microwave amplifier called the KIPA, based on parametric mixing processes that take place in superconductors featuring high kinetic inductance, as occurs in the NbTiN film that makes up our device. The simple design of the KIPA facilitates a three wave mixing process by passing a bias current through the resonant geometry, enabling phase sensitive amplification by an off resonant pump. We derive the Hamiltonian of the KIPA using the principals of circuit-QED and find close agreement with the Hamiltonian for an ideal degenerate parametric amplifier. By extracting the non-linearity constant of the film, I_2^*, we are able to show that the additional Kerr term present in the KIPA Hamiltonian is negligible compared to the remaining DPA components. Already, this shows evidence that the KIPA is a highly-idealised DPA that is free from the non-idealities that limit squeezing in similar microwave frequency devices [5].

We characterise the KIPA as a phase insensitive and a phase sensitive amplifier, where we find in approximately 40 dB and 50 dB of gain respectively. Combining our theory for the KIPA Hamiltonian with input-output formalism, we find excellent fits to theory for the phase sensitive and phase insensitive gain profiles arising from realistic system parameters. In phase insensitive, or non-degenerate, operation the KIPA maintains a gain bandwidth product of 98 MHz. In phase sensitive operation, we find a 1 dB compression power of -43 dBm referred to the KIPA output, orders of magnitude greater than has been realised in JPAs. Further, we speculate that the compression power of the KIPA may be even higher than the value reported here as we are unable to rule out compression of our HEMT.

Using homodyne detection, we image the phase space of the KIPA output for a phase swept coherent input and find no obvious distortion of the phase space, which has been shown to be a typical symptom of limited squeezing ability [5]. Using the Hamiltonian of the DPA and input-output theory we are again able to accurately predict the observed linear distortion of the phase space, assuming some weak reflections in our setup. Up to 26 dB of deamplification is observed, showing promise of significant squeezing potential by this device. We find the KIPA to be quantum limited, producing an additional 0.07 input referred photons in phase sensitive operation. We believe a sizeable portion of this contribution to the output fluctuations could be explained by a thermal offset in our setup. Although future work is needed to fully understand the noise squeezing properties of the KIPA, we observed additional evidence of near ideal DPA operation by studying the statistical properties of the output field. We extract the moments and cumulants of the noise distribution inferred to the KIPA output and find no significant deviation from Gaussianity.

The highly idealised nature of the KIPA raises the exciting prospect that it is capable of squeezing the vacuum to levels not observed before in the microwave regime. Due to its compact nature, it is foreseeable that the KIPA may be engineered to interact with other quantum systems 'on-chip', providing access to squeezing that is not limited by the losses between elements of an experimental setup. Squeezing levels < 5 dB have already been used to enhance the sensitivity and accelerate the measurement of a number of physical phenomena, including the search for dark matter axions and the weak measurement of electron spin resonance echos. We envisage that the KIPA can contribute to these efforts and may facilitate new experiments in quantum metrology and quantum computing with microwave cluster states.

The next steps for this device require us to robustly characterise its squeezing abilities. We aim to refine our measurement of the squeezing level inferred from the reduction in detection chain noise with the KIPA active. Repeating this across multiple bias currents will unveil the influence of the bias current on the losses present in our system and their impact on squeezing. Ultimately we wish to then characterise squeezing with a follow on quantum limited amplifier, which will allow us to place a concrete upper bound on the achievable squeezing by this device. Combined with new theory to characterise the squeezing as a function of the measurement bandwidth, we hope to attain a complete

theoretical framework that accurately models the behaviour of our device.

The KIPA is an incredibly simple device to manufacture, and despite this, we are able show here that it robustly behaves as an ideal degenerate parametric amplifier, a claim not yet made in the microwave domain.

Bibliography

[1] C. M. Caves, "Quantum limits on noise in linear amplifiers," *Physical Review D*, vol. 26, pp. 1817–1839, Oct. 1982. Publisher: American Physical Society.

[2] M. Tse, H. Yu, N. Kijbunchoo, A. Fernandez-Galiana, P. Dupej, L. Barsotti, C. Blair, D. Brown, S. Dwyer, A. Effler, M. Evans, P. Fritschel, V. Frolov, A. Green, G. Mansell, F. Matichard, N. Mavalvala, D. McClelland, L. McCuller, T. McRae, J. Miller, A. Mullavey, E. Oelker, I. Phinney, D. Sigg, B. Slagmolen, T. Vo, R. Ward, C. Whittle, R. Abbott, C. Adams, R. Adhikari, A. Ananyeva, S. Appert, K. Arai, J. Areeda, Y. Asali, S. Aston, C. Austin, A. Baer, M. Ball, S. Ballmer, S. Banagiri, D. Barker, J. Bartlett, B. Berger, J. Betzwieser, D. Bhattacharjee, G. Billingsley, S. Biscans, R. Blair, N. Bode, P. Booker, R. Bork, A. Bramley, A. Brooks, A. Buikema, C. Cahillane, K. Cannon, X. Chen, A. Ciobanu, F. Clara, S. Cooper, K. Corley, S. Countryman, P. Covas, D. Coyne, L. Datrier, D. Davis, C. Di Fronzo, J. Driggers, T. Etzel, T. Evans, J. Feicht, P. Fulda, M. Fyffe, J. Giaime, K. Giardina, P. Godwin, E. Goetz, S. Gras, C. Gray, R. Gray, A. Gupta, E. Gustafson, R. Gustafson, J. Hanks, J. Hanson, T. Hardwick, R. Hasskew, M. Heintze, A. Helmling-Cornell, N. Holland, J. Jones, S. Kandhasamy, S. Karki, M. Kasprzack, K. Kawabe, P. King, J. Kissel, R. Kumar, M. Landry, B. Lane, B. Lantz, M. Laxen, Y. Lecoeuche, J. Leviton, J. Liu, M. Lormand, A. Lundgren, R. Macas, M. MacInnis, D. Macleod, S. Márka, Z. Márka, D. Martynov, K. Mason, T. Massinger, R. McCarthy, S. McCormick, J. McIver, G. Mendell, K. Merfeld, E. Merilh, F. Meylahn, T. Mistry, R. Mittleman, G. Moreno, C. Mow-Lowry, S. Mozzon, T. Nelson, P. Nguyen, L. Nuttall, J. Oberling, R. Oram, B. O'Reilly, C. Osthelder, D. Ottaway, H. Overmier, J. Palamos, W. Parker, E. Payne, A. Pele, C. Perez, M. Pirello, H. Radkins, K. Ramirez, J. Richardson, K. Riles, N. Robertson, J. Rollins, C. Romel, J. Romie, M. Ross, K. Ryan, T. Sadecki, E. Sanchez,

L. Sanchez, T. Saravanan, R. Savage, D. Schaetzl, R. Schnabel, R. Schofield, E. Schwartz, D. Sellers, T. Shaffer, J. Smith, S. Soni, B. Sorazu, A. Spencer, K. Strain, L. Sun, M. Szczepańczyk, M. Thomas, P. Thomas, K. Thorne, K. Toland, C. Torrie, G. Traylor, A. Urban, G. Vajente, G. Valdes, D. Vander-Hyde, P. Veitch, K. Venkateswara, G. Venugopalan, A. Viets, C. Vorvick, M. Wade, J. Warner, B. Weaver, R. Weiss, B. Willke, C. Wipf, L. Xiao, H. Yamamoto, M. Yap, H. Yu, L. Zhang, M. Zucker, and J. Zweizig, "Quantum-Enhanced Advanced LIGO Detectors in the Era of Gravitational-Wave Astronomy," *Physical Review Letters*, vol. 123, p. 231107, Dec. 2019.

[3] K. M. Backes, D. A. Palken, S. A. Kenany, B. M. Brubaker, S. B. Cahn, A. Droster, G. C. Hilton, S. Ghosh, H. Jackson, S. K. Lamoreaux, A. F. Leder, K. W. Lehnert, S. M. Lewis, M. Malnou, R. H. Maruyama, N. M. Rapidis, M. Simanovskaia, S. Singh, D. H. Speller, I. Urdinaran, L. R. Vale, E. C. van Assendelft, K. van Bibber, and H. Wang, "A quantum enhanced search for dark matter axions," *Nature*, vol. 590, pp. 238–242, Feb. 2021.

[4] A. Bienfait, J. J. Pla, Y. Kubo, M. Stern, X. Zhou, C. C. Lo, C. D. Weis, T. Schenkel, M. L. W. Thewalt, D. Vion, D. Esteve, B. Julsgaard, K. Mølmer, J. J. L. Morton, and P. Bertet, "Reaching the quantum limit of sensitivity in electron spin resonance," *Nature Nanotechnology*, vol. 11, pp. 253–257, Mar. 2016. Number: 3 Publisher: Nature Publishing Group.

[5] S. Boutin, D. M. Toyli, A. V. Venkatramani, A. W. Eddins, I. Siddiqi, and A. Blais, "Effect of Higher-Order Nonlinearities on Amplification and Squeezing in Josephson Parametric Amplifiers," *Physical Review Applied*, vol. 8, p. 054030, Nov. 2017. Publisher: American Physical Society.

[6] M. Malnou, D. Palken, L. R. Vale, G. C. Hilton, and K. Lehnert, "Optimal Operation of a Josephson Parametric Amplifier for Vacuum Squeezing," *Physical Review Applied*, vol. 9, p. 044023, Apr. 2018. Publisher: American Physical Society.

[7] A. Bienfait, P. Campagne-Ibarcq, A. Kiilerich, X. Zhou, S. Probst, J. Pla, T. Schenkel, D. Vion, D. Esteve, J. Morton, K. Moelmer, and P. Bertet, "Mag-

netic Resonance with Squeezed Microwaves," *Physical Review X*, vol. 7, p. 041011, Oct. 2017. Publisher: American Physical Society.

[8] P. Krantz, M. Kjaergaard, F. Yan, T. P. Orlando, S. Gustavsson, and W. D. Oliver, "A quantum engineer's guide to superconducting qubits," *Applied Physics Reviews*, vol. 6, p. 021318, June 2019.

[9] C. Eichler, A. J. Sigillito, S. A. Lyon, and J. R. Petta, "Electron spin resonance at the level of 10^4 spins using low impedance superconducting resonators," *Phys. Rev. Lett.*, vol. 118, p. 037701, Jan 2017.

[10] S. Probst, A. Bienfait, P. Campagne-Ibarcq, J. J. Pla, B. Albanese, J. F. Da Silva Barbosa, T. Schenkel, D. Vion, D. Esteve, K. Mølmer, J. J. L. Morton, R. Heeres, and P. Bertet, "Inductive-detection electron-spin resonance spectroscopy with 65 spins/ hz sensitivity," *Applied Physics Letters*, vol. 111, no. 20, p. 202604, 2017.

[11] V. Ranjan, S. Probst, B. Albanese, T. Schenkel, D. Vion, D. Esteve, J. J. L. Morton, and P. Bertet, "Electron spin resonance spectroscopy with femtoliter detection volume," *Applied Physics Letters*, vol. 116, no. 18, p. 184002, 2020.

[12] L. Zhong, E. P. Menzel, R. Di Candia, P. Eder, M. Ihmig, A. Baust, M. Haeberlein, E. Hoffmann, K. Inomata, T. Yamamoto, Y. Nakamura, E. Solano, F. Deppe, A. Marx, and R. Gross, "Squeezing with a flux-driven Josephson parametric amplifier," *New Journal of Physics*, vol. 15, p. 125013, Dec. 2013.

[13] M. Malnou, D. Palken, B. Brubaker, L. R. Vale, G. C. Hilton, and K. Lehnert, "Squeezed Vacuum Used to Accelerate the Search for a Weak Classical Signal," *Physical Review X*, vol. 9, p. 021023, May 2019.

[14] K. W. Murch, S. J. Weber, K. M. Beck, E. Ginossar, and I. Siddiqi, "Suppression of the radiative decay of atomic coherence in squeezed vacuum," *Nature*, vol. 499, pp. 62–65, July 2013. arXiv: 1301.6276.

[15] M. Gu, C. Weedbrook, N. C. Menicucci, T. C. Ralph, and P. van Loock, "Quantum computing with continuous-variable clusters," *Phys. Rev. A*, vol. 79, p. 062318, Jun 2009.

[16] B. W. Walshe, L. J. Mensen, B. Q. Baragiola, and N. C. Menicucci, "Robust fault tolerance for continuous-variable cluster states with excess antisqueezing," *Physical Review A*, vol. 100, Jul 2019.

[17] E. A. Tholén, A. Ergül, E. M. Doherty, F. M. Weber, F. Grégis, and D. B. Haviland, "Nonlinearities and parametric amplification in superconducting coplanar waveguide resonators," *Applied Physics Letters*, vol. 90, p. 253509, Jun 2007.

[18] M. R. Vissers, R. P. Erickson, H.-S. Ku, L. Vale, X. Wu, G. C. Hilton, and D. P. Pappas, "Low-noise kinetic inductance traveling-wave amplifier using three-wave mixing," *Applied Physics Letters*, vol. 108, p. 012601, Jan. 2016.

[19] A. Anferov, A. Suleymanzade, A. Oriani, J. Simon, and D. I. Schuster, "Millimeter-wave four-wave mixing via kinetic inductance for quantum devices," *Physical Review Applied*, vol. 13, Feb 2020.

[20] M. Malnou, M. R. Vissers, J. D. Wheeler, J. Aumentado, J. Hubmayr, J. N. Ullom, and J. Gao, "A three-wave mixing kinetic inductance traveling-wave amplifier with near-quantum-limited noise performance," *arXiv:2007.00638 [astro-ph, physics:quant-ph]*, Nov. 2020. arXiv: 2007.00638.

[21] C. Eichler, Y. Salathe, J. Mlynek, S. Schmidt, and A. Wallraff, "Quantum-Limited Amplification and Entanglement in Coupled Nonlinear Resonators," *Physical Review Letters*, vol. 113, p. 110502, Sept. 2014.

[22] X. Zhou, V. Schmitt, P. Bertet, D. Vion, W. Wustmann, V. Shumeiko, and D. Esteve, "High-gain weakly nonlinear flux-modulated Josephson parametric amplifier using a SQUID array," *Physical Review B*, vol. 89, p. 214517, June 2014.

[23] R. E. Slusher, L. W. Hollberg, B. Yurke, J. C. Mertz, and J. F. Valley, "Observation of Squeezed States Generated by Four-Wave Mixing in an Optical Cavity," *Physical Review Letters*, vol. 55, pp. 2409–2412, Nov. 1985.

[24] R. Movshovich, B. Yurke, P. G. Kaminsky, A. D. Smith, A. H. Silver, R. W. Simon, and M. V. Schneider, "Observation of zero-point noise squeezing via a Josephson-parametric amplifier," *Physical Review Letters*, vol. 65, pp. 1419–1422, Sept. 1990.

[25] C. Eichler, D. Bozyigit, C. Lang, L. Steffen, J. Fink, and A. Wallraff, "Experimental State Tomography of Itinerant Single Microwave Photons," *Physical Review Letters*, vol. 106, p. 220503, June 2011.

[26] C. Cohen-Tannoudji, B. Diu, and F. Laloë, *Quantum mechanics*. New York: Wiley, 1977.

[27] D. F. Walls and G. J. Milburn, *Quantum optics*. Berlin: Springer, 2nd ed ed., 2008.

[28] M. A. Castellanos-Beltran, K. D. Irwin, G. C. Hilton, L. R. Vale, and K. W. Lehnert, "Amplification and squeezing of quantum noise with a tunable Josephson metamaterial," *Nature Physics*, vol. 4, pp. 929–931, Dec. 2008.

[29] G. Milburn and D. Walls, "Production of squeezed states in a degenerate parametric amplifier," *Optics Communications*, vol. 39, pp. 401–404, Nov. 1981.

[30] D. M. Pozar, *Microwave engineering*. Hoboken, NJ: Wiley, 4th ed ed., 2012. OCLC: ocn714728044.

[31] M. H. Devoret, "Quantum Fluctuations in Electrical Circuits," p. 351, Jan. 1997.

[32] B. Yurke and E. Buks, "Performance of Cavity-Parametric Amplifiers, Employing Kerr Nonlinearites, in the Presence of Two-Photon Loss," *Journal of Lightwave Technology*, vol. 24, pp. 5054–5066, Dec. 2006.

[33] A. Blais, A. L. Grimsmo, S. M. Girvin, and A. Wallraff, "Circuit Quantum Electrodynamics," *arXiv:2005.12667 [quant-ph]*, May 2020. arXiv: 2005.12667.

[34] J. Zmuidzinas, "Superconducting Microresonators: Physics and Applications," *Annual Review of Condensed Matter Physics*, vol. 3, pp. 169–214, Mar. 2012.

[35] J. Gao, M. Daal, A. Vayonakis, S. Kumar, J. Zmuidzinas, B. Sadoulet, B. A. Mazin, P. K. Day, and H. G. Leduc, "Experimental evidence for a surface distribution of two-level systems in superconducting lithographed microwave resonators," *Applied Physics Letters*, vol. 92, no. 15, p. 152505, 2008.

[36] A. Bruno, G. de Lange, S. Asaad, K. L. van der Enden, N. K. Langford, and L. Di-Carlo, "Reducing intrinsic loss in superconducting resonators by surface treatment

and deep etching of silicon substrates," *Applied Physics Letters*, vol. 106, p. 182601, May 2015.

[37] A. Bienfait, "Magnetic resonance with quantum microwaves," p. 186.

[38] C. W. Gardiner and M. J. Collett, "Input and output in damped quantum systems: Quantum stochastic differential equations and the master equation," *Physical Review A*, vol. 31, pp. 3761–3774, June 1985.

[39] S. Boutin, "Amplificateur paramétrique Josephson : Limite quantique, modélisation et caractérisation," p. 152.

[40] B. Yurke, P. G. Kaminsky, R. E. Miller, E. A. Whittaker, A. D. Smith, A. H. Silver, and R. W. Simon, "Observation of 4.2-K equilibrium-noise squeezing via a Josephson-parametric amplifier," *Physical Review Letters*, vol. 60, pp. 764–767, Feb. 1988.

[41] C. Eichler and A. Wallraff, "Controlling the dynamic range of a Josephson parametric amplifier," *EPJ Quantum Technology*, vol. 1, p. 2, Dec. 2014.

[42] V. V. Sivak, S. Shankar, G. Liu, J. Aumentado, and M. H. Devoret, "Josephson Array-Mode Parametric Amplifier," *Physical Review Applied*, vol. 13, p. 024014, Feb. 2020.

[43] C. Eichler, D. Bozyigit, and A. Wallraff, "Characterizing quantum microwave radiation and its entanglement with superconducting qubits using linear detectors," *Physical Review A*, vol. 86, Sep 2012.

[44] S. Anlage, H. Snortland, and M. Beasley, "A current controlled variable delay superconducting transmission line," *IEEE Transactions on Magnetics*, vol. 25, pp. 1388–1391, Mar. 1989.

[45] P. V. Christiansen, E. B. Hansen, and C. J. Sjöström, "Negative self-inductance in superconducting thin wires and weak links," *Journal of Low Temperature Physics*, vol. 4, pp. 349–389, Apr. 1971.

[46] L. H. London F., "The electromagnetic equations of the supraconductor," *Proceedings of the Royal Society of London. Series A - Mathematical and Physical Sciences*, vol. 149, pp. 71–88, Mar. 1935.

[47] M. Tinkham, *Introduction to superconductivity*. Dover books on physics, Mineola, NY: Dover Publ, 2. ed ed., 2004. OCLC: 728146785.

[48] A. B. Pippard, "An experimental and theoretical study of the relation between magnetic field and current in a superconductor," *Proceedings of the Royal Society of London. Series A. Mathematical and Physical Sciences*, vol. 216, pp. 547–568, Feb. 1953.

[49] A. J. Annunziata, D. F. Santavicca, L. Frunzio, G. Catelani, M. J. Rooks, A. Frydman, and D. E. Prober, "Tunable superconducting nanoinductors," *Nanotechnology*, vol. 21, p. 445202, Nov. 2010.

[50] A. J. Kerman, E. A. Dauler, J. K. W. Yang, K. M. Rosfjord, V. Anant, K. K. Berggren, G. N. Gol'tsman, and B. M. Voronov, "Constriction-limited detection efficiency of superconducting nanowire single-photon detectors," *Applied Physics Letters*, vol. 90, p. 101110, Mar. 2007.

[51] B. Ho Eom, P. K. Day, H. G. LeDuc, and J. Zmuidzinas, "A wideband, low-noise superconducting amplifier with high dynamic range," *Nature Physics*, vol. 8, pp. 623–627, Aug. 2012.

[52] S. Chaudhuri, D. Li, K. D. Irwin, C. Bockstiegel, J. Hubmayr, J. N. Ullom, M. R. Vissers, and J. Gao, "Broadband parametric amplifiers based on nonlinear kinetic inductance artificial transmission lines," *Applied Physics Letters*, vol. 110, p. 152601, Apr. 2017.

[53] R. P. Erickson and D. P. Pappas, "Theory of multiwave mixing within the superconducting kinetic-inductance traveling-wave amplifier," *Physical Review B*, vol. 95, p. 104506, Mar. 2017.

[54] N. Samkharadze, A. Bruno, P. Scarlino, G. Zheng, D. P. DiVincenzo, L. DiCarlo, and L. M. K. Vandersypen, "High-kinetic-inductance superconducting nanowire res-

onators for circuit qed in a magnetic field," *Phys. Rev. Applied*, vol. 5, p. 044004, Apr 2016.

[55] L. Zhang, W. Peng, L. X. You, and Z. Wang, "Superconducting properties and chemical composition of nbtin thin films with different thickness," *Applied Physics Letters*, vol. 107, no. 12, p. 122603, 2015.

[56] A. J. Sigillito, A. M. Tyryshkin, T. Schenkel, A. A. Houck, and S. A. Lyon, "Electrically driving nuclear spin qubits with microwave photonic bangap resonators," 2017.

[57] D. I. Schuster, "Circuit Quantum Electrodynamics," *Dissertation*, p. 255, May 2007.

[58] M. S. Khalil, M. J. A. Stoutimore, F. C. Wellstood, and K. D. Osborn, "An analysis method for asymmetric resonator transmission applied to superconducting devices," *Journal of Applied Physics*, vol. 111, no. 5, p. 054510, 2012.

[59] S. Probst, F. B. Song, P. A. Bushev, A. V. Ustinov, and M. Weides, "Efficient and robust analysis of complex scattering data under noise in microwave resonators," *Review of Scientific Instruments*, vol. 86, no. 2, p. 024706, 2015.

[60] "Fitkit: Python library." https://github.com/Emigon/fitkit/tree/develop. SHA-1: d4532cfbd0080c7b2180082290768ab07746970e.

[61] C. M. Wilson, T. Duty, and P. Delsing, "Parametric oscillators based on superconducting circuits," in *Fluctuating Nonlinear Oscillators* (M. Dykman, ed.), pp. 390–410, Oxford University Press, July 2012.

[62] C. Eichler, Y. Salathe, J. Mlynek, S. Schmidt, and A. Wallraff, "Supplementary material for "Quantum limited amplification and entanglement in coupled nonlinear resonators"," p. 9.

Appendices

A Algebraic Expressions for the Cumulants

n	m	$\langle\langle (a^\dagger)^n a^m \rangle\rangle$
-1	0	$\log\left(a_{00}\right)$
-1	1	$\left(a_{01}\right)/a_{00}$
0	0	$\left(a_{10}\right)/a_{00}$
1	0	$\left(6a_{20} - \frac{6a_{10}^2}{a_{00}}\right)/6a_{00}$
-1	2	$\left(6a_{02} - \frac{6a_{01}^2}{a_{00}}\right)/6a_{00}$
0	1	$\left(6a_{11} - \frac{6a_{01}a_{10}}{a_{00}}\right)/6a_{00}$
2	0	$\left(3a_{30} - \frac{9a_{10}a_{20}}{a_{00}} + \frac{6a_{10}^3}{a_{00}^2}\right)/3a_{00}$
-1	3	$\left(3a_{03} - \frac{9a_{01}a_{02}}{a_{00}} + \frac{6a_{01}^3}{a_{00}^2}\right)/3a_{00}$
1	1	$\left(3a_{21} - \frac{3a_{01}a_{20}}{a_{00}} - \frac{6a_{10}a_{11}}{a_{00}} + \frac{6a_{01}a_{10}^2}{a_{00}^2}\right)/3a_{00}$
0	2	$\left(3a_{12} - \frac{6a_{01}a_{11}}{a_{00}} - \frac{a_{10}\left(6a_{02} - \frac{12a_{01}^2}{a_{00}}\right)}{2a_{00}}\right)/3a_{00}$
3	0	$\left(a_{40} - \frac{4a_{10}a_{30}}{a_{00}} - \frac{3a_{20}^2}{a_{00}} + \frac{12a_{10}^2a_{20}}{a_{00}^2} - \frac{6a_{10}^4}{a_{00}^3}\right)/a_{00}$
-1	4	$\left(a_{04} - \frac{4a_{01}a_{03}}{a_{00}} - \frac{3a_{02}^2}{a_{00}} + \frac{12a_{01}^2a_{02}}{a_{00}^2} - \frac{6a_{01}^4}{a_{00}^3}\right)/a_{00}$
2	1	$\left(a_{31} - \frac{a_{01}a_{30}}{a_{00}} - \frac{3a_{10}a_{21}}{a_{00}} - \frac{3a_{11}a_{20}}{a_{00}} + \frac{6a_{01}a_{10}a_{20}}{a_{00}^2} + \frac{6a_{10}^2a_{11}}{a_{00}^2} - \frac{6a_{01}a_{10}^3}{a_{00}^3}\right)/a_{00}$
0	3	$\left(a_{13} - \frac{3a_{01}a_{12}}{a_{00}} - \frac{a_{10}\left(a_{03} - \frac{6a_{01}a_{02}}{a_{00}} + \frac{6a_{01}^3}{a_{00}^2}\right)}{a_{00}} - \frac{a_{11}\left(6a_{02} - \frac{12a_{01}^2}{a_{00}}\right)}{2a_{00}}\right)/a_{00}$
1	2	$\left(a_{22} - \frac{2a_{01}a_{21}}{a_{00}} - \frac{a_{02}a_{20}}{a_{00}} - \frac{2a_{10}a_{12}}{a_{00}} - \frac{2a_{11}^2}{a_{00}} + \frac{2a_{01}^2a_{20}}{a_{00}^2} + \frac{8a_{01}a_{10}a_{11}}{a_{00}^2} + \frac{2a_{02}a_{10}^2}{a_{00}^2} - \frac{6a_{01}^2a_{10}^2}{a_{00}^3}\right)/a_{00}$

Table 1: Analytical expressions for the cumulants of the field $\hat{a}$ in terms of its moments up to order $n + m = 4$. For brevity, the shorthand $a_{nm} = \langle (\hat{a}^\dagger)^n \hat{a}^m \rangle$ is used.